The Effects of Collimation on Image Formation in Anger Gamma Cameras

Nia Eleri Harrison

Thesis for the degree of Doctor of Philosophy

University College London
University of London

August 1993

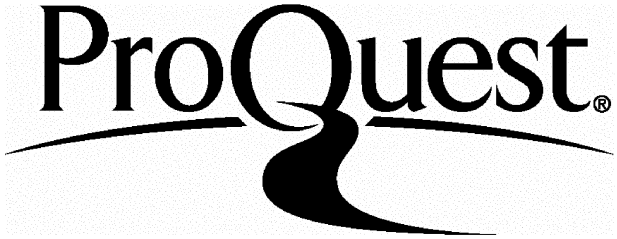

Abstract

This thesis investigates the effects that collimators have on gamma camera images in nuclear medicine studies using technetium-99m. A Monte Carlo simulation of photon transport through a multihole collimator was written to determine the average point source response function of collimators. The code is flexible, thus enabling the modelling of different dimensions, hole misalignments and alternative structures. Separate computer programs were written to produce images of source distributions using various collimator response functions. The effects on the response functions and images of photons which have passed through collimator walls are determined.

Collimator hole angulations of up to 1° are simulated and images produced using collimator simulations with random angulations over the collimator. The effects of angulation on the spatial resolution and linearity are investigated.

Laminated collimator structures are proposed as a means of producing more robust, lighter weight collimators. Response functions are obtained for several different layer thicknesses and are compared with those of a conventional lead collimator. It is shown that computer images obtained from a laminated collimator compare favourably with those from a conventional lead collimator.

Alternative materials to lead are considered for use in collimators and depleted uranium is determined to be suitable. The improved absorption properties of uranium would enable a much reduced septal thickness to be used with no increase in photon penetration. Such a reduction would also produces an increase in collimator efficiency.

Contents

List of figures

List of tables

Errata

Chapter 1

p. 31	Equation 1.4	Denominator $= \left(1+\frac{\sqrt{2}}{3}\right)$, Result $\approx 0.804\,DF$

Chapter 2

p. 42	Line 22	Delete second occurrence of 'of photon transport'.
p. 42	Line 27	Insert '(Horrocks 1988)' after 'UCL'.
p. 43	Line 25	Insert '(Rodriguez-Villafuerte 1991)' after 'results'.
p. 57	Line 17	Replace '0.1%' with '0.4%'.
p. 60	Equation 2.15	The variable 'dt' should be inserted after each integral.
p. 60	Equation 2.16	The variable 'dt' should be inserted after the integral.
p. 76	Paragraph 2	Insert at end of paragraph 'The fitting routine is based on the Singular Value Decomposition least squares fitting routine of Press *et al* (1988).'.

Chapter 3

p. 77	Line 23	Before the final sentence the following should be inserted: 'The widths were measured from the response curves by determining the intersection points of the curve with the lines y = 0.5, y = 0.1 and y = 0.01.'
p. 80	Line 8	Insert '(i.e. a source placed at the face of the collimator)' after '0 cm'.
p. 80	Table 3.2	Replace '± 0.001 cm' with '±0.01 cm'.
p. 84	Line 16	Insert ', a septal thickness of 0.24 mm' after 'hole size'.
p. 88	Figure 3.7	Replace 'L' with 'M' in figure key.
p. 89	Line 9	Replace 'table 3.5' with 'table 3.6'.

Chapter 4

p. 96	Line 19	Replace 'will the subdivide' with 'will then subdivide'.
p.107	Line 1	Insert 'The angulations were random only in magnitude and not in orientation.' after 'in figure 4.8.'
p. 113	Line 13	Insert 'Collimator M0100 was used for all images of laminated structures.' after 'a conventional collimator.'.

Chapter 5

p. 141	Line 1	Replace 'of the collimator' with 'of the collimators'.

-1-

The gamma camera and the description of images

The gamma camera is a well established instrument in radioisotope imaging. A vital component of the gamma camera is the collimator. This thesis considers the various effects of collimators on gamma camera images by using Monte Carlo techniques to model photon transport. Various defects in collimators are considered and the results of such defects on images are presented. Collimators constructed from different materials and using different designs are also simulated. This chapter introduces the gamma camera, discussing the various components of the camera, concentrating in particular on the collimator and its design.

1.1 The Gamma Camera

This section briefly discusses the development of the gamma camera from its introduction to the modern camera. The basic principles of the camera are presented.

1.1.1 Historical Introduction

The first attempts at radionuclide imaging were made in the late 1940s. Moores (1948) reported on the diagnosis and localisation of brain tumours using I^{131} and a highly shielded beta-gamma Geiger-Müller tube mounted on a portable unit. The detection unit was placed directly on the skin at several different locations on the skull and the counts recorded for each measurement site. A repeat examination of the sites of higher activity was made in order to localise more definitely the suspected lesion.

The use of phosphors for scintillation detectors was discussed by Sharpe and Taylor (1951) and the advantages of thallium-activated sodium iodide [NaI(Tl)] for gamma ray detection were noted. The first imaging device to effectively image γ-ray distributions within the body was the rectilinear scanner described by Cassen *et al* (1951). The scanner was an automated version of the device built by Moores (1948) and consisted of a collimated scintillation counter scanning in a raster pattern over the patient. The collimation restricted the field of view of the counter to a small volume directly beneath it. The image of the radioactive distribution was obtained by correlating the recorded count rate with the spatial position of the detector at the time.

Another use of the scintillator was demonstrated by Anger (1952) in a pinhole camera which consisted of a stationary lead shield with a pinhole aperture and a γ-ray

sensitive film with a thallium activated sodium iodide, NaI(Tl), intensifying screen. The method required a therapeutic dose of I^{131} and an exposure time of one hour. A faint but usable image of a tumour on the elbow was achieved. Anger later reported a much improved gamma-ray camera (Anger 1958) which replaced the film-screen combination with a single large-area NaI(Tl) crystal and a packed array of seven photomultiplier tubes (figure 1.1). A signal matrix circuit determined the position of interactions and a pulse-height analyser rejected all signals outside a predetermined energy window. The image was produced on a cathode-ray oscilloscope and photographed by a conventional camera for storage.

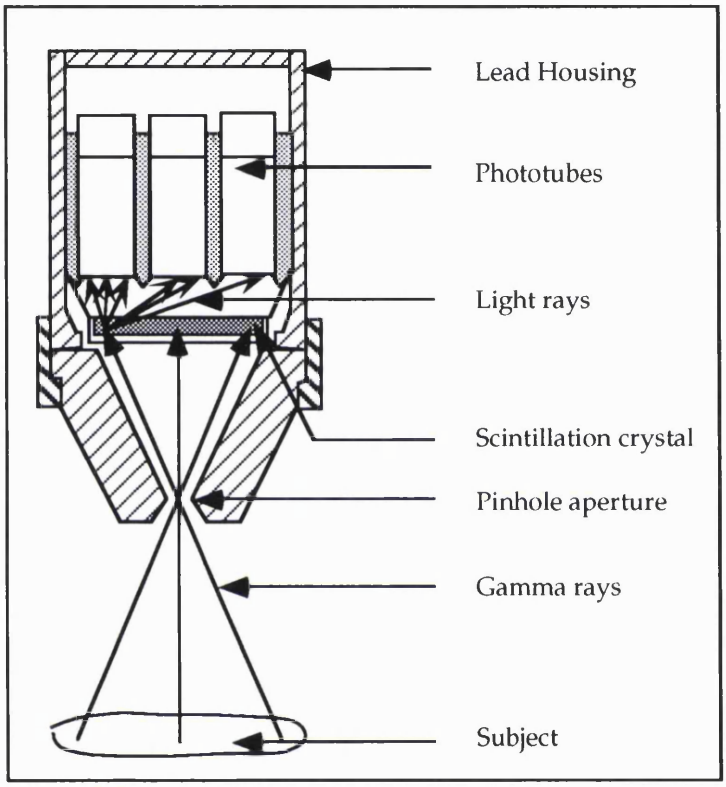

Figure 1.1 The gamma camera introduced by Anger (1958).

This gamma camera had several advantages over the rectilinear scanner. It was concurrently sensitive to all parts of the field of view, and, since no scanning was involved, the image had no line structure. The camera could be easily oriented in any direction making it more flexible for unusual views. In addition, the acquisition time for a study using such a camera was less than that for a rectilinear scanner since no mechanical scanning motions were involved. An initial disadvantage that the gamma camera had when compared with the rectilinear scanner was its small field of view. This meant that early cameras required two exposures when imaging large objects such as the lungs and although a solution to this problem was to construct a larger scintillation detector for the camera this would have led to increasing technical problems. A solution was found in the design of diverging collimators rather than parallel holed collimators (Muehllehner 1969).

Since the Anger camera was first introduced other imaging devices have been developed, but the camera has become the main instrument in nuclear medicine for measuring *in-vivo* distributions of activity due to its balance of image quality, detection efficiency and ease of use.

1.1.2 The modern gamma camera

Much work has been carried out in the field of the gamma camera since the introduction of the pinhole camera in 1952. The replacement of the photographic plate by PM tubes and a cathode ray oscilloscope (CRO) was a significant improvement (Anger 1958). Soon to follow were new multihole collimator designs; both parallel holes (Anger 1964) and tapered holes (Muehllehner 1969), enabling the imaging of larger organs. Investigations were conducted into crystal material and thickness (Anger and Davis 1964, Mallard and Myers 1963a), the type of photomultiplier tube (Mallard and Myers 1963b) and the use of digital rather than analogue circuitry for image production. The advent of emission computer tomography (Freedman 1970, Muehllehner 1971, Chang *et al* 1980, Shosa *et al* 1980) led to a new line of research both in camera design and reconstruction techniques.

1.1.2.1 Basic Construction

A schematic diagram of the basic components of a modern gamma camera is shown in figure 1.2.

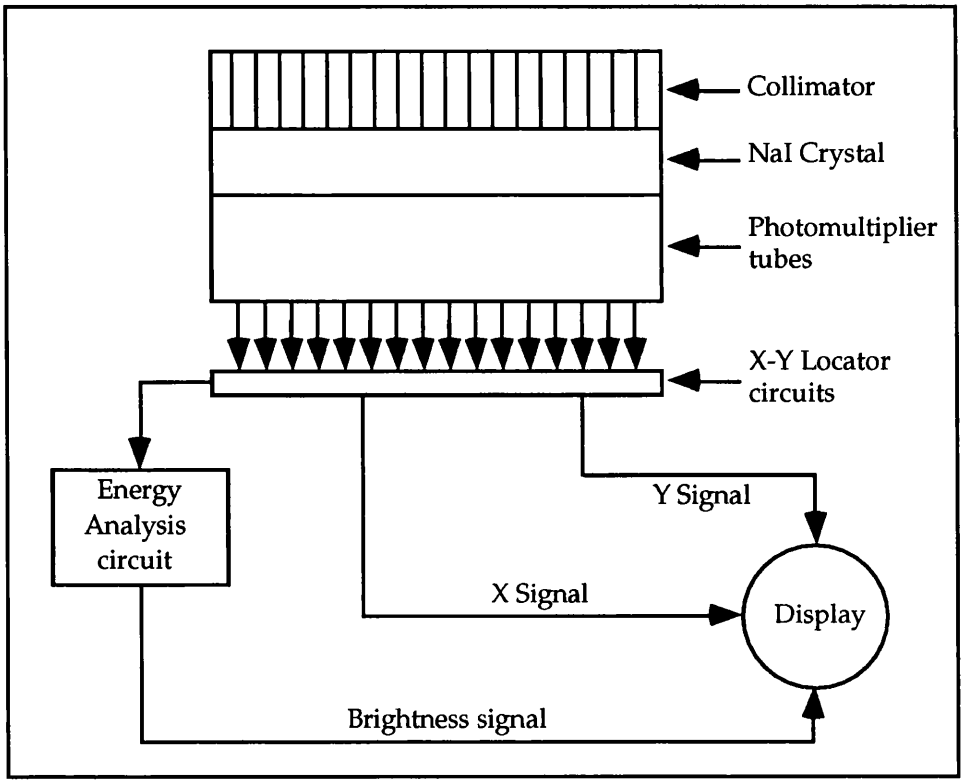

Figure 1.2 The modern gamma camera.

Gamma photons from a radioactive distribution interact within a large-area, thin scintillation crystal optically coupled to a closely packed array of photomultiplier (PM) tubes. The crystal and PM tubes are hermetically sealed in a light-tight can to keep out moisture and light. This can is usually constructed from a thin aluminium sheet on the front face and sides so as not to attenuate the incoming gamma-rays, while the surface between the crystal and PM tubes is an optical window.

The photoelectric absorption of a photon within the crystal results in the emission of a scintillation pulse in the visible spectrum. The pulse is proportional in intensity to the energy of the absorbed gamma ray. The PM tubes convert the light to an electronic signal and amplify it to give a sufficiently large current to be handled by an electronic circuit. The PM tubes closest to an absorption event will receive the greatest intensity of light photons and hence signals produced by these tubes will have greater amplitudes than those further away. The signals from the PM tubes are processed to give X and Y position signals and a Z energy signal. The energy signal is produced by the summation of the outputs from all the tubes to give the total light produced by the scintillation. The summed energy signal is then passed to a pulse height analyser and if the energy is within the set range the signals are processed to give the image.

Since gamma-rays are emitted isotropically, the detector described above would not result in an image, however, as there is no inherent relationship between the location of the scintillation interaction and the point of emission of the gamma-ray from the patient. Just as in an optical camera the film alone is not sufficient to form an image of the scene, so the scintillation camera described above does not constitute a gamma-ray imaging system. The function of the detector is to record an image formed by another element. In the case of an optical camera this is the lens. However, with high-frequency radiation such as gamma-rays a much cruder device must be employed, the collimator. Several varieties of collimator exist. All are made from a high atomic number material, and all but one type have many holes. The design and quality of the collimator determines the quality of the image produced and will be considered throughout the thesis.

1.2 Factors to be considered in the design of camera components

The gamma camera system consists of several different components; the crystal, PM tubes and associated electronics, and the collimator. To achieve good images careful consideration must be given to the design of each component. This section describes the components of the camera and considers briefly some of the factors to be considered in gamma camera design.

1.2.1 The crystal

The purpose of the scintillation crystal is to convert photons incident on it to a light pulse whose amplitude is proportional to the photon energy absorbed in the crystal. The crystal is therefore useful for energy-selective counting. The desirable properties of a scintillation crystal are the following:

(a) High photoelectric absorption efficiency;
(b) High conversion of gamma-ray energy into light;
(c) Short scintillation decay time;
(d) Crystal transparent to its own scintillations;
(e) Wavelength of light should match response of PM tubes.

Inorganic alkali halide crystals are favoured for use in gamma-ray spectroscopy due to the high density and relatively high atomic number of the constituents. In inorganic crystals, the absorption of the energy of a photon elevates an electron from the valence band across the band gap to the conduction band leaving a hole in the valence band. A photon is emitted when a hole is filled by an electron returning to the valence band. In a pure crystal the energy of the photon would typically be of too high an energy to lie in the visible range. In order to enhance the probability of the production of visible photons, impurities, known as activators, are added to the lattice to modify the band structure by creating energy states within the band gap through which the electron can de-excite back to the valence band. Since this energy is lower than that of the gap, visible photons can be produced by the transition.

The most commonly used scintillation crystal in gamma cameras is thallium-activated sodium iodide (NaI(Tl)). NaI is a good absorber of photons in the range 30 keV to 700 keV due to the high atomic number of iodine ($Z = 53$) and its relatively high density ($\rho = 3.67$ g/cm^3). It is a relatively efficient scintillator, yielding one visible light photon per 30 eV of radiation energy absorbed. The wavelength of the light photons produced is 410 nm, close to that required by the PM tubes. The duration of each scintillation is about 0.8 μs. There is little loss of scintillation light caused by self-absorption since NaI is transparent to its own scintillation emissions. The output signal from the detector is proportional in amplitude to the amount of radiation energy absorbed in the crystal allowing the detector to be used for energy-selective counting.

Sensitivity considerations demand the thickest possible crystal, but to locate a scintillation accurately a thin crystal is required as a gamma ray may cause a scintillation anywhere between the top and bottom of the crystal. For an angle of incidence ϕ, the lateral distance between events at the top and bottom faces is given by $t \tan\phi$, where t is the crystal thickness, so the error in positioning is expected to be proportional to t. It has been shown (Mallard and Myers 1963a) that errors due to this effect are negligible for crystals of thickness up to 13 mm. A thinner crystal also minimises the adverse effects of Compton

scatter in the crystal (Anger and Davis 1964). Gamma camera crystals are typically 6-12 mm thick, with a diameter of up to 50 cm to provide a large field of view.

The exit window of the crystal is optically coupled to lightguides using silicone grease. The purpose of the lightguides is to optically interface the crystal to the PM tubes so that light losses are kept to a minimum. The guides are made from a transparent plastic and are carefully shaped to match the photocathode in the PM tubes. The refractive index of the plastic is matched to the refractive index of the tube. The use of a thin light guide improves the spatial resolution but tends to worsen the effects of non-linearity and non-uniformity. The lightguide is also optically coupled to the PM tubes using silicone grease. In some modern cameras the lightguide is dispensed with in favour of correction procedures in the data processing stage.

1.2.2 The photomultiplier tubes

The purpose of the photomultiplier tubes is to convert the scintillation pulse created in the crystal to an electrical signal which is then multiplied to produce a sufficiently large current pulse to be handled by an electronic circuit. The PM tubes consist of two major elements — the photocathode and the dynode structure (Appendix 1 — PM tube description and diagram). Anger's scintillation camera (Anger 1958) had an array of 7 photomultiplier tubes of 1.5 inch (38 mm) diameter. The tubes used in the modern gamma camera have a much smaller diameter (~25 mm) enabling a greater number of tubes to be contained in the array, typically 75 or 91. The tubes, of circular or hexagonal cross-section, are closely packed in a hexagonal array. The use of a large number of small diameter tubes improves the spatial resolution but can cause non-uniformity problems. The voltage supply to the PM tube array must be stable so that the gain remains constant.

The photocathode material is chosen such that its spectral response matches the scintillation emission wavelength from the crystal while at the same time giving a high quantum efficiency in order to minimise statistical fluctuations in the output signal. The bialkali K_2CsSb, activated with oxygen and caesium, satisfies these requirements.

Of major importance in the choice of the dynode material is its stability to changes in voltage and temperature. Beryllium-copper dynodes show a reasonable stability although their gain is lower than gallium phosphide coated dynodes (Simon and Williams 1968). Of the various dynode configurations available in PM tubes, the most effective dynode structure for gamma cameras is the Venetian blind construction, with the first dynode modified to a 'teacup' shape, so that the angle of incidence of primary electrons does not lead to a non-uniform response (Short 1984).

1.2.3 Signal processor

The PM tube outputs are processed to give the position information by means of a resistive coupled network. The energy signal, obtained from the summation of the outputs

from all PM tubes is subjected to pulse height analysis, all signals lying within a chosen energy window being used to form the image.

1.2.3.1 The Anger logic circuit

In analogue cameras the outputs from the array of PM tubes are passed through a capacitor network or a resistive-coupled network to provide the position information necessary to form an image. The relative intensity of the signal determines the (x, y) coordinates of the scintillation event and provides four signals x^+, x^-, y^+, y^- to produce an image on an oscilloscope. The total intensity z of the signal is given by the sum of the four signals

$$z = x^+ + x^- + y^+ + y^- \tag{1.1}$$

and the x and y positions are given by

$$x = \frac{k\left(x^+ + x^-\right)}{z} \quad \text{and} \quad y = \frac{k\left(y^+ + y^-\right)}{z} \tag{1.2}$$

where k is a scale factor adjusted for the deflection voltage requirements of the oscilloscope.

In newer cameras the positional signals from the PM tubes are either converted to digital signals using an interface box before displaying the output on a computer, or the conversion to a digital signal is performed directly on each PM tube output. In the latter case, a microprocessor performs the position and energy calculations and the output is displayed by a computer.

1.2.3.2 Pulse height analysis

Energy selection in a gamma camera is achieved by passing the z signal from the PM tubes and logic circuitry through a single channel analyser and setting two discrimination levels to determine whether the signal lies within an expected energy window. Photons with energies lower than the lower-level discriminator or higher than the upper-level discriminator will be rejected. Any signals lying within the energy window are accepted and the x and y signals are passed to the display unit to produce the image.

1.2.4 The collimator

Since gamma rays are isotropically emitted, no inherent relationship exists between the position of interaction of the gamma ray with the crystal and its point of emission in the patient. The purpose of a collimator is to limit the photons detected to those travelling in an appropriate direction in order to produce an image in the crystal. In the majority of studies a parallel hole collimator is used, but other types may be employed for specialised tasks.

Consider the path of photons through an ideal collimator in which no photon scatter occurs and all photons entering a collimator septum are completely absorbed (figure 1.3).

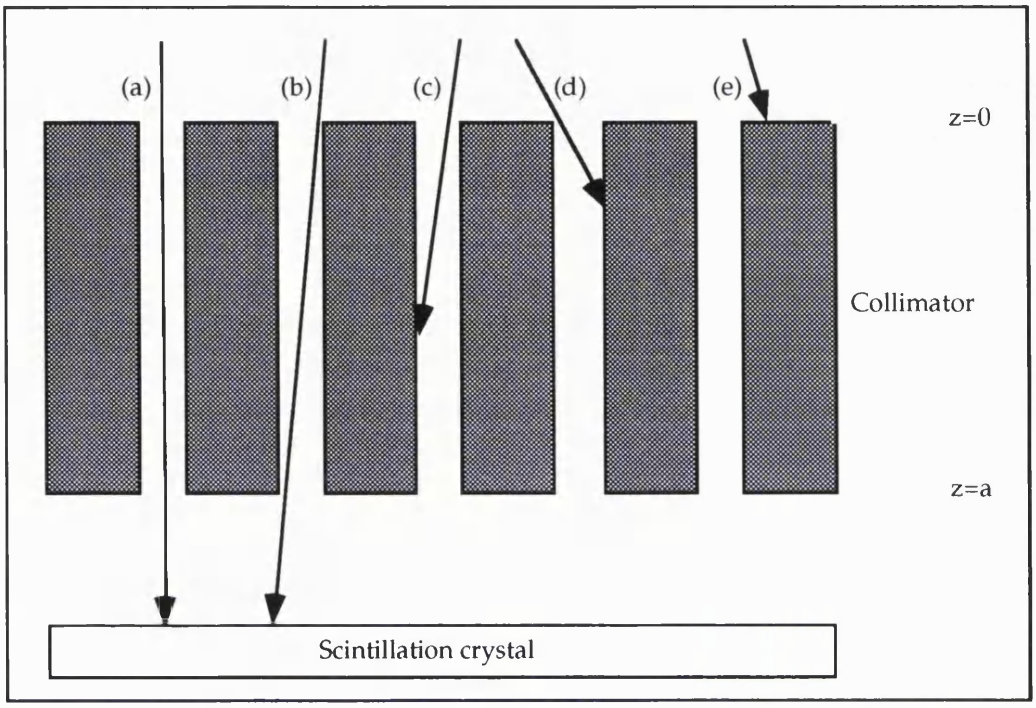

Figure 1.3 The possible paths of photons through an ideal collimator.

At the face of the collimator (z=0) photons (a) to (d) enter the collimator through a hole. Photon (e) is incident on the septum surface and is completely absorped. At z = a only photons (a) and (b) emerge, the remainder having entered a septum at some point in their path and undergoing complete absorption. If the hole width is infinitely narrow only those photons whose direction of travel is parallel to the hole wall will emerge and be detected. The finite hole size leads to a small angular range in the directions of detected photons.

1.2.4.1 Choice of collimator material

In reality, some photons entering the collimator septa will be scattered and others will penetrate the septa without undergoing either absorption or scatter (figure 1.4). The material from which the collimator is constructed should therefore have high absorption properties to minimise these effects. Lead is normally chosen as the collimator material for three main reasons. The first and most important reason as mentioned previously is that lead is a very good photon absorber. Secondly, lead is widely available and cheap. Finally, lead can be easily cast or folded into shape. In selecting a suitable material for collimators, it is necessary to consider the absorption, physical and mechanical properties of the material. It is also necessary for the material selected to be widely available, cheap and easily machinable.

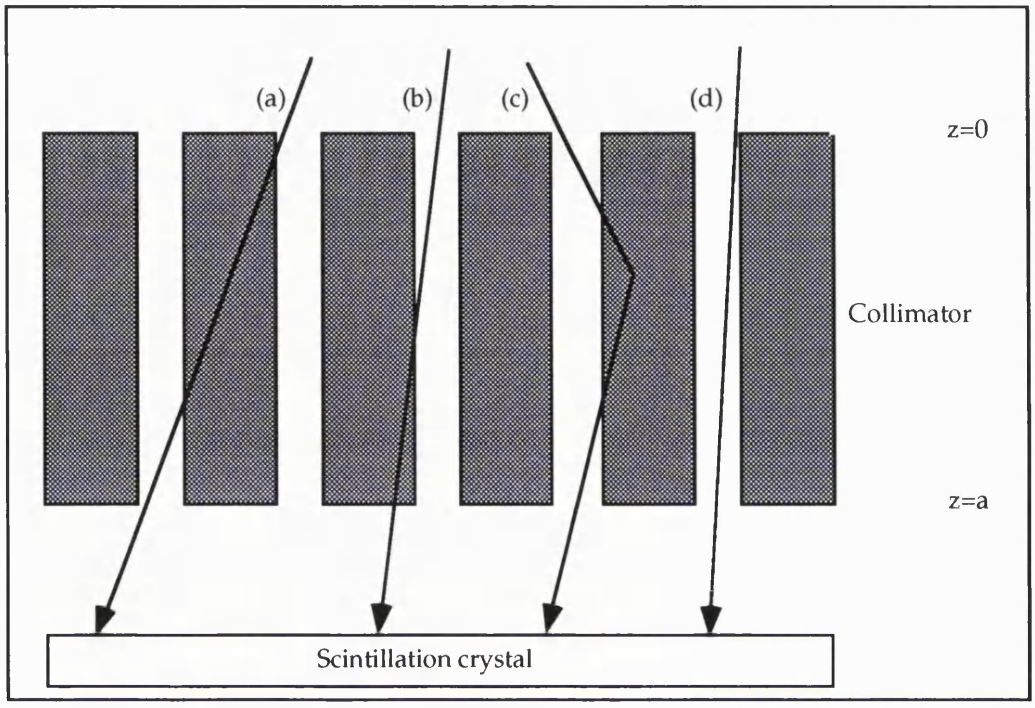

Figure 1.4 Actual photon paths through a gamma camera collimator: (a) Complete septum penetration; (b) Partial septum penetration (edge penetration); (c) Scattering in septum; and (d) Geometric path.

Since the purpose of a collimator is to absorb incident photons, the collimator material must have strong photon absorption properties. The variations of the photoelectric and Compton cross sections with atomic number for a photon energy of 140 keV are seen in figure 1.5. The photoelectric cross section per atom increases while the Compton cross section per atom decreases with increase in atomic number. From this consideration, a collimator material should have a high atomic number so that it is a good absorber of photons.

Since the attenuation produced by a layer of material is dependent on the number of electrons and atoms present in that layer, the linear attenuation coefficient μ of a material is dependent on its density ρ. This can be seen in figure 1.6 where μ and ρ are plotted as functions of Z for elements with Z ranging from 70 to 94 at E=140 keV; the value of μ for lead is indicated by the dashed line. The attenuation coefficient can be seen to be dependent both on atomic number and density.

Once a material has been selected as having suitable absorption properties for collimation it is then necessary to consider its mechanical properties. Ideally the collimator material should be strong and hard, so as to prevent damage due to maltreatment, etc. Another factor to consider is the ease with which any alternative material may be machined into a collimator. One of the methods of collimator construction is to cast the molten collimator material around pins. The melting point of a material is therefore of importance, as too high a melting point would lead to difficulties in the casting process.

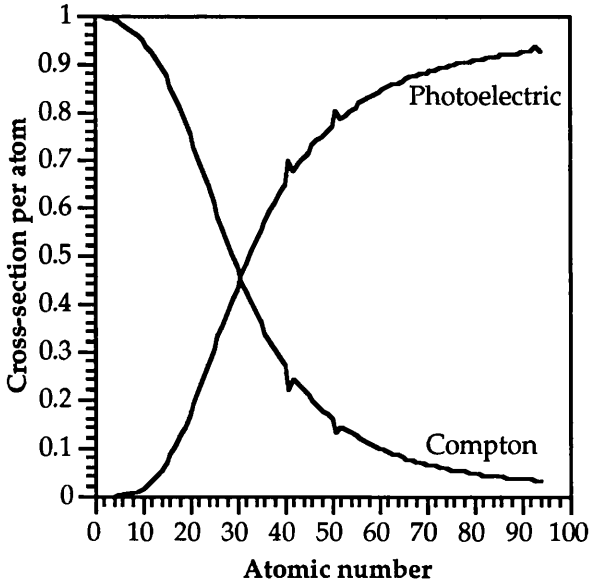

Figure 1.5 Variation in photoelectric and Compton cross-section with atomic number for a photon energy of 140 keV.

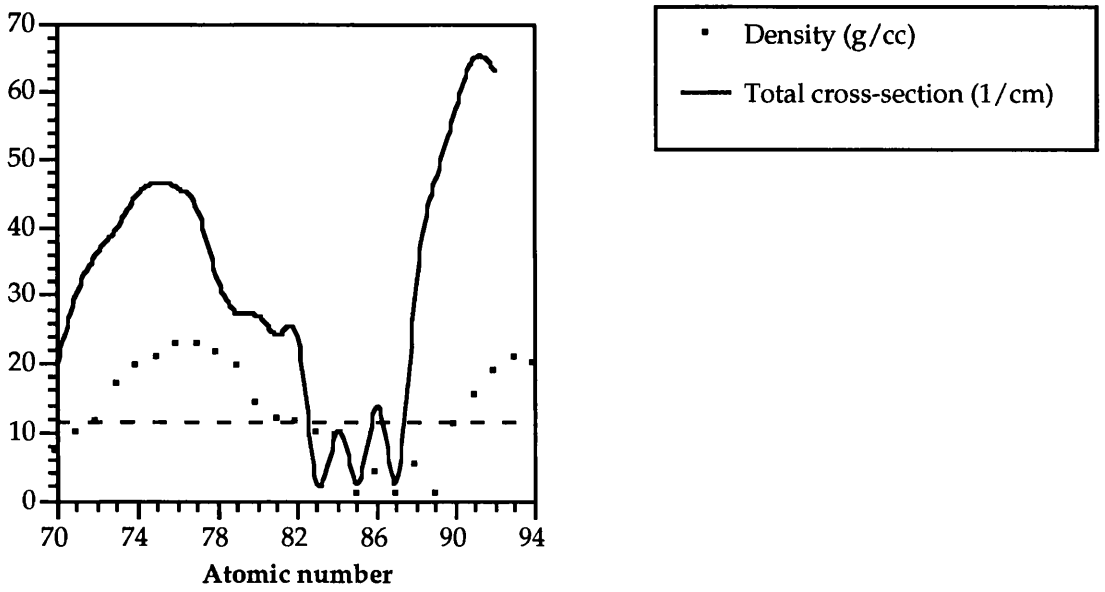

Figure 1.6 Variation in linear attenuation coefficient (for E = 140 keV) and density with atomic number for elements of Z = 70 to 92.

A major factor in the selection of a material for gamma camera collimators is the cost. Whilst all other factors may suggest its suitability, its cost may be prohibitive. Since lead is commonly used in collimator manufacture, the cost of any alternative material relevant to the cost of lead is of importance.

For a material to be suitable for use as a collimator it is therefore necessary that it has high μ values, and for it to be strong, cheap and suitable for casting. Using the μ value of lead as a standard, table 1.1 lists the materials seen in figure 1.6 whose μ values are

greater or equal to lead, giving an indication of their costs relative to lead and comments on those materials which are unsuitable for use in a collimator due to their physical and mechanical properties, etc.

Z	Name	Melting Point °C	ρ g/cm^3	Approx. relative cost	Yield strength MPa	Tensile strength MPa	Young's Modulus GPa	Comments
73	Tantalum	2996	16.6	21	705	760	186	
74	Tungsten	3410	19.3	4	550	550	411	
75	Rhenium	3180	21.0	11	315	1125	466	
76	Osmium	3045	22.5	493	—	—	559	
77	Iridium	2410	22.4	381	—	550	528	
78	Platinum	1772	21.45	423	14	125	170	
79	Gold	1064.4	19.3	479	205	130	79	
80	Mercury	-38.87	13.6	N/A	—	—	—	Liquid
81	Thallium	303.5	11.85	41	—	9	8	
82	Lead	327.5	11.35	1	5.5	12	16	
90	Thorium	1750	11.5	41	298	305	78	
91	Protact-inium	~1230	~15.37	N/A	—	—	—	V. rare, radioactive, hazardous
92	Uranium	1132.3	~11.7		250	580	176	U235 depleted

Table 1.1 Materials with suitable absorption properties for use as collimator materials.

Materials which would meet the absorption requirements are, from figure 1.6, situated around lead in the periodic table. From table 1.1 two materials are instantly ruled out, mercury and protactinium. The cost is obviously prohibitive in the case of osmium, iridium, platinum, and gold. Another possible material is thallium (Z = 81), however its attenuation coefficient is too similar to that of lead to warrant its use. The remaining materials are uranium (Z = 92), which has the highest value of μ, tungsten (Z = 74) and rhenium (Z = 75), which both have similar values of μ, and thorium (Z = 90), with an attenuation coefficient slightly lower than uranium. A discussion follows on the possible use of these materials and of lead for collimators.

Lead: Lead is the material which is currently used, normally as an alloy, in gamma camera collimators. It is a heavy material ($\rho \approx 11.35$ g cm^{-3} at 18°C), and in elemental form is very soft and highly malleable. The addition of a small amount of antimony toughens the material, but it is still prone to damage, meaning that great care must be taken during the manufacturing process, and the subsequent use of the collimator.

Uranium: Uranium has the highest atomic number of the naturally occurring elements. Naturally occurring uranium contains a mixture of U^{235} and U^{238} (0.711% U^{235}). It is used in the nuclear industry in fuel elements for nuclear reactors. Depleted uranium, so called because it has a much lower concentration of the U^{235} isotope than natural uranium, is a by-product of the nuclear industry. It contains approximately 0.3% U^{235}. It has a wide range of industrial uses due to its unique combination of properties — high density, high strength and high melting point. It is a very dense metal ($\rho \approx 18.7$ g cm^{-3} at 18°C), its density being greater than that of lead, with a high melting point.

There are several hazards associated with uranium, most noticeably the radioactive hazard. Uranium is of low specific activity and low radiotoxicity. Alpha, beta and gamma radiations are continuously emitted, however the main radiation dose comes from beta radiation which is completely stopped by 1.5 mm of steel. The dose from the gamma radiation is less than 5% of the beta dose at the surface of uranium. Alpha radiation can be stopped by nickel plating or other surface coatings. Nickel plating is also used to prevent the oxidation of uranium which occurs in air. Other hazards of uranium include a toxicity on inhalation comparable with that of lead, and a fire hazard. Although massive uranium metal offers no real problem, in a finely divided form it is pyrophoric, and care is necessary to prevent fires. For this reason when uranium is machined a rapid flow of a coolant is required to prevent swarf from igniting. The pyrophoric nature of uranium would impose a lower limit on the minimum septal thickness possible in a collimator, however this is thought to be less than 10 microns.

Another consideration in the use of uranium as a material for cast collimators is its high melting point (1132.3 °C). The total volume change from 25°C to melting point is 8.81%, a factor which would need to be considered when casting the collimator. One possible method of casting would be to cast the uranium around beryllium pins, which would remain in the collimator. The melting point of beryllium is slightly higher than that of uranium (1278°C). The permanent pins would also prevent the uranium from both oxidising and igniting. Beryllium, with its low atomic number is virtually transparent to gamma photons at 140 keV.

Tungsten: Tungsten is placed 8 elements before lead in the periodic table. Its density (19.3 g cm^{-3} at 20°C), which is similar to uranium, is higher than lead. It is a strong, hard metal (table 4.11). It has the highest melting point of all metals (3410 °C), a possible disadvantage for cast collimators.

Rhenium: From its attenuation coefficient rhenium appears a suitable material for use in collimators. It is a silvery metal having a density of 21.9 g cm^{-3} and a melting point of 3180 °C. Rhenium is an extremely hard metal, its wear resistance is good and it is not easily corroded. However, rhenium is a very rare metallic element, widely distributed in a variety of

minerals but usually in concentrations below 0.1 part per million. It has two naturally occurring isotopes Re-185 which is stable and Re-187 which is radioactive and the more abundant. Due to its rarity it would not be a viable material for gamma camera collimators.

Thorium: Thorium, which is thought to be approximately three times as abundant as uranium and therefore about as abundant as lead, is a fissionable metal and a source of nuclear power. The purest specimens of thorium contain thorium oxide, which has a melting point of 3300 °C. Powdered thorium metal is often pyrophoric. Thirteen isotopes of thorium are known, all of which are radioactive. Thorium-232 occurs naturally and has a half-life of 1.41×10^{10} years. It is an α, β, and γ emitter, and is sufficiently radioactive to expose a photographic film in an few hours. Thorium disintegrates with the production of thoron (radon^{220}), an alpha emitter which presents a radiation hazard.

From the five materials discussed above, three materials other than lead emerge as possibilities for collimator materials. Of these uranium and thorium have similar absorption properties, while the attenuation coefficient of tungsten is slightly lower. Both uranium and thorium are naturally radioactive, however the nuclear industry have unwanted supplies of depleted uranium making it more cost effective. Uranium is also stronger and harder than thorium. Because of the strength of tungsten, and its relatively high attenuation coefficient, it is also a good choice for a collimator material. In chapter three, the performance of collimators constructed from lead, tungsten and uranium will be considered from their response functions.

1.2.4.2 Collimator types

The four major types of collimator used in nuclear medicine imaging are: pinhole, parallel hole, diverging and converging (figure 1.7).

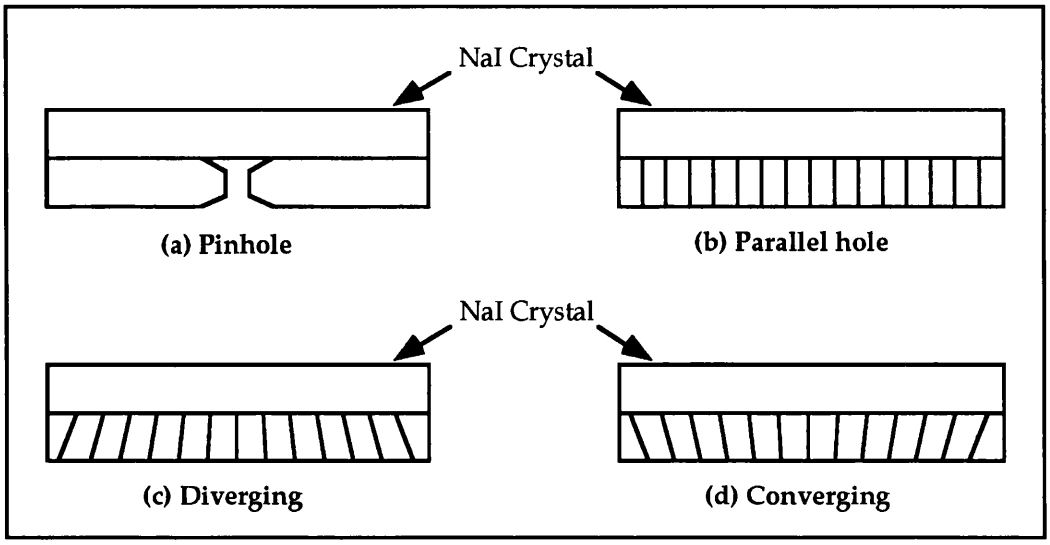

Figure 1.7 Various types of mechanical collimator.

Pinhole collimator: The pinhole collimator is identical to the optical pinhole except that the pinhole is made from lead and has a diameter of a few millimetres. The image formed in the crystal is inverted. Pinhole collimators provide good resolution for the imaging of small organs relatively close to the collimator face. As the aperture-source distance decreases, image size and efficiency increase and resolution improves. Increasing the pinhole size will improve efficiency but at the expense of resolution. The degree of penetration is increased with an increase in gamma ray energy effectively increasing hole size and so worsening the resolution.

Parallel-hole collimator: In the parallel-hole collimator the holes are perpendicular to the crystal face, so only gamma rays travelling in this direction will be detected; obliquely incident gamma rays being absorbed by the septa.
Converging collimator: In the converging collimator the holes converge towards the object so that gamma rays diverging from it are detected, forming an enlarged image. Converging collimators provide the capability of high resolution, high sensitivity imaging. The field of view is, however, small and some image distortion occurs.
Diverging collimator: Diverging collimators are primarily used to produce a reduced size image of a large organ. Both spatial resolution and sensitivity are reduced and distortion is caused by the change of magnitude with depth.

The first gamma-camera (Anger 1952) used a pinhole collimator to produce the image, however nowadays the parallel-hole collimator is used for the majority of studies, the other types being employed for specialised tasks. All but the pinhole collimator are multihole collimators and provide greater efficiency in gamma ray collection. The efficiency and resolution of collimators depend on the hole size, the septal thickness (i.e. thickness of collimator walls) and the geometry of the holes. Gamma-camera collimators can be obtained as low-, medium- or high-energy collimators. Septal thickness increases from low-energy to high-energy collimators to minimise interseptal penetration. High-energy collimators have the poorest efficiency and resolution due to the thicker septa and wider holes, respectively. If the septal thickness is too thin, gamma rays will penetrate the septal walls and reach the crystal resulting in a degradation of image contrast due to the detection of penetrated photons and an increase in detected scattered radiation.

1.3 Gamma camera imaging

The gamma camera is used for a variety of different imaging studies, both planar and tomographic. This section briefly considers some of the applications of the camera in clinical imaging. The production of images is then introduced by considering how images are formed by the uncollimated camera and by the collimator. Previous collimator studies

are reviewed considering effects such as penetration and scatter and different modelling techniques. Finally, the section suggests that the formation of images using numerical methods by combining the response functions of the individual camera components to a source distribution has advantages over a single photon transport model of the complete system.

1.3.1 Tomography and the gamma camera

Planar imaging portrays a three dimensional distribution of activity as a two dimensional image superimposing structures at different depths. The result is a loss of contrast in the plane of interest due to the presence of activity in structures from outside the plane of interest. The acquisition of several views (posterior, anterior, lateral and oblique) may aid interpretation of the image, but is not ideal. Emission computed tomography (ECT) is a technique whereby multi-cross sectional images of tissue function can be produced, thus removing the effect of overlying and underlying tissues. ECT can be divided into two general types: limited angle (or longitudinal) tomography and transaxial (or transverse section) tomography. In limited angle ECT, photons within a limited angular range are detected simultaneously from several sections of the body. The reconstruction gives images of planes that are parallel to the face of the detector. Transaxial ECT is performed using a gamma camera that, under computer control, rotates around the patient. A series of static images is obtained with the camera in different angular positions around the patient. Other systems use two or three gamma cameras mounted on a rotating gantry collecting several views simultaneously. A two dimensional image is obtained at each angular position around the patient. Rotation through 180° satisfies angular sampling requirements, however many gamma camera SPECT studies are performed with 360° rotation to minimise errors resulting from attenuation and loss of resolution with depth. Mathematical reconstruction of these images using a filtered backprojection algorithm (Budinger and Gullberg 1977) leads to a set of sections through the patient.

1.3.2 Typical clinical applications of the gamma camera

The modern gamma camera may be used for a variety of types of studies; those possible with a modern gamma camera are described below.

Single planar study : In this type of study both the patient and the camera are stationary. The image is acquired for either a preset time or a preset count. The images are normally obtained in 128 x 128 or 256 x 256 matrix size.

Static studies : These are recorded in the same manner as the single study. Any number of statics can be acquired, each view being uniquely labelled, e.g. *anterior* or *posterior.*

Dynamic studies : A series of sequential images may be acquired in order to record the changing distribution of activity within a patient. Each of these images is acquired for a preset time. Data for the first image is stored in a memory buffer, on reaching the preset

time acquisition of the second image is commenced, the data being stored in another buffer, while the first image data is stored on disk. The process is repeated until the required number of frames has been acquired. The image matrix size used is normally 64 x 64 or 128 x 128.

Dual isotope studies : Since some isotopes are multiple-energy emitters, and some clinical investigations can utilise two different isotopes (e.g. parathyroid imaging), gamma cameras have the facility to record events from more than one energy signal. These studies can be acquired in both static or dynamic mode. By a comparison of the images at the two energies a clearer image of target-organ function is obtained.

Gated studies: Gating an image is achieved by use of a physiological trigger or signal (e.g. an electrocardiograph) derived from equipment that independently monitors a physiological or physical parameter. The technique is known as Multiple Gated Acquisition (MUGA). MUGA enables a blood pool image of the beating heart to be acquired.

1.3.3 Image production in terms of camera components

The components in a gamma camera system were described in section 1.2. In this section the way in which the image is formed by the collimator and the camera is considered.

1.3.3.1 The uncollimated camera

The camera components which form the image of photons incident on the crystal are the crystal, the PM tubes, the pulse height analyser and associated electronics. The method of image production from these components was described in section 1.2. To achieve high spatial resolution from the camera a thin crystal is required, together with a large number of closely packed PM tubes. The efficiency of the camera is also dependent on the crystal thickness, a thicker crystal being more efficient than the thinner crystal required for high resolution.

1.3.3.2 The collimator

The spatial resolution and geometric efficiency can be expressed in terms of the collimator dimensions. If A is the hole length, d the hole diameter and ZA the source-to-collimator distance, then the collimator spatial resolution R_c is given by (Anger 1964)

$$R_c = \frac{d(A+ZA)}{A} \qquad (1.3)$$

Thus the spatial resolution is improved by increasing the hole length or by increasing the number of holes per unit area (providing the septal thickness is adequate) so that a large number of smaller diameter holes can be fitted into the same overall area. The spatial resolution is also improved by minimising the source-to-collimator distance.

Equation (1.3) predicts the resolution of a collimator with square holes in a rectangular array. The equation assumes the collimator to move sideways with respect to the source and detector during the exposure. The resolution calculated is the full width at half maximum (FWHM) of the response to a point source along a single direction, the line of measurement being perpendicular to a hole edge (figure 1.8). For a point spread function (PSF) averaged over all directions the hole 'diameter' would need to consider all possible paths and rotational angles of the photons.

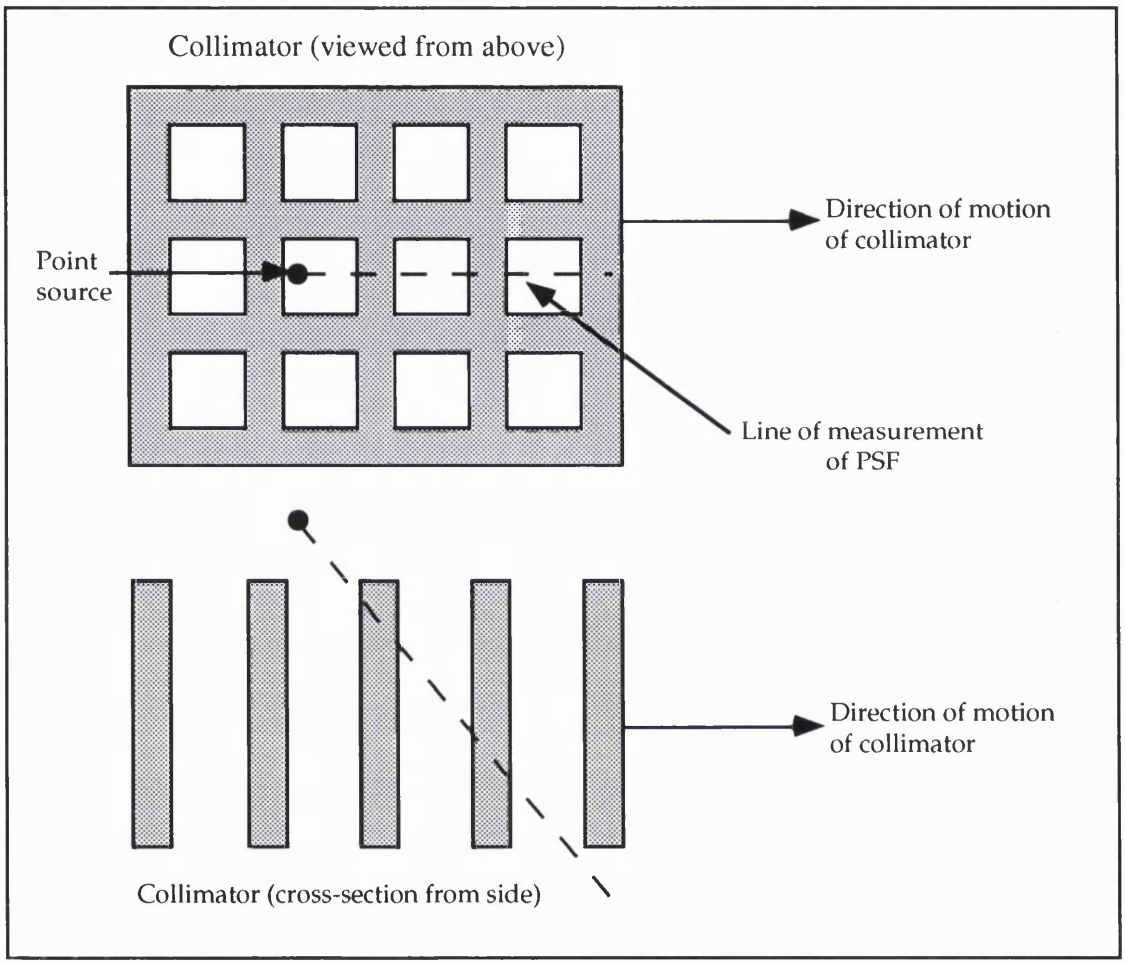

Figure 1.8 Measurement of PSF in Anger's equations (1964).

A simplified analysis of the effective hole diameter for a hexagonal hole collimator, flat-to-flat distance DF, might be as follows:

Consider a beam of particles incident sideways on a hexagon (figure 1.9a). The average distance travelled through the hexagon will be given by $\sqrt{3}\,DF/2$. For a beam of particles perpendicular to this first beam, incident on the hexagon (figure 1.9b), the average distance through the hexagon will be $3DF/4$. The ratio of the number of photons passing through the hexagon from the second beam compared with the first beam is $2/\sqrt{3}$. Thus the average distance travelled through the hexagon is

$$\frac{1}{2}\left(\frac{\sqrt{3}DF}{2}+\frac{3DF}{4}\cdot\frac{2}{\sqrt{3}}\right)=\frac{\sqrt{3}DF}{2}\approx 0.866DF \qquad (1.4)$$

Thus the effective diameter of the hole would be expected to be approximately $\sqrt{3}/2$ of the flat-to-flat hole size.

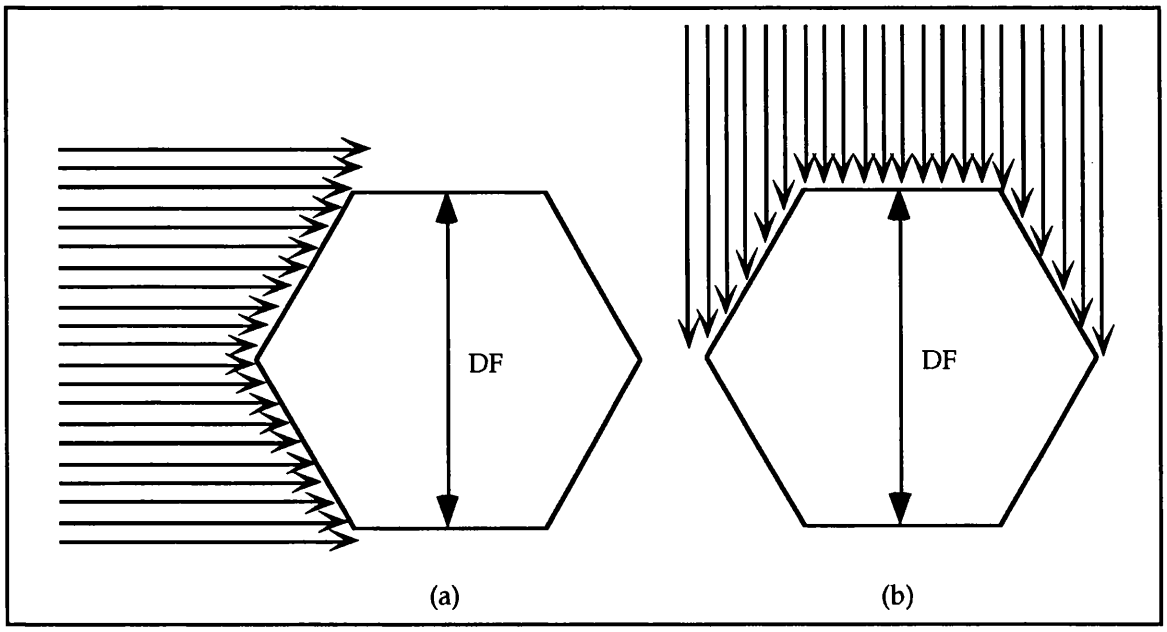

Figure 1.9 Method of calculating effective hole size.

The geometric efficiency g of the collimator is given by (Anger 1964)

$$g \sim K\left[\frac{d^2}{A(d+t)}\right]^2 \qquad (1.5)$$

where t is the septal thickness and K is a constant dependent upon hole shape and pattern. For hexagonal holes in a closely packed array $K \approx 0.26$. The efficiency is therefore independent of the source-to-collimator distance (in air) for a point source. For high efficiency thin collimators with large holes are desirable.

There are several possible methods of construction of collimators for gamma-cameras dependent on the type of collimator (e.g. parallel-holed, focused, etc.) and on the shape and layout of holes. Lead foil collimators are constructed by gluing lead foil strips together to produce the required shape. The advantage of this method of construction is that narrow septa may be easily produced. However if the construction process is less than perfect, gaps in the junction between the lead strips will allow photons to pass through the collimator preferentially along the direction of the strips (Yeh 1983, Gillen *et a;* 1988). Another method of collimator construction is to pour molten lead around pins which are later removed when the lead has set. This method of construction can lead to non-

parallelism of holes caused by individual channels not being aligned with respect to each other. This non-parallelism can lead to non-uniformity and non-linearity in the image.

Modern imaging applications such as single photon emission computed tomography (SPECT) place stringent demands on camera system performance. SPECT literature emphasises the requirements of both good uniformity (Rogers *et al* 1982) and spatial linearity (Chang *et al* 1985, 1988). The intrinsic uniformity and linearity of the camera have been improved but the uniformity and linearity of the collimation needs also to be improved. The uniformity of collimation is defined as the regional variation of the efficiency across the collimator core. Any variation in the thickness of the collimator septa or distortion or damage caused in the construction process will affect the uniformity of the collimator. The linearity of collimation is dependent on the accuracy in the alignment of each channel in the collimator. Algorithms for the reconstruction of data in SPECT assume that the collimator holes and septa are precisely perpendicular to the axis of the camera's rotation throughout the rotation. If this is not the case then a centre of rotation offset occurs. The holes must also lie perpendicular to the top and bottom so that the holes are aligned orthogonally with respect to the axis of rotation.

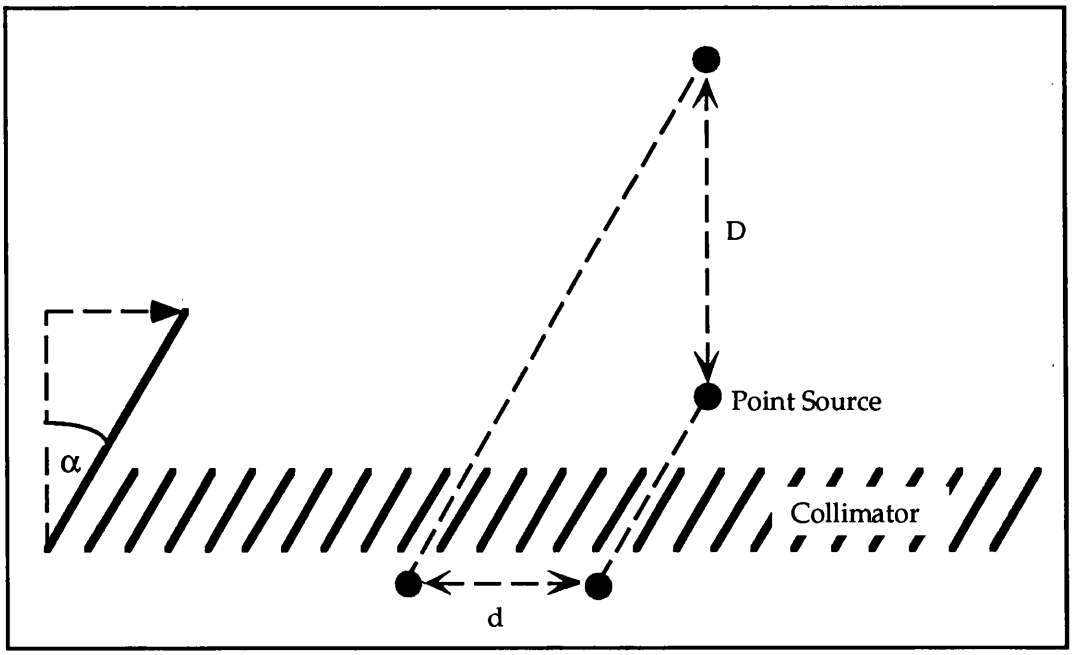

Figure 1.10 The separation of images due to the angulation of septa.

The angulation of collimator holes can be measured by imaging a radioactive point source at two different heights above the collimator surface. When the collimator holes are precisely perpendicular to the collimator face the images formed will be superimposed. A small angulation of the holes within a region (figure 1.10) will cause the images to be separated by a small distance d from which the hole angulation α may be determined using the equation $\alpha = \tan^{-1}(d/D)$. Such regional variations in the angulation of channels in the collimator lead to a degradation of resolution when SPECT images are reconstructed. For

example, a 1° channel tilt can introduce a 3.5 mm error in projection and backprojection at a distance of 20 cm (Chang *et al* 1988).

Methods exist to measure the linearity and uniformity of collimators. Collimator uniformity can be measured using a specially adapted rectilinear scanner to record the regional transmission rate of a radioactive source through a piece of collimator core on a point-by-point basis as a two-dimensional image. A slightly diverging scanning beam will reduce the system's sensitivity to small variations in collimator channel tilt (Chang *et al* 1988). Regional errors in channel angulation are measured on a gamma camera by acquiring static images of a tray of point sources at two altitudes above the collimator. The x, y coordinates of each point source at each height are determined from the data and the angulation error for each point source is determined from the shift in coordinates (Busemann-Sokole 1987). This calculation assumes that there are no sharp changes in channel tilt. The uniformity test would be more sensitive to such changes (Chang *et al* 1988).

The choice of collimator is dependent upon the study to be performed, e.g. pinhole for thyroid imaging, parallel hole for liver studies, etc., but the design of each type of collimator can affect the final image. The optimisation of the design of a gamma camera collimator is a compromise between resolution and efficiency in order to obtain the best possible image of a source distribution. Equations 1.3 and 1.5 have shown that long holes of small diameter give high resolution while short holes of large diameter produce high efficiency — hence the necessary compromise between resolution and efficiency. In practice, the spatial resolution will be worsened due to the penetration of septa by photons. To minimise this the collimator should be constructed with thick septa and long holes from a high atomic number material such as lead. The hole shape and packing is also of importance. To maximise the exposed area of the crystal face a hexagonally close packed array of round or hexagonal holes is preferred, the latter giving more uniform septal thickness throughout.

1.3.3.3 Gamma camera components: conclusions

Having discussed the function and design of the various components of the gamma-camera system it remains to determine whether improvements can be made to any of the components which will have consequences on clinical imaging. Much research has been carried out into the improvement of intrinsic resolution and intrinsic efficiency of the gamma camera (Royal *et al* 1979, Svedberg 1972, Zimmerman 1977), and data processing techniques have been investigated for the removal of spatial, energy, and sensitivity distortions in the camera (see for example Muellehner *et al* 1980, Knoll *et al* 1982, King *et al* 1985). While investigations into the camera components have advanced, little has changed in the design of the parallel hole collimator since it was first described by Anger (1964). The design of the collimator determines image quality in terms of resolution, efficiency,

uniformity and linearity. The geometric resolution of the collimator is limited by efficiency considerations, while, in addition to being limited by the geometric resolution, the geometric efficiency of the collimator is affected by the septal thickness required to prevent septal penetration. Traditionally collimators have been constructed from lead, or a lead alloy, however recently others have used tungsten or titanium or alloys of these materials to improve absorption properties. To improve geometric efficiency, while maintaining geometric resolution, it is desirable to use a material with a higher linear attenuation coefficient than lead and investigations into the design of collimators using such materials would be useful. Due to the malleable nature of lead it is very easily damaged, and it has been demonstrated that collimators whose surfaces have been inadvertently damaged by denting with small hard objects can cause significant ring artefacts in reconstructed SPECT images (Jarritt and Ell 1984). Design improvements either in the collimator material or in the use of a protecting layer are desirable to minimise such effects. Another area of concern in gamma camera collimators is how closely they match the design specifications. Studies have demonstrated (Chang *et al* 1985, 1988, Gillen *et al* 1988, Malmin *et al* 1990) that defects in collimators, such as angulation error and variations in the resolution with direction exist in commercially available collimators and have consequences in the uniformity and linearity of images, both in planar and tomographic gamma camera imaging.

The collimator limits the performance of the gamma camera imaging system more than any other individual component (Moore *et al* 1992) and therefore merits considerable attention. This thesis will investigate the conventional gamma camera collimator, using photon transport models to investigate the effects of penetration and scatter in the collimator on planar imaging. Similar models will be used to investigate the effects of collimator defects on images, and to produce images from alternative collimators, using different materials and designs.

1.3.4 Previous collimator studies and what has been achieved

The design and quality of the collimator are important to both planar and tomographic imaging. The principles of gamma ray collimation have been under investigation for many years. The properties of an ideal collimator material are that it is non-scattering and opaque to gamma radiation, however such a material does not exist. High atomic number materials such as lead approach these requirements better than other materials. There have been many investigations into the subject of penetrating radiation in collimators, for example Mather (1957) investigated the gamma ray penetration and scattering effects in a single hole collimator deriving equations for the geometric, penetration and scattering apertures of the collimator. He concluded that the computations of both penetration and scattering effects were very involved even for a single cylindrical hole collimator. It was found that penetration could be of the order of one half of the geometric effect in some situations. Anger (1964) proposed a method to determine the minimum septal thickness by calculating a minimum path length which a photon must traverse the

collimator material. The minimum path length suggested by Anger was $3/\mu$ which allowed for 5% penetration where μ is the linear attenuation coefficient of the collimator material. Other authors suggested restricting penetration to less than 1% by the use of much thicker collimator septa with a minimum path length of $5/\mu$ (Kibby 1969).

Gerber and Miller (1974) modified the equation given by previous authors (Anger 1964, Keller 1968, Walker 1969) for the calculation of the geometric resolution of a parallel hole collimator. They calculated that for a collimator that moves during the exposure, the geometric resolution (FWHM of the triangular shaped intensity distribution curve) is given by

$$R_c \approx \frac{d(A_e + ZA)}{A_e} \qquad (1.6)$$

where $A_e = A - \frac{2}{\mu(E)}$ the effective collimator length when penetration occurs, A is the collimator length and $\mu(E)$ the linear attenuation coefficient of the collimator material. The remaining variables in equation (1.6) are as defined in equation (1.3). Equation (1.6) considers the collimator hole length A to be reduced by $1/\mu$ on both ends to give A_e, the effective collimator length when penetration effects are taken into account.

The effects of edge penetration for both single hole collimators (Simons 1962, Bell *et al* 1970) and for multihole focusing collimators (Rottenberg and Johns 1965, Simons 1970) have been investigated. Myhill (1961) also included the effects of radiation penetrating the septa between collimator holes, as well as the septa edges, in his theory of the response of multihole focusing collimators. Both experimental and computer simulation techniques have been employed to investigate penetration effects. Christie and MacIntyre (1969) made experimental measurements of the line response of existing collimators using photon sources of two different energies, attributing the difference to penetration. Muehllehner and Luig (1973) used a ray tracing technique to determine line spread functions in an investigation of septal penetration in parallel hole collimators for various hole shapes. As a result of their work an existing collimator was improved by reducing the septal thickness. Similar studies have also been performed by Rotenberg and Johns (1965) and Simons (1970). The ray tracing technique has also been applied to multihole focusing collimator geometry (Jahns 1981) to determine the geometric edge penetration and septum penetration, and to the design and analysis of collimators for high-energy photons (Beck and Redtung 1985a, 1985b).

Monte Carlo techniques (described in Appendix 4) have been successfully employed in a wide range of nuclear medicine studies. Such studies include simulating the interaction of light photons in scintillation crystals for the design of SPECT systems (Bradshaw *et al* 1985), investigating the effects of scatter in medical imaging (Dresser and Knoll 1973), evaluating Compton scatter in SPECT (Beck *et al* 1982, Floyd *et al* 1985a,

1985b), and simulating photon transport in gamma camera systems (Rosenthal and Henry 1990, de Vries *et al* 1990 and Yanch *et al* 1992).

De Vries *et al* (1990) investigated the effects of high energy contaminant photons on image quality. Using a 20% I-123 energy window the authors found that photons scattered at least once in a low energy general purpose collimator comprised 27% for a Cr-51 source (320 keV) and 33% for Sr-85 (514 keV). Yanch *et al* (1992) simulated SPECT by locating a virtual sphere around a phantom and storing the position coordinates, direction cosines, energy and scatter order of a photon passing through the sphere. The photon was then cloned and allowed to interact with all collimator positions with which it would interact. Each view was simulated on a different processor to provide a highly efficient process. The energy of each photon interacting with the camera plane was sampled for a Gaussian function with a FWHM of 12% via an inverse probability distribution function, the same function being used regardless of the photon energy. Convolution techniques were used to incorporate the intrinsic spatial resolution of the camera, assuming a FWHM of 3 mm. Such methods have been described by White (1979), Heller and Goodwin (1987) and Todd-Pokropek (1980).

1.3.5 Description of images in terms of response functions

As was discussed in section 1.2 gamma camera images are formed by the effects of several of the system's components. Each of the components modifies the information from the source distribution. The way in which the information is modified is known as the response of the system. If, for example, the source distribution considered was a point source then the final image would be a blurred representation of that point source. The total response of the system is actually built up from the responses of the individual camera components. If, for example, a radiograph was taken of the photon distribution after the collimator stage, the image would show a blurring of the point source due to the range of angles of the photons after traversing the collimator. Each of the other camera components further blurs the information.

Under certain conditions, which will be considered in chapter two, the relationship between the object and the final image can be described in terms of a convolution. If the object is described by the function f and the image by the function g then the relationship between the image and the object is given by

$$g = h*f \qquad (1.7)$$

where * denotes a convolution and h is the total response of the system. This can in theory only be applied to systems which exhibit both linearity and spatial-invariance. However, even when these conditions are not satisfied it it possible to form the image from a knowledge of the object and the response functions of individual components.

1.3.6 The advantages of working in response functions compared with complete Monte Carlo

One approach to numerically modelling a gamma camera system is to model the system by tracing individual photons from their origin until they are either photoelectrically absorbed in the collimator or crystal, or they reach a boundary beyond which they cannot be detected. In a single numerical model any light photon produced by the absorption in the crystal would then need to be traced to the photocathodes of the PM tubes, after which the electrons created would need to be followed through the PM tube dynode structure. The Anger logic circuitry and PHA would then require modelling before the final image could be obtained. Such a model would obviously be very complicated and would require lengthy CPU times due to numerous inefficiencies inherent in the system, the most prominent being the collimator inefficiency. Other inefficiencies exist such as non-absorption of photons by the crystal. In addition, for each different source distribution or collimator structure, it would be necessary to simulate the complete system from photon generation to image production.

The use of individual response functions can greatly simplify this procedure, eliminating some of the inefficiencies and reducing run times considerably. It is possible to measure the intrinsic response function of the uncollimated camera experimentally. The camera approximates a linear system permitting the formation of an image by the convolution of the camera response function with the photon distribution at the crystal face. The problem then remains of determining the photon distribution at the crystal face. Chapter two will discuss the fact that a typical patient and collimator system does not exhibit the spatial-invariance required to use the convolution technique. It is still however possible to obtain the collimator response to a point source and to combine it with the distribution of photons at the collimator surface to produce the distribution in the crystal. Although this technique does require both the determination of the collimator response by numerical simulation and the photon distribution at the collimator face, it has the advantage that a study of the effects on images of different collimators can be rapidly achieved for a particular source distribution without requiring the simulation of photon transport from the source through each collimator.

1.3.7 The collimator function

The collimator was discussed in section 1.3.3.2. Equation (1.3) indicated the dependence on the source height of the collimator resolution for an ideal collimator. From this equation it is evident that any collimator response function could only be valid for a particular source height. For a three dimensional source distribution a different collimator response function would be required for each z-plane of activity in the source distribution.

In addition to the three dimensional nature of a typical source distribution, in a practical situation scatter will occur within the object. This scatter has two effects. The first is that the response of the collimator is dependent upon the photon energy. Thus although

the ideal response of the collimator is independent of energy, the actual response is dependent on energy due to the penetration and scatter fractions of the response, and so photons scattered within the object have a lower probability of penetrating the collimator than primary photons. The second effect caused by scatter within the object is a change in the source distribution. In the ideal situation of no scatter, the object can be viewed as a distribution of isotropically emitting point sources. When scatter occurs, in addition to these point sources, there exists a generally anisotropic, inhomogenous distribution of scattered photons of various energies. Thus, whereas the collimator response to an ideal source distribution can be formed by the convolution of the point spread function with a distribution of point sources, the point spread function cannot be used for the scattered distribution. The way in which a response function which deals with photons scattered within the object is obtained will be discussed in detail in chapter 2.

In conclusion a realistic collimator function is not in fact a single function but rather a series of response functions to various effects, such as source height and the effects of photon scatter within the object.

1.4 The aim of the current work

The purpose of a gamma camera collimator is to limit the direction of travel of photons to a small angular distribution to produce an image of high spatial resolution. Unfortunately, consideration of efficiency means that the angular range of photons produces a deteriation in the spatial resolution. In addition, however, to the inherent defects in collimators, other defects exist which arise from poor design or manufacture or from maltreatment of the collimator. This thesis investigates the effects of such defects on images. As an introduction to collimator defects this section presents an overview of literature on the subject. Following this the material covered in the thesis is set out.

1.4.1 Consideration of collimator defects

The effects that collimator defects have on images have been investigated by several authors. Bonte *et al* (1971), for example, discovered image aberrations during a study of the quality of the image produced using multihole collimators, both parallel and diverging. Two parallel hole collimators were used, one designed for technetium studies (2.5 mm square holes, 0.5 mm septa), and the other for higher energy radioiodine studies (6 mm diameter round holes, septa 2 mm thick at thinnest point, holes perpendicular to the crystal at centre of collimator, inclination increasing with distance from the centre). Images of a parallel line source using the high energy parallel hole collimator and the diverging collimator indicated an interference pattern in the form of a Moiré pattern that distorted the parallel line image. The effect decreased with an increase in phantom-to-collimator distance, disappearing at a distance from it. The study showed the interference pattern to be a property of all camera

collimators that had thick septa and linear arrays of collimator holes. The authors suggested either the use of lower energy collimators and emitters or the movement of the collimator during exposure (Bramlet 1970, Wilks *et al* 1969).

A Moiré pattern distortion was also observed by Yeh (1979) when imaging a bar-phantom. Yeh observed that an image of a bar-phantom using a medium-energy collimator and a flood source of Tc-99m showed much better delineation of the bars than one using a lower-energy collimator. However, on examination of the image it was found that fewer bars were present than should have been. The bar-phantom consisted of four quadrants with the width and spacing of bars decreasing in successive quadrants whereas the scintiphoto of the medium-energy collimator showed the width and space to increase in successive quadrants. The distortion could have lead to the misconception that the medium-energy collimator represented better resolution than did a lower-energy collimator. In a subsequent study, Yeh (1983) observed a star-shaped artefact when imaging a point source using a low-energy parallel-hole collimator. Instead of the six point star which was expected due to septal penetration, the image had eight points, two of which were extended. An investigation of the collimator showed two clefts at opposite angles of each hole, the direction of the clefts corresponding exactly to the two extra points in the image. The bar-phantom was imaged at different orientations to evaluate the effect on the resolution of this polarity. The result was that the resolution appeared best when the bars were parallel to the collimator's polarity suggesting that image distortion due to polarity can impair gamma camera resolution.

A similar star shaped artefact was observed by Gillen *et al* (1988). An image of a point source contained four lines of varying intensity passing through the centre of the image and extending across the whole field of view. The collimators examined were lead foil collimators. The most intense line in the PSF was found to be due to gaps in the junction between the foil strips allowing photons to pass preferentially in that direction. The least intense line, which was perpendicular to this, was due to photons having to penetrate a double thickness of lead. The two remaining lines, at 35° to the most intense, were found to be due to the stretching of holes during the manufacturing process. Measurement of the resolution along the most intense line gave a FWHM of 2 mm greater than the manufacturer's specifications.

With the advent of rotating gamma camera SPECT, more stringent demands were placed on system performance and correction techniques. The effects of detector non-uniformity on SPECT images have been discussed by several authors (Muehllehner *et al* 1980, King *et al* 1985) leading to an improvement in the intrinsic uniformity and intrinsic spatial linearity of commercial cameras (Chang *et al* 1988). A consideration of the intrinsic system performance alone is however inadequate since it is the collimator that imposes the most severe limitations on the overall system performance, the effects of certain parameters affecting SPECT much more drastically than planar imaging. For instance, regional variations in hole channel tilt in a parallel hole collimator, undesirable in planar imaging, can cause projection errors in data sampling in SPECT (Chang *et al* 1985). A hole channel tilt

of 1 degree (commonly given as the manufacturing accuracy) can produce an error of 3.5 mm in projection and backprojection for a source distance of 20 cm. A method of examining collimators for variations in hole channel tilt for both parallel hole and slant collimators has been described by Busemann-Sokole (1987). The angulation was determined by measuring the shift in the image of a point source at two different source heights. A similar method was employed by Chang *et al* (1988) who also measured collimator uniformity using a rectilinear scanner which has several advantages over measurement by a gamma camera or radiograph. The scanner has excellent intrinsic uniformity and whereas the limited intrinsic resolution of the gamma camera often masks the high-frequency components in the collimator's uniformity response, the scanner has reasonably high frequency response. Excellent resolution would be attainable by taking a radiograph, however quantification of global or regional uniformity would be difficult.

Angulation errors in collimators have also been deduced by viewing changes in count density (Malmin *et al* 1990). The technique compared the experimental PSF to a least squares fit of a model of the theoretical PSF of a perfect collimator. Deviations in the measured PSF and hence the count density can be related to changes in the angle between the vector from the septum location to the point source and the septal direction vector. Using the results a correction for collimator linearity is possible in the reconstruction method.

Much of the work carried out in the investigation of collimator defects has been the experimental examination of existing collimators for hole angulation (Farrell *et al* 1984, Busemann-Sokole 1987, Chang *et al* 1988, Gillen *et al* 1988). In the SPECT simulation performed by Malmin *et al* (1990), rather than performing a collimator simulation of hole defects, a normal distribution of errors was added to the image location of a point source in each simulated SPECT projection and the data recostructed. This thesis will present a method of modelling collimator hole angulations directly, calculating the effects on planar images of various degrees of hole angulation.

1.4.2 Layout of thesis

The purpose of the work carried out for this thesis was to investigate the various effects that collimators have on image formation in gamma cameras. To achieve this several different collimators have been investigated. Conventional lead collimators for low energy general purpose imaging have been modelled and images obtained for one of these collimators. The effects of defects in conventional low energy general purpose collimators have also been modelled. In addition collimators constructed from different materials and of different designs have been simulated and their images compared with those of the conventional collimator.

Chapter two of the thesis deals with the modelling and measurement of the response functions of the collimator and camera. Methods of image formation are investigated. Individual components in the imaging system are discussed together with the ways in which each component degrades the image. The computer model devised of a collimator is

described and verified and typical results are discussed. Modifications to the collimator model are discussed that will enable several different types of collimator to be simulated. A phantom for assessing image quality is described together with the method used for image formation.

Response functions of collimators are investigated in chapter three. Firstly, perfect conventional collimators of various septal thicknesses are modelled and the contribution of primary, penetrated and scattered photons to the response functions are considered. The degradation to collimator response caused by misalignment of holes is discussed, response functions being obtained for several different hole angulations. As an investigation into alternative collimator designs, two types of layered collimator are then modelled. The purpose behind these designs is to construct more rigid collimators which are lighter but produce responses which are comparable with that of a conventional lead collimator. Finally, alternative material collimators are modelled, with a view to improving collimation properties.

Images of line source phantoms produced by the collimators modelled in chapter three are presented and compared in chapter four. The effects on the images of penetration and scatter are discussed. The resolution and linearity of the images are determined.

Chapter five considers the contrasts detectable with the collimators whose resolutions and linearities are considered adequate for imaging. From these measurements conclusions are drawn as to the viability of the use of these collimators in clinical imaging.

The conclusions drawn from the work are presented in the final chapter and suggestions for future work discussed.

- 2 -

System response function - measurement and modelling

The individual components of the gamma camera were discussed in chapter one together with the importance of investigating collimator design. This chapter will present methods of producing gamma camera images using numerical modelling. The imaging system will be considered to consist of three main components — the object to be imaged, the collimator and the gamma camera. A method of image formation will be discussed that will use a combination of the individual responses of the collimator and the camera to a point source to form the image of a source distribution within an object. Particular attention will be paid to a numerical model of a collimator which will enable various collimator designs and defects to be simulated. The collimator model will be verified both experimentally and theoretically. To determine the effects that different collimators have on images it is necessary to have an object to image. For this purpose a numerical model of a source distribution within a scattering medium is presented, and verified experimentally. The method of image analysis that will be used throughout the thesis will then be introduced. The numerical simulations of the object and collimator and the method of image formation and analysis will be used in subsequent chapters of the thesis.

2.1 Monte Carlo modelling of photon transport

Many physical processes are random in nature giving rise to probability distributions of their occurrence. Such processes may be simulated by the generation of random numbers from these known probability distributions. These techniques are known as Monte Carlo methods. Monte Carlo methods are commonly used from studying photon or electron histories and have many applications in medical physics, for example absorbed dose calculations, determination of the efficiencies of gamma-ray detectors, etc. (Andreo 1991). A Monte Carlo simulation of photon transport of photon transport is a sequence of random number choices: distance to next collision, type of collision process and photon trajectory and energy subsequent to the collision. A description of the use of Monte Carlo modelling for photon transport is given in appendix 4.

Two types of Monte Carlo modes of photon transport were available for use. The first system was developed in the Academic Radiation Physics Group, UCL. The system simulates the radiation transport of photons through any medium. A routine for photon generation is supplied by the user as are routine modelling geometries. The probabilities of interaction are determined using photon cross-section data (Storm and Israel 1970).

The interactions simulated are photoelectric absorption, Compton scatter and coherent (Rayleigh) scatter. These three interaction processes are described in appendix 3. The photoelectric process simulated is a complete absorption of the incident photon, the characteristic photon and photoelectron. The Compton scatter routine is modelled using the rejection technique (Khan 1956). The Klein-Nishina description of Compton scatter is used in this technique to determine the energy deposited by the photon and the resulting direction of the scattered photon. Coherent scatter is simulated using an inversion-rejection technique (Williamson and Morin 1983). The technique determines the coherent scattering angle. Form factor data of Hubbel *et al* (1975) is used to modify the scattering processes.

The second type of Monte Carlo system available was the Electron-Gamma-Shower (EGS4) Monte Carlo package (Nelson *et al* 1985). The EGS4 system is a general purpose package to simulate the radiation transport of photons, electrons and positrons in any element, compound or mixture. Many physical processes may be modelled including Compton and coherent scattering and the photoelectric effect. The production and transport of K- and L-edge photons is possible but will not be used for programs described in this thesis. In an EGS4 code, individual particles are followed until they either escape from the system geometry or their energy falls below a given cut-off energy (Jenkins *et al* 1988). A system geometry is described by using geometrical routines available in the EGS4 system.

These two Monte Carlo systems were used for the computer models described in this thesis. Initially only the first (the UCL system) was available and was used for the collimator model. Subsequently the EGS4 system became available and was used for the simulation of source distributions within scattering media. Comparisons between the two systems at photon energies of 140 keV and lower have yielded similar results, justifying the use of either system at these energies.

2.2 System description using response functions

A complete numerical model of a gamma camera system would be very lengthy. The model would require tracing each photon from its origin in the patient through the collimator, simulating interaction processes. If the photon was to pass through the collimator without being absorbed its transport in the crystal would require simulation and the scintillation photons created would then need to be followed to the PM tubes. Multiplication of the photoelectrons in the dynode structure, the Anger logic and the PHA window levels would be simulated, an image being formed from the acceptable signals. Such a model would obviously be very complicated and would require a lengthy run time. This section deals with methods of forming an image which require less CPU time than a complete Monte Carlo and enable the easy substitution of different components.

2.2.1 Methods for image formation

A common method for numerical image formation is the use of linear systems theory which considers the image to be formed from the individual components of a system by means of simple convolutions. If this were applicable to a gamma camera system, the convolution of the source distribution function, collimator response function and intrinsic camera response function would produce the image. However two requirements of linear systems theory are that the imaging system be both linear and shift-invariant. Linear systems theory is described in appendix 2. A linear system is one in which if two or more inputs are simultaneously applied the output is given by a function dependent on a combination of those individual inputs. The system is shift-invariant if the imaging process is independent of the location of the input within the object plane. Although no imaging system exhibits perfect linearity and shift-invariance, many approximate both requirements well. If the system is linear and shift-invariant, then the final image can be constructed from the convolution of the response functions of each of the components.

In the case of a gamma camera imaging system, shift-variance is present in all components. One source of shift-variance is in the scintillator detector and PM tubes. The resolution varies over the surface of the crystal, being poorer when a photoelectric absorption is located directly under a PM tube and degrading at the edges of the crystal.

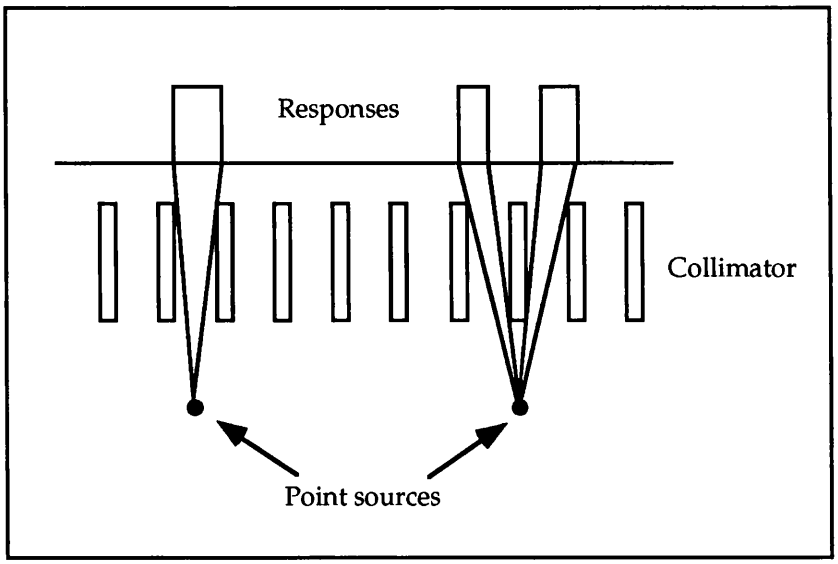

Figure 2.1 Shift-variance of a parallel hole collimator.

The collimator is a second source of shift-variance. Figure 2.1 shows that the image of a point source is dependent on the location of the source relative to the collimator, indicating that the collimator is in fact shift-variant. This problem can be overcome if an average collimator response function is calculated by determining the response when a point source is moved to all possible source locations, thus producing

shift-invariance. However if an imperfect collimator is considered, the response of the collimator may vary across its surface, causing further shift-variance.

The major source of shift-variance however is the patient; the two main reasons for this are the presence of different scattering media in the patient and the variation in the thickness of the patient. The shift-variance caused by these factors cannot be removed by any averaging properties.

Linear systems theory is therefore applicable to limited components of a gamma camera system. If the distribution of photons in the crystal is known the theory may be applied to form the system image by convolution with the intrinsic camera response. A technique is required to obtain the photon distribution in the crystal from a knowledge of the object and the collimator. The major requirement of this technique is that it is faster than a complete Monte Carlo simulation of the situation while still providing a similar degree of accuracy. The technique should also permit the generation of images from a variety of different objects and collimators and because of this it would be advantageous if the two did not require simulation each time a different combination of object and collimator was used. From this consideration, it was decided that for each object to be modelled, a Monte Carlo simulation would obtain the photon spatial, angular and energy distributions on a plane parallel to the collimator but external to the object. Also for each collimator to be modelled a computer simulation would obtain the average response functions of the collimator to a point source located on the collimator surface for a range of photon energies. The combination of the photon distribution from the object with the collimator response functions will then provide the photon distribution in the crystal for convolution with the intrinsic response of the camera to form the final image. The simulations required for these processes will be described in the remainder of the thesis.

2.2.2 Components in the system and resolution degradation

Any gamma camera image is formed by the contributory effect of various components. The imaging system can be reduced to three main components; the source distribution within the patient, the collimator response and the response of the camera. This section considers each component in turn and the way that each degrades the image.

2.2.2.1 The source distribution

Any imaging system requires an object to image and in a nuclear medicine study this object is the distribution of radioactivity within the patient. The gamma ray energy must be sufficient for photons to penetrate several centimetres of tissue but low enough for the photons to be absorbed by the crystal. Energies between 50 keV and 300 keV satisfy this requirement, with an energy of about 150 keV being ideal.

Photons emitted in the patient would ideally travel undeviated to the collimator. In practice, however, interactions will occur in the surrounding body tissues. In soft tissue at these energies Compton scatter is the dominant interaction. At the collimator face there

will be both primary, unscattered photons and secondary, scattered photons. The scattered photons will have energies ranging from the photon peak energy downwards. Scattered photons that pass through the collimator and are stopped in the crystal will degrade the image since the position from which the photon originated will appear to be the scattering site and not the emission site.

2.2.2.2 The collimator response

The function of a gamma camera collimator is to allow only those photons travelling along certain directions to reach the crystal. Photons not travelling in the required direction should ideally be photoelectrically absorbed in the collimator septa before reaching the crystal. In the case of the parallel hole collimator, photons travelling in any direction other than parallel to the collimator walls should not reach the crystal. Any photons that reach the crystal and are not travelling in the preferred direction can only degrade the image. The collimator determines the efficiency, resolution and uniformity of the final image. The spatial resolution and geometric efficiency of an ideal parallel hole collimator were given in equations (1.6) and (1.7). For perfect resolution a very narrow long hole would be required in order to limit the direction of travel of photons to that exactly parallel to the septa walls. This would produce a very inefficient collimator. This unavoidable trade off between resolution and efficiency can only serve to degrade the spatial accuracy of the image.

In practice, collimators deviate from this ideal behaviour and some gamma rays will penetrate the septal walls and reach the crystal. Penetrated photons lead to a degradation of the image since they are travelling in a direction which is not defined by the holes of the collimator, i.e. the ray is not perpendicular to the collimator surface. Other photons which enter the lead septa will scatter in the collimator before reaching the crystal resulting in a further degradation in image contrast due to both the direction of the photon and its energy.

2.2.2.3 The intrinsic response

The responses of several camera components are combined to produce the intrinsic response. These components are the scintillation crystal, the photomultiplier tubes and the electronics of the camera.

The ideal situation for photon detection in the scintillation crystal is that each photon incident on the crystal will have its full energy deposited in a single interaction. This would require each photon to undergo a photoelectric absorption in the crystal as the first interaction and subsequent absorption of the characteristic photon. If the crystal is too thin then not all photons will be stopped in it leading to a decrease in the detected photon intensity with increase in energy. Compton interactions within the crystal will result in only partial energy deposition giving the effect that a greater number of lower energy photons are present than is the case. If a photon undergoes either single or multiple Compton scatter within the crystal and the residual scattered photon is

subsequently detected the events contribute to the photopeak, since all the energy of the original photon is absorbed in the scintillator. The scintillation from the first Compton electron is correctly positioned on the path of the original gamma ray, but the other scintillations are located a distance away. The computed position of all the events will be their centre of gravity. In practice this effect is small and can be ignored at the energies used in nuclear medicine (Anger and Davis 1964). Although pulse height analysis eliminates photons with energies outside the energy window, coherently scattered photons and Compton scattered photons that have only undergone a small deviation will still lie within the acceptable limits. Typically, a window equal to 20% of the peak energy value is used, e.g. for Tc-99m with photon emission at 140 keV energy signals between 126 and 154 keV are acceptable, this corresponds to a scattering angle of up to ~55°.

The number of optical photons reaching the photocathode of a PM tube will be Poisson distributed. The generation of photoelectrons in the PM tube is also governed by a Poisson process thus producing the overall result that the signal from the tube has a Poisson distribution causing a loss in resolution (Knoll 1989).

Although it is possible to deduce the collimator response from measurements of the system and intrinsic responses there is an advantage to being able to numerically model the collimator to obtain the response.

2.3 Numerical modelling and experimental measurement of response functions

This section will discuss the computer models of the collimator and source distribution, giving a basic description of the models together with verification of the results. A description of the measurement of the camera response will also be given.

2.3.1 The collimator response

The UCL Monte Carlo system introduced previously has been used to simulate the gamma camera collimator. The model describes a parallel hole collimator whose geometry and material are defined by user supplied input. The parallel hole collimator was selected for simulation as it is the most widely used type of collimator in nuclear medicine imaging. While it is possible to experimentally obtain the response of a collimator to a line source by deconvolution of the intrinsic response from the total camera response the result obtained is applicable only to the collimator measured and is therefore dependent on the dimensions and quality of that collimator. Numerical calculations will enable different collimator designs to be prepared before a prototype is constructed and tested experimentally. Anger (1964) provided equations (1.6 and 1.7) which approximately describe the geometric properties of resolution (FWHM) and efficiency in terms of the collimator thickness, hole size and septal thickness for parallel

hole collimators. The shape of the geometric component of the PSF can be obtained by analytical calculation (Barrett and Swindell 1981, Metz *et al* 1980) and the penetration component of the PSF can be determined by ray tracing techniques (Muehllehner and Luig 1973, Beck and Redtung 1985b, Newiger and Jordan 1985). Using Monte Carlo techniques to simulate photon transport through the collimator the effects of scatter in the collimator (in addition to the geometric and penetration response components) can be investigated (de Vries *et al* 1990, Rosenthal and Henry 1990). The purpose of the investigation by de Vries *et al* (1990) was to study the effect of high-energy contaminant photons on gamma camera imaging. For ease of implementation their Monte Carlo code simplified the hexagonal collimator structure by modelling square holes and then scaling the geometric component of the response by an appropriate factor to account for the different geometric efficiency. Such a technique requires the assumption that the penetration and scatter components of the response are independent of hole shape. While this has provided a useful indication of the contribution of scattered photons from the high energy contaminants it alters the shape of the geometric component of the response and cannot accurately predict the penetrated and scattered components since these must be affected by the shape and size of the septa in the collimator.

2.3.1.1 Requirements of the collimator model

In the discussion on collimators given in chapter one, the actual performance of a collimator deviated from that of an ideal collimator due to the contribution of penetration and scatter. While the contribution of penetration can be determined using ray-tracing techniques, methods such as Monte Carlo simulations are required for modelling the contribution of scatter in the collimator.

The problems due to collimator defects have also been discussed previously, in particular the misangulation of holes in the collimator. A model incorporating such angulations will enable their effects to be assessed more quantitatively than is possible by experimental techniques.

A third area that requires simulation is the investigation of different collimator designs. It is useful to use Monte Carlo simulations of different designs to assess whether the quantity of penetration and scatter is altered by changing the collimator design. The simulation of collimators constructed from different materials is also of interest. Once again, if Monte Carlo techniques are employed, it is possible to gain information on the degree of penetration and scatter obtained.

There are therefore several requirements for the collimator model. The first is that it accurately models photon transport through a parallel hole gamma camera collimator by simulating photoelectric absorption, Compton and coherent scatter, and that the response obtained give the spatial distribution of photons at the crystal in terms of the geometric, penetrated and scattered response of the collimator. It is also necessary for the

collimator model to be able to simulate collimator hole angulations as well as new collimator designs. The simulation of various collimator materials is also required.

2.3.1.2 Description of collimator

A parallel hole collimator consists of a regular array of holes enabling its geometry to be described by the arrangement of several small pieces of the collimator known as unit cells. Investigations made on the unit cell are equally applicable to the collimator as a whole. Figure 2.2 shows a unit cell for a hexagonal hole collimator. The collimator simulation program describes the collimator by means of a unit cell and contains several subprograms describing various parts of the unit cell.

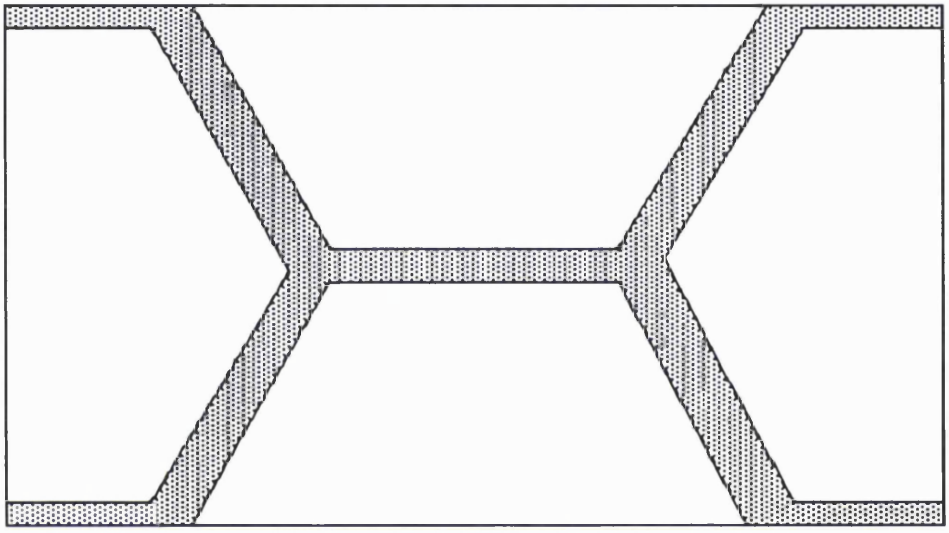

Figure 2.2 The unit cell.

2.3.1.3 Conventional parallel hole collimator model

The collimator model described here will produce the rotationally averaged response of a cast, parallel hexagonal hole collimator to a point source, the lateral position of which is chosen randomly within the confines of a unit cell in order to provide a response which is independent of the relative position of the source to the collimator at a given height. This removes any artefacts due to the hole structure of the collimator.

A flow chart of the model is given in figure 2.3. In the flow chart the circled numbers identify connections between program parts.

When a photon history is initiated its initial direction and position are selected first. For each azimuthal angle τ many photon histories are followed. The angle τ is chosen such that successive groups of photons will intersect the crystal plane at equal incremental distances providing they are not scattered (figure 2.4). For each angle τ the rotational angle θ of successive photons is incremented by a small constant amount. The

initial photon coordinates are chosen by generating two random coordinates within the unit cell to set the position of the ray at the entrance face of the collimator.

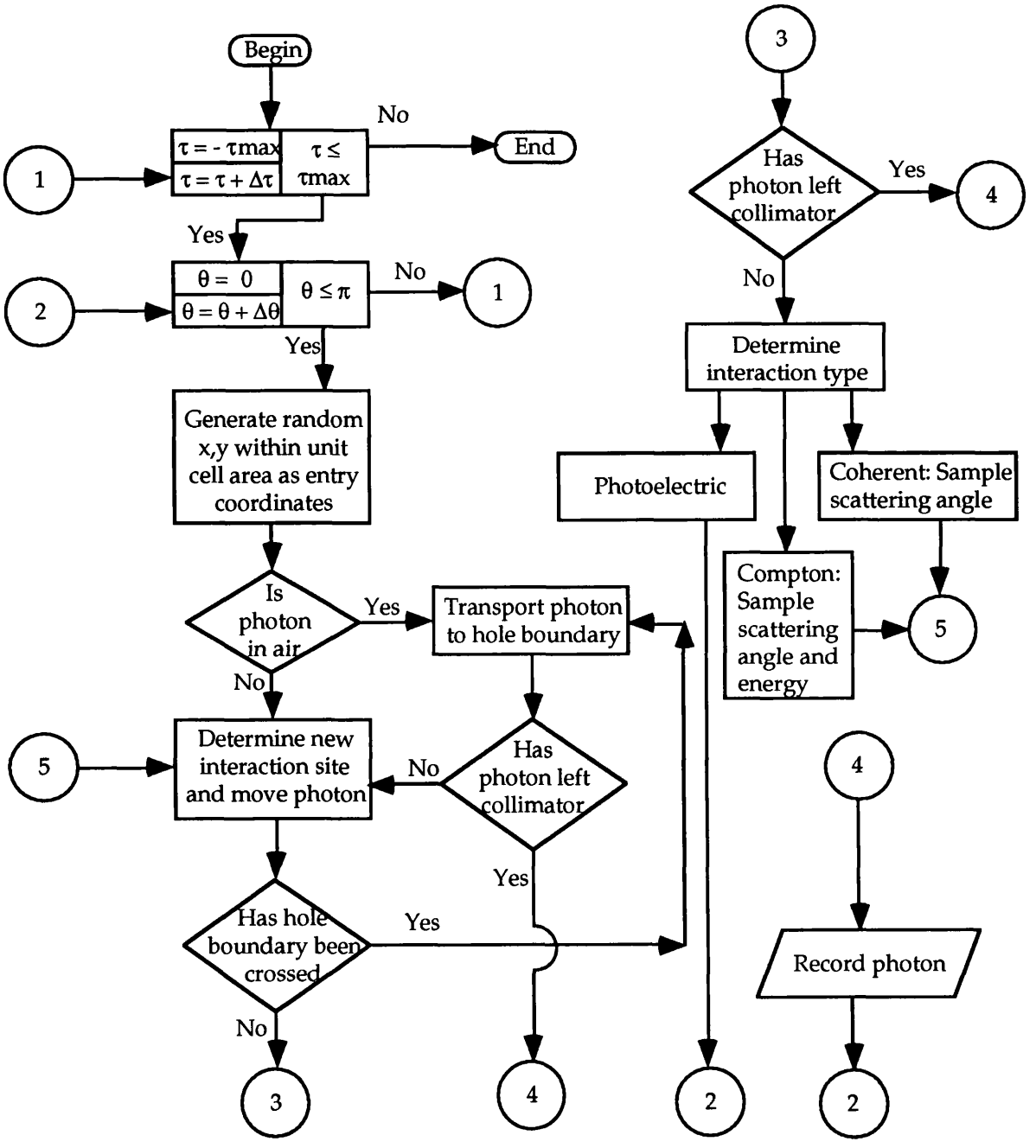

Figure 2.3 Flow chart of collimator simulation.

Having determined the direction of the photon and its coordinates, a geometric test is applied to determine whether the photon impinges on lead or air on entering the collimator. If the photon is incident in air, it is transported along its line of travel until a boundary with lead is reached. Having determined that the photon is in a lead septum, the coordinates of the interaction are calculated using the inversion sampling technique. A test is applied to determine whether the photon will have crossed a hole boundary before reaching the interaction site. If a boundary has been crossed then the photon is transported, without interaction, to that hole boundary and from there to the next

boundary with lead. If the calculated interaction coordinates are, however, reached by the photon before a hole boundary is crossed then, if the photon is still in the collimator, its interaction type is determined.

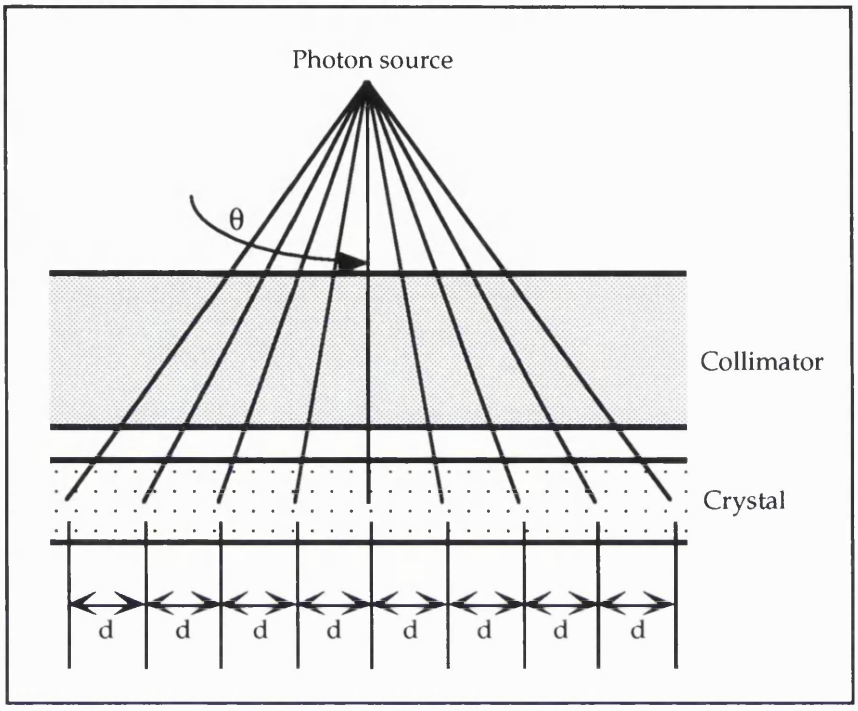

Figure 2.4 Directions in which photons are traced through the collimator are chosen such that if no scatter occurs then the photons will intersect the crystal plane at equal incremental distances d.

The photon interactions simulated include photoelectric absorption, coherent scatter and Compton scatter. The type of interaction is determined by generating a random number r* and applying the following conditions:

(a) if $r^* \leq \left(\frac{\sigma_{coh}}{\mu}\right)$ then coherent scatter occurs,

(b) if $\left(\frac{\sigma_{coh}}{\mu}\right) < r^* \leq \left(\frac{\sigma_{coh}}{\mu} + \frac{\tau}{\mu}\right)$ then a photoelectric interaction occurs,

(c) if $r^* > \left(\frac{\sigma_{coh}}{\mu} + \frac{\tau}{\mu}\right)$ then a Compton interaction occurs,

where $\frac{\sigma_{coh}}{\mu}$ and $\frac{\tau}{\mu}$ are the relative probabilities of a coherent scattering event and a photoelectric event occurring, respectively.

Having selected the interaction type, the photon is either terminated (in the case of photoelectric absorption) or its new direction is determined along with any change in photon energy. If the photon has not been terminated then a new interaction site is determined and the whole process repeated. When a photon is terminated a new photon is generated from the source, until the required number of photons have been traced.

The location of a photon within the collimator is determined by means of a unit cell structure. The equation of each plane in the unit cell is described by the direction cosines of a normal to the plane and a point on the plane, and is stored in a subroutine specific to that plane. As a photon enters the top face of the collimator the index of the unit cell in which it is incident is determined, together with the particular hole or lead region containing the photon. If the coordinates of entry are in a hole the coordinates of intersection of the photon path with the first lead boundary on its path are determined. If the new coordinates lie within the collimator the Monte Carlo routine is entered and the path of the photon followed until it leaves the collimator.

Consider a unit cell in a perfect collimator. The equation of a plane in the unit cell is described by the equation of a line normal to the plane and the coordinates of a point on the plane.

The equation of a hole edge in the x-y plane (figure 2.5) is given by

$$L_1x + M_1y + N_1z = P_1 \qquad (2.1)$$

where $P_1 = L_1x_1 + M_1y_1 + N_1z_1$

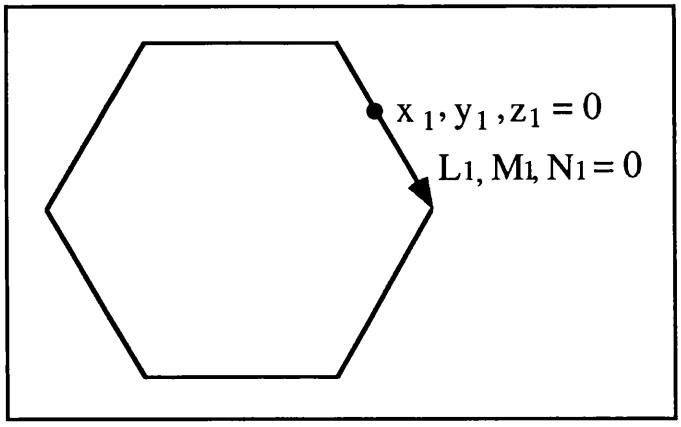

Figure 2.5 Description of a line in the x-y plane.

Since the edge is in the x-y plane, $N_1 = 0$, thus

$$L_1x + M_1y = P_1 \qquad (2.2)$$

where $P_1 = L_1x_1 + M_1y_1$.

The equation of a normal to this edge (figure 2.6) where $L_1 = 0$ and $M_1 = 0$ is

$$N_2z = P_2 \qquad (2.3)$$

where $P_2 = N_2z_2$.

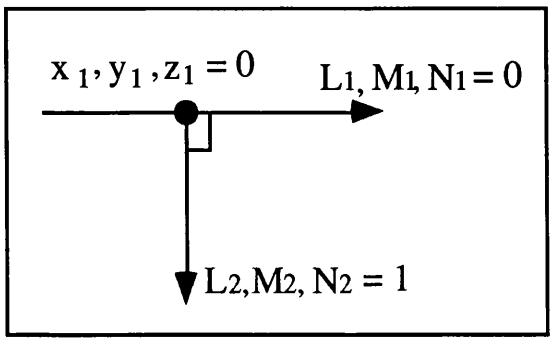

Figure 2.6 Description of two perpendicular lines in a plane.

The line which describes the plane is also normal to the lines described above (figure 2.7).

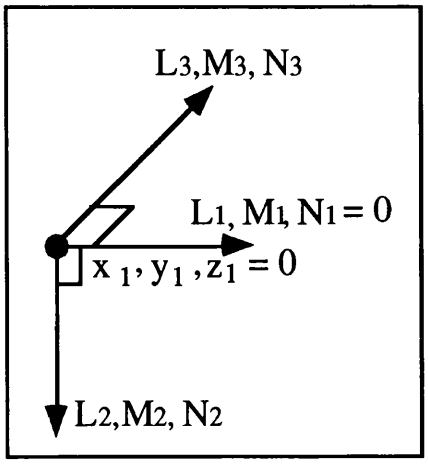

Figure 2.7 Description of a plane using three perpendicular lines and a point.

For this line the following conditions will hold:

$$L_1L_3 + M_1M_3 + N_1N_3 = 0 \tag{2.4}$$

$$L_2L_3 + M_2M_3 + N_2N_3 = 0 \tag{2.5}$$

$$L_3^2 + M_3^2 + N_3^2 = 1 \tag{2.6}$$

Substituting the direction cosines for line 2 into equation (2.5) gives

$$N_3 = 0 \tag{2.7}$$

Hence substituting into equation (2.4) gives

$$L_1L_3 + M_1M_3 = 0 \tag{2.8}$$

Using equation (2.6) in equation (2.8) we have

$$M_3 = -\frac{L_1L_3}{M_1} \tag{2.9}$$

which by substitution into (2.6) gives

$$L_3 = \pm \frac{M_1}{\sqrt{L_1^2 + M_1^2}} = \pm M_1 \qquad (2.10)$$

Hence the direction cosines of the line normal to the plane are given by

$$\begin{aligned} L_3 &= \pm M_1 \\ M_3 &= \mp L_1 \\ N_3 &= 0 \end{aligned} \qquad (2.11)$$

2.3.1.4 Output from simulation

For each azimuthal angle τ the intensity of photons reaching the crystal is recorded. This intensity is divided in order to provide information on the histories of the photons. The following response functions are recorded for each azimuthal angle:

(i) *Geometric response function:* The number of photons detected which have passed through air alone;

(ii) *Penetrated response function:* The number of photons detected which have passed through lead without undergoing any form of scatter;

(iii) *Single coherent response function:* The number of photons detected which have undergone a single coherent interaction alone;

(iv) *Single Compton response function:* The number of photons detected which have undergone a single Compton interaction alone;

(v) *Multiple coherent response function:* The number of photons detected which have undergone multiple coherent interactions but no other interactions;

(vi) *Multiple Compton response function:* The number of photons detected which have undergone multiple Compton interactions but no other interactions;

(vii) *Mixed scatter response function:* The number of photons detected which have undergone both coherent and Compton interactions;

(viii) *Total photon response function:* The total number of photons detected.

In addition to this for each angle τ traced out, the photon intensity recorded in 5 keV energy intervals is recorded, listing the intensities according to the partial response functions listed above.

2.3.1.5 Modification to collimator code for simulation of hole angulation

Two types of unequal septa defects exist. One is that seen in lead foil collimators where gaps may exist between the collimator junctions. The other type of unequal septa defect is seen in cast collimators where the hexagonal channel is inclined to the vertical. Thus the channel may be hexagonal along its length but the channel will be inclined to

the vertical. A cross-section through any horizontal plane would indicate a distorted hole shape. This hole misalignment has been modelled using a Monte Carlo simulation and the method used is described below.

To model the types of defect seen in cast collimators, the basic Monte Carlo model which describes a perfect collimator is used with some minor modifications. The method assumes all holes to be inclined to the vertical by the same angle, γ, i.e. it models a slant hole collimator (figure 2.8). Thus a horizontal cross-section through the collimator would indicate distorted holes but a cross-sectional view at an angle γ to the horizontal would indicate correctly shaped holes.

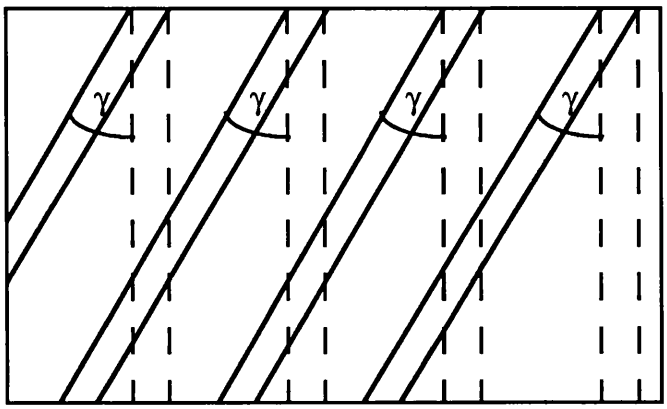

Figure 2.8 Slant hole collimator.

This slant holed collimator is modelled by considering the holes to lie parallel to the vertical axis with the top and bottom surfaces of the collimator inclined at an angle γ to the horizontal. There are thus two coordinate systems, one rotated with respect to the other by an angle γ (figure 2.9).

The coordinates (x, y, z) and angles (τ, θ) of photons in the two coordinate systems are linked by the matrix equations

$$\begin{pmatrix} x \\ y \\ z \end{pmatrix} = \begin{pmatrix} \cos\gamma & 0 & -\sin\gamma \\ 0 & 1 & 0 \\ \sin\gamma & 0 & \cos\gamma \end{pmatrix} \begin{pmatrix} x' \\ y' \\ z' \end{pmatrix} \qquad (2.12)$$

and

$$\begin{pmatrix} \theta \\ \tau \end{pmatrix} = \begin{pmatrix} \cos\gamma & -\sin\gamma \\ \sin\gamma & \cos\gamma \end{pmatrix} \begin{pmatrix} \theta' \\ \tau' \end{pmatrix} \qquad (2.13)$$

In order to model a slant hole collimator such as this N photons are emitted at each azimuthal angle τ'. The angle τ' is chosen such that successive groups of photons will intersect the crystal plane at equal incremental distances providing no scattering occurs. For each angle τ' the rotational angle θ' of successive photons is incremented by a small constant amount. The initial photon coordinates are chosen by generating two

random coordinates within the resolved unit cell (figure 2.10) to set the position of the ray at the entrance face of the collimator.

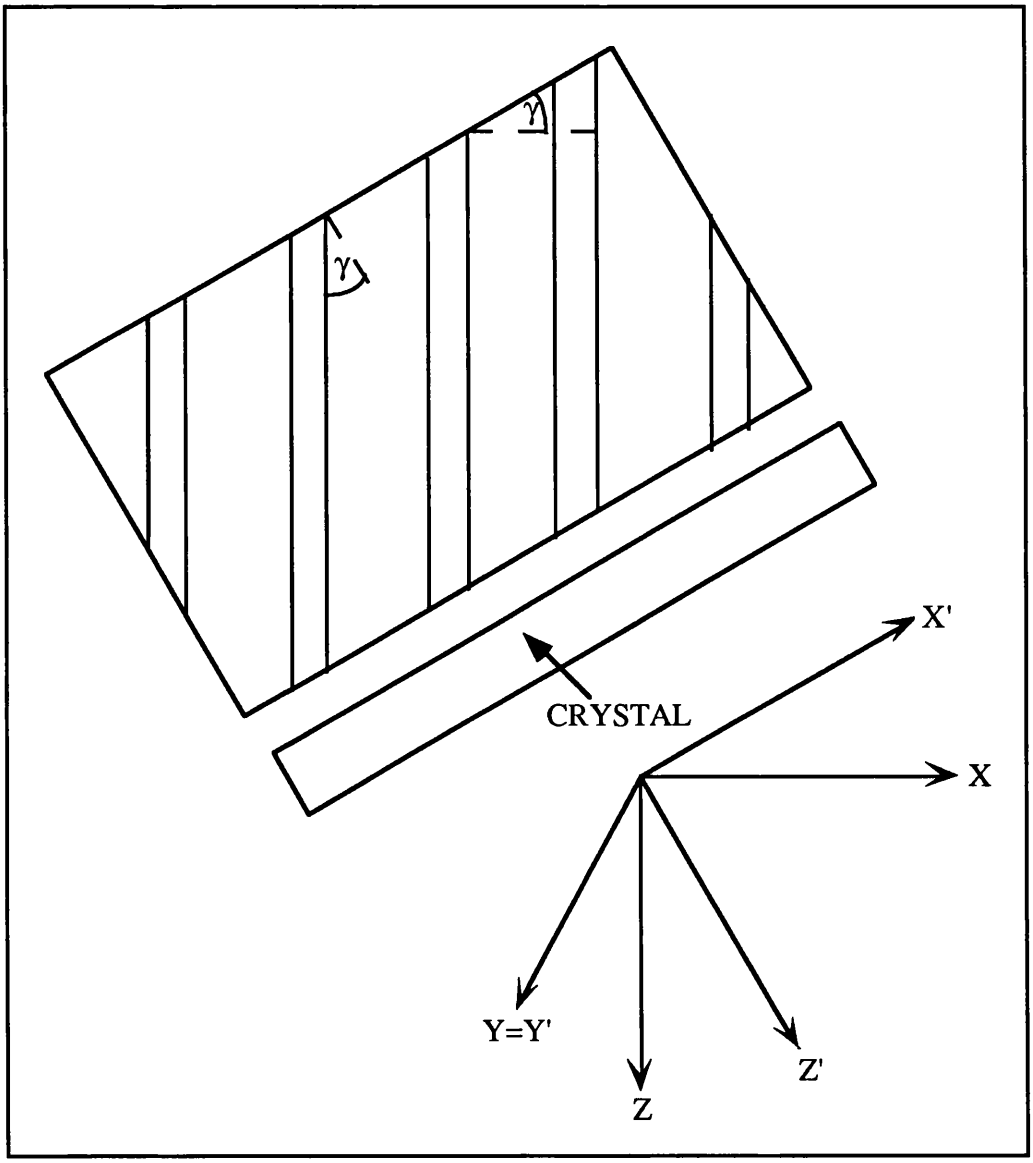

Figure 2.9 Model for computer simulation of cast collimator defects showing rotated coordinate system.

Having selected (X', Y', Z') and (τ', θ') for a photon, the coordinates and direction the photon has in the coordinate system corresponding to the holes is calculated: (X, Y, Z) and (τ, θ). The photon is traced through the collimator using the same method as that described in section 2.3.1.3 until it leaves the collimator (again considering the lower surface of the collimator to be slanted).

2.3.1.6 Modification to collimator code for simulation of layered structures

In modelling a layered structure the basic collimator design (hole shape, size and length) remains unaltered but the layered structure needs to be incorporated in the model;

thus the only change required in the code is the inclusion of a variable number of layers of two different types of material. The thickness of each layer is also a variable. A flow chart showing the main changes to the code is shown in figure 2.11; the numbered circles refer to the same points as in figure 2.3. Once the entry coordinates have been determined the test is made to see whether the photon is in air (top of figure 2.11). The photon is traced through the collimator as with the conventional collimator, however tests are made to determine whether the photon is in lead or in the second material.

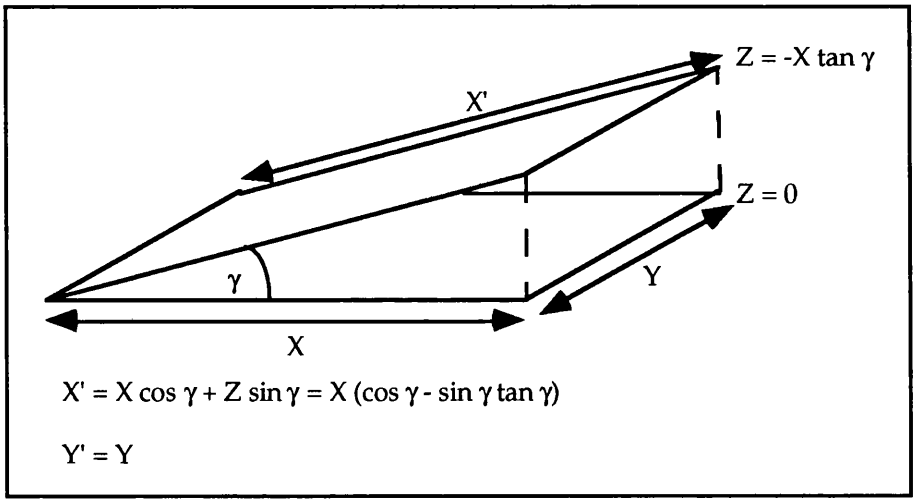

Figure 2.10 The resolved unit cell.

2.3.1.7 Modification to collimator code for simulation of alternative materials

In modelling photon transport through collimators of alternative materials no changes need to be made to the Monte Carlo code for the conventional collimator, however, the cross-section and form factor data used need to be altered.

2.3.1.8 Experimental validation of the collimator code

In order to test the program, the response of a collimator to a source approximating a point source was measured experimentally using the apparatus shown in figure 2.12. The radiation sources used were technetium-99m and americium-241.

The single hole response of the collimator to a point source scanned in a straight line above the collimator face is determined using this apparatus. The lead mask used is 2.2mm thick and is attached to the collimator so as to isolate the central hole. This thickness of lead provides only 0.1% transmission at 140 keV. Photon detection is performed using a Canberra planar high purity germanium detector. The crystal area is sufficiently large to ensure that all photons which pass through the hole of the mask are detected. The detector output is passed to a Canberra 2020 spectroscopy amplifier which feeds the pulses to a multichannel scaler (MCS). The MCS is interfaced to an IBM compatible PC. The MCS used is the EG&G ORTEC 913 ACE MCS card.

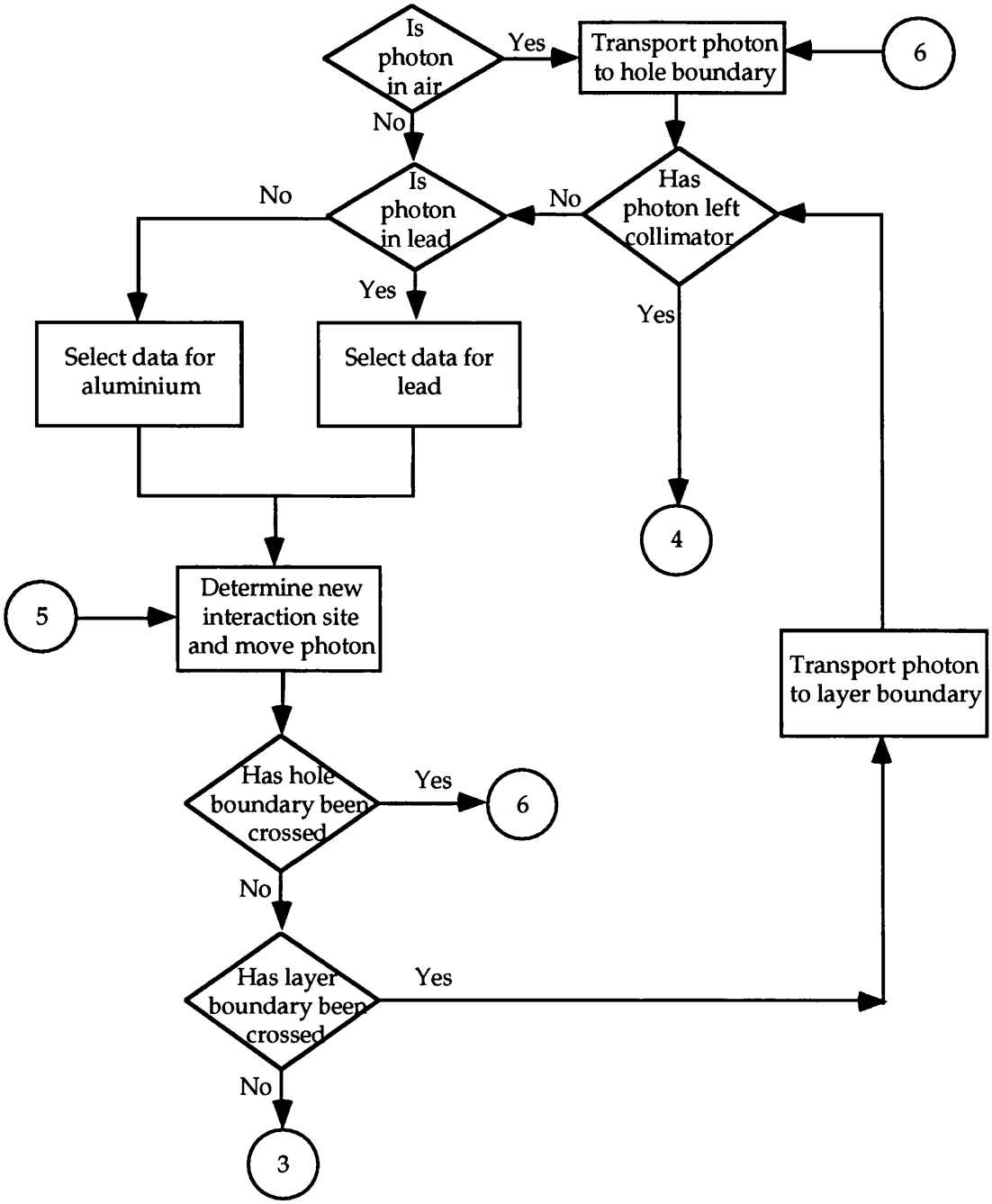

Figure 2.11 Flow chart of changed code for layered collimator simulation.

The source is held in a variable height source holder resting on a fine screw thread driven by a computer controlled stepper motor. This screw thread rests on another screw thread also computer controlled which is perpendicular to the first thread. Programs written in GWBASIC on a PC interfaced to the stepping drive unit for controlling the stepper motors allow the source to be moved in incremental steps in either the X or the Y direction. Data are collected at each incremental source position on a line.

The experiment proceeds in the following way. The computer sends a signal to the stepper motor drive to move the source rapidly a given distance. When this movement is complete a channel advance signal is sent from the drive unit to the MCS to begin counting. An energy window is set to count all photons within an energy range of ± 10%

of the source energy. The source is held stationary for a set period of time. When this dwell period is complete the process is repeated. A plot of intensity versus time was obtained.

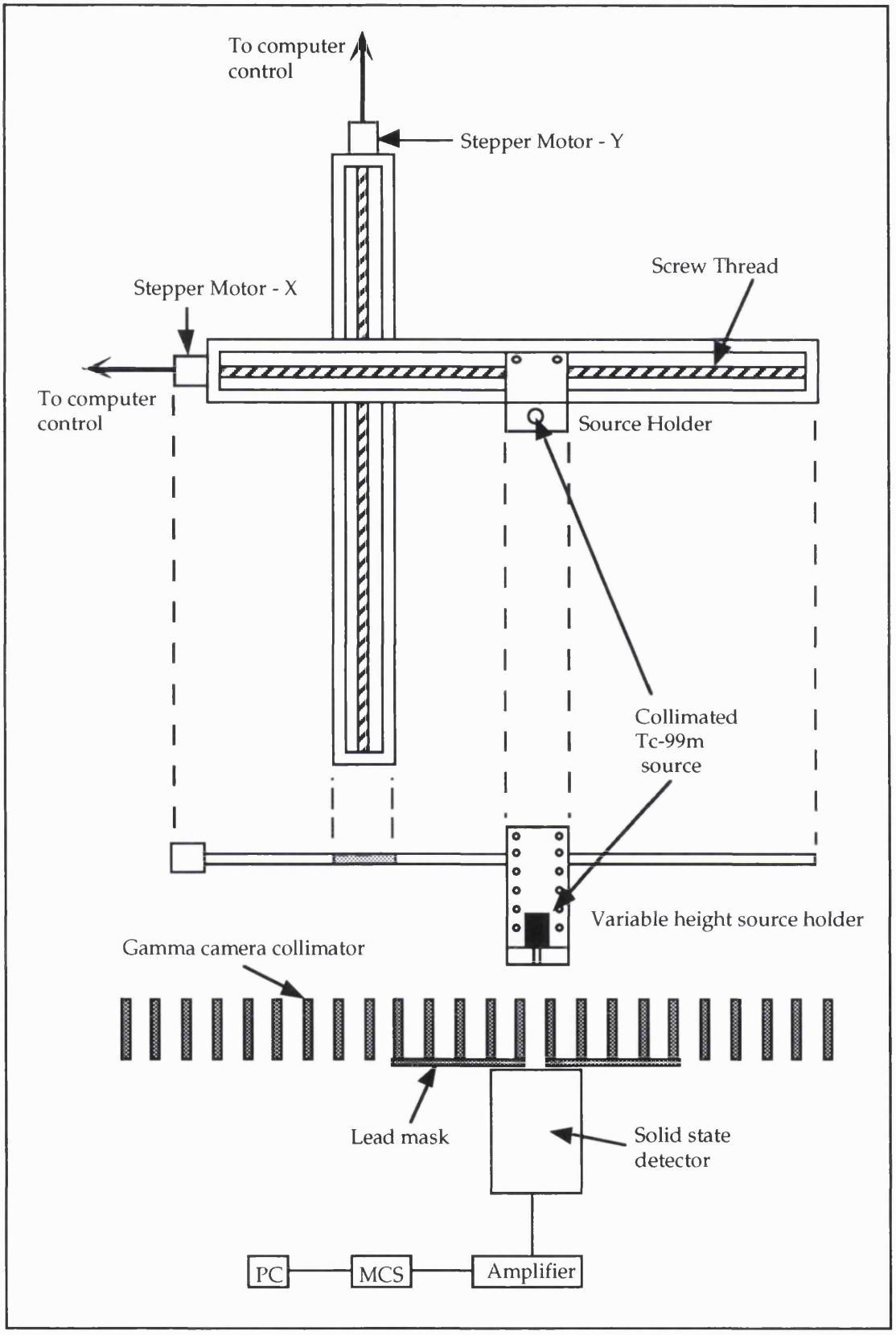

Figure 2.12 Experimental test apparatus

In order that the data collected need not be corrected for the source decay, the dwell period is a variable determined according to the elapsed time since the start of the scan. Thus the greater the time elapsed the longer the dwell period. The dwell period for a particular position is determined in the following way. Given that at any time t, the number of radioactive nuclei is

$$N(t) = N_0 e^{-\lambda t} \tag{2.14}$$

where N_0 is the number of radioactive nuclei at time $t = 0$,
and the decay constant $\lambda = \frac{\ln 2}{t_{1/2}}$ where $t_{1/2}$ is the half life of the isotope.

If the scan started at time $t = 0$ and the initial dwell period was INDW then the number of decays CO in this period is given by

$$\begin{aligned} CO &= \int_{t=0}^{t=INDW} N(t) = \int_{t=0}^{t=INDW} N_0 e^{-\lambda t} \\ &= \frac{N_0}{\lambda}\left[1 - e^{-\lambda * INDW}\right] \end{aligned} \tag{2.15}$$

Subsequent dwell periods are calculated such that there will be CO decays in that time. Hence if the current time is $t = t_3$, then the time t_4 at which the dwell period should end such that CO decays will have occurred is determined in the following way:

$$\text{Let } CO = N_0 \int_{t_3}^{t_4} e^{-\lambda t} \tag{2.16}$$

then using equation (2.15) gives

$$\frac{N_0}{\lambda}\left[1 - e^{-\lambda * INDW}\right] = \frac{N_0}{\lambda}\left[e^{-\lambda t_3} - e^{-\lambda t_4}\right] \tag{2.17}$$

which gives the end of the dwell period to be

$$t_4 = -\frac{1}{\lambda}\ln\left(e^{-t_3} + e^{-\lambda * INDW} - 1\right) \tag{2.18}$$

The initial activity of the Tc-99m source used was approximately 1200 MBq in 0.3 ml. The stepper motors were scanned a distance of 0.3 mm between readings (240 steps at 2000 steps/second). The initial dwell time used was 180 seconds. The source was scanned from a distance of 3.6 mm from the centre of the isolated hole to the centre. These measurements were made for various source heights over the range 0 cm to 20 cm.

In order to compare the computer code with the experimental measurement some changes were required to the code. The changes made were in the initial photon conditions. A simulated source was scanned along a horizontal line, source positions being separated by 0.3 mm increments. At each source position 10^5 photons were emitted. The source was considered to have a diameter of 3 mm and initial photon

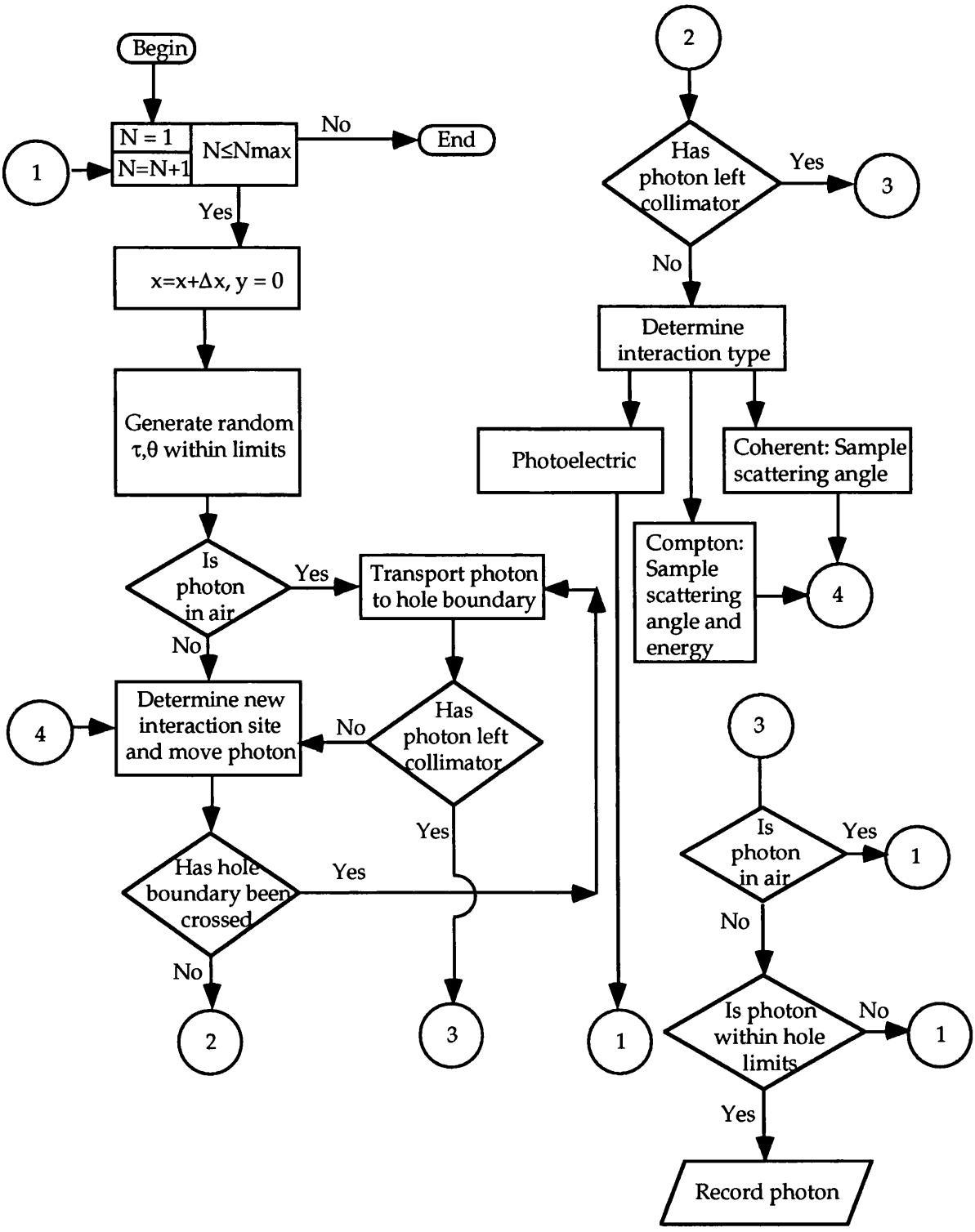

Figure 2.13 Flowchart of Monte Carlo code for comparison with experimental measurement.

coordinates were randomly selected within this width. The dimensions, geometry and scanning simulates exactly the experimental conditions. An isotropic source distribution was simulated, the azimuthal angles generated being limited to simulate the collimated source. The code defining the collimator geometry and the passage of photons through the collimator is unchanged. Once the photon has exited the collimator, a decision is

made as to whether the photon will be detected. To simulate the lead mask which is placed on the lower surface of the collimator in the experimental setup, only those photons which on leaving the collimator pass through the isolated hole are counted in the program. A flow chart of the program is shown in figure 2.13; as before the circled numbers denote a connection between program parts. The response functions recorded are the same as those given in section 2.3.1.4.

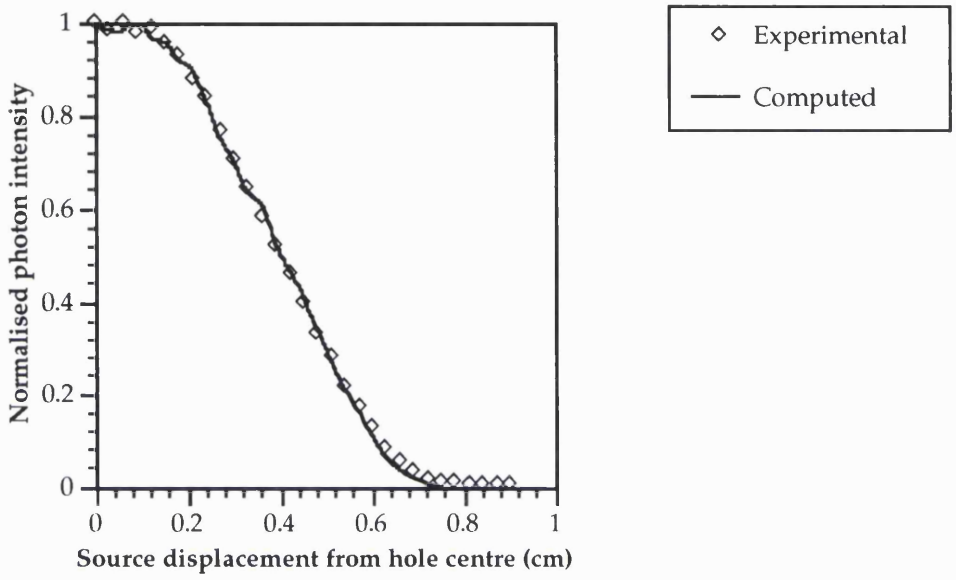

Figure 2.14 Experimental and simulated photon intensities as a function of source position for a technetium source at a 10 cm height. Collimator hole size 0.25 cm flat-to-flat, septal thickness of 0.03 cm and hole length 4.1 cm.

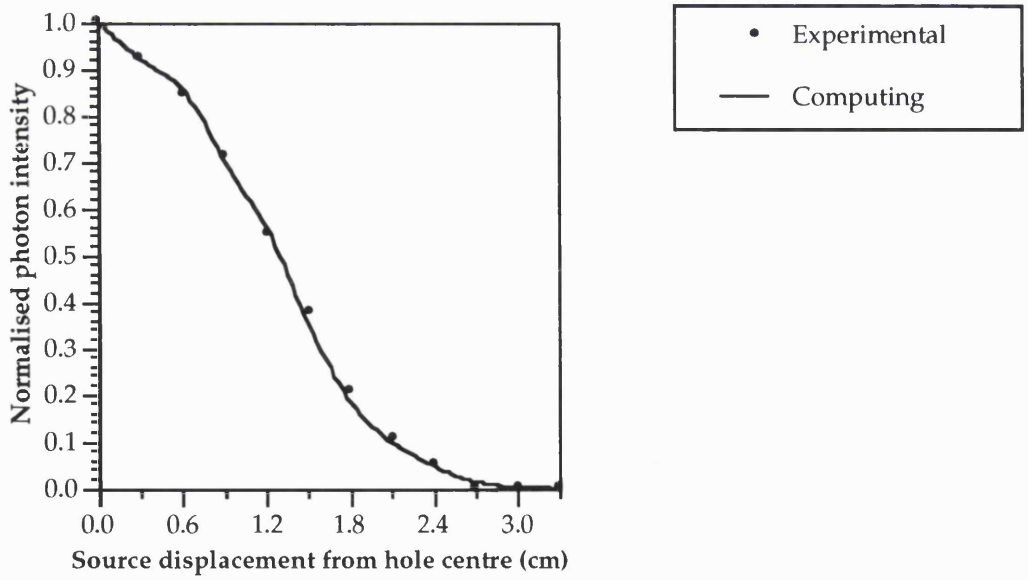

Figure 2.15 Experimental and simulated photon intensities as a function of source position for an americium source at a height of 0.4 cm. Collimator hole size 0.25 cm flat-to-flat, septal thickness of 0.03 cm and hole length 4.1 cm.

A comparison between the collimator responses obtained from experiment and simulation is shown in figures 2.14 and 2.15. Accurate angular positioning of the direction of motion of the source with respect to the diagonal of the collimator hole was difficult in the experiment, leading to a slight uncertainty in the direction of the experimental scan, a scan across the hole diagonal being assumed. The simulated scan was performed across the diagonal of the hole. Figure 2.14 gives the measured and computed photon intensity as a function of source position for a Tc-99m source at a height of 10 cm above the collimator. The error analysis considers the error to be a Poisson distribution using the square root of the count intensity. Good agreement is seen for all source positions. Figure 2.15 shows the curves obtained for an Am-241 source at a source height of 0.4 cm. The comparison indicates that the Monte Carlo code provides a good simulation of the transport of photons through collimators.

2.3.1.9 Theoretical validation of collimator code

Equation 1.3 provides a theoretical value for the resolution at FWHM of the geometric component of the collimator point spread function. As shown in section 1.3.3.2, since the equation provides the resolution for a square hole collimator, some modification is required when hexagonal hole collimators are considered. Equation 1.4 suggested that when hexagonal hole collimators were used the effective diameter becomes 0.866 DF, where DF is the flat-to-flat distance across the collimator hole. To verify this, the geometric FWHM was plotted against source height (figure 2.16).

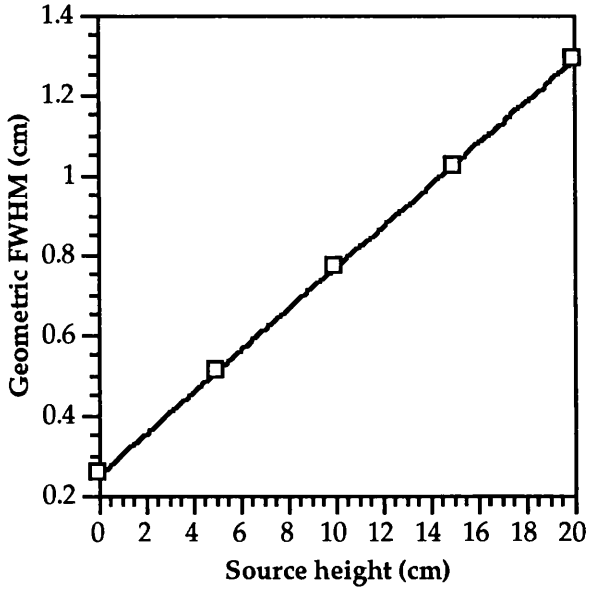

Figure 2.16 Variation in FWHM with source height.

From equation (1.3), a plot of the FWHM of the geometric PSF against the source height will yield a straight line of slope d/A and intercept $(d/A)\cdot(A+C)$ where d is the average effective diameter hole size, A is the collimator length and C is the distance

between the collimator and the detector plane. A weighted linear least square fit to the data produced the solid line through the points in figure 2.16 with the following values:

$$\text{SLOPE} = \frac{d}{A} = 0.052 \pm 0.002$$

$$\text{INTERCEPT} = \frac{d}{A}(A + C) = 0.251 \pm 0.001 \text{ cm}$$

For the collimator length (4.1 cm) and distance between collimator and detector plane (0.8 cm) the fit produces an effective hole diameter of $d = 0.212 \pm 0.012$ cm. Thus $d = m \cdot DF$ where $m = 0.848 \pm 0.048$ which is in agreement with the rough calculation which yielded $m = \sqrt{3}/2$

Equation 1.3 contains three variables which affect the spatial geometric resolution — the source height, the hole size and the collimator length. To verify the collimator code these three dimensions were varied.

Varying source height: Figure 2.16 confirms that the variation in FWHM with height obtained from the collimator code is as predicted by equation 1.3, a linear relationship being obtained. The values obtained for the gradient and intercept agree with those predicted by Anger's resolution equation.

Varying hole sizes: Consideration of equation (1.3) suggests that a plot of the FWHM of the geometric component of the PSF against the effective hole size should yield a straight line through the origin with a gradient of $(A+Z)/A$. Using the predicted value of $d = \sqrt{3}/2$ (equation (1.4)) for the effective hole size a plot of the FWHM against the hole size flat-to-flat will have a gradient of $\left(\sqrt{3}/2\right) \cdot \left((A+Z)/A\right)$. Figure 2.17 shows such a plot for two different hole sizes of the geometric and total components together with the curve predicted for the equation. Good agreement is seen between the computed and predicted geometrical components. Although a smaller hole size gives an improved resolution at FWHM the efficiency is degraded, which in turn degrades the image.

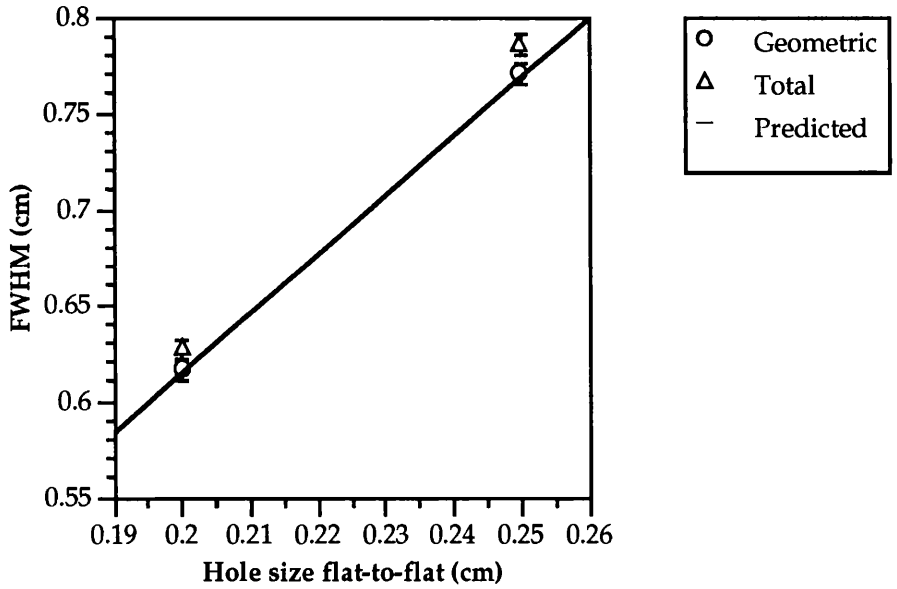

Figure 2.17 Variation in FWHM with hole size

Varying hole length: The collimator hole length is adjusted by altering the value in the input file. From Anger's resolution equation (1.6) a plot of the geometric FWHM against inverse hole length should yield a straight line with a gradient of the product of the hole diameter and source height, and an intercept of the effective hole diameter. Figure 2.18 is a plot of the FWHM of both geometric and total components against inverse hole length together with the line predicted from Anger's equation. The results of the geometric component from the simulation agree well with the predicted results.

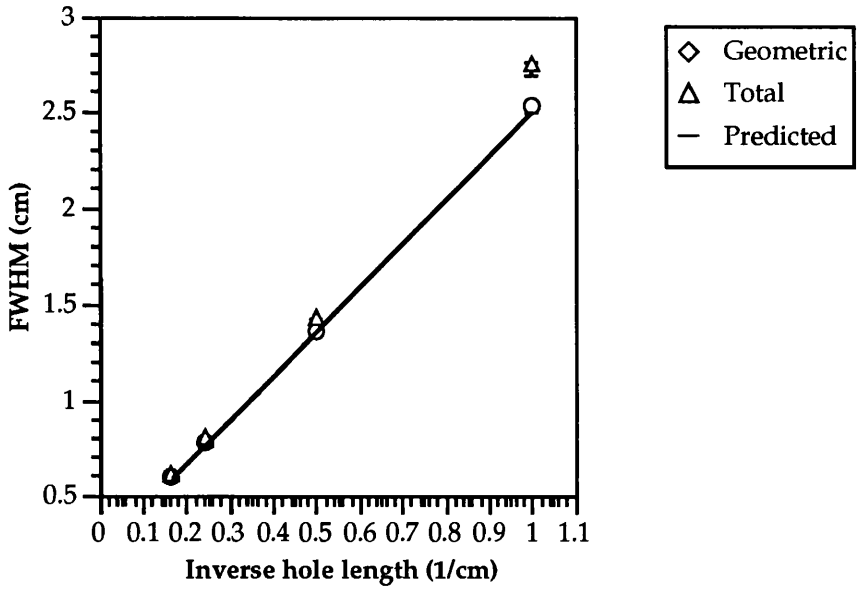

Figure 2.18 Variation in FWHM with hole length.

2.3.2 The source distribution

As discussed in section 2.1.2.1 the ideal situation of all photons emitted in the patient travelling to the collimator without being scattered does not exist. Interactions occur in the surrounding soft tissues and bones resulting in both scattered and unscattered photons entering the collimator. Thus a full description of the source distribution must include these scattered photons in addition to the primary photons. The source distribution can be obtained by numerical modelling or by experimental measurement. The accurate measurement of a source distribution would be very involved, requiring the determination of the spatial, angular and energy distrubutions of photons. Such a measurement would be time consuming and would present a hazard due to exposure to radioactivity. Data corrections would need applying to account for source decay. The simulation of a source distribution using Monte Carlo techniques removes the hazard of the experiment, and enables the accurate determination of spatial, angular and energy distributions.

2.3.2.1 Requirements of a source distribution model

Any radioactive source distribution can be considered as many point sources randomly located within that distribution. Photons are emitted isotropically from each of these point sources. Photons which pass through, and exit, the patient without undergoing an interaction are useful photons which will not degrade the image. In a gamma camera imaging system photons that undergo an interaction in the patient and are subsequently detected cannot provide useful information but serve only to degrade the image. In order to form an image using a computer simulation, a numerical model of the source distribution is required. Since the collimator is designed to limit the direction of photons contributing to the image, a knowledge of the angular distribution of the photons hitting the collimator is necessary in addition to the photon energies.

2.3.2.2 Description of a preliminary model

If the ideal situation of no scattering were true then the modelling of the photon distribution at the collimator would be simple. From a knowledge of the geometry, location and activity of the object the photon flux and distribution at the collimator surface could be determined by considering the active volume to consist of a uniform distribution of point sources. A numerical model of such a situation would consist of the spatial coordinates of the point sources of activity. In practice, however, scatter occurs so that the photon distribution at the collimator face consists of both primary and scattered radiation.

The energy distribution and angular distribution at the collimator surface of photons scattered in the object is dependent on both the source distribution and the volume, shape and location of any scattering material present. Any numerical model of scatter must be a model of the photon distribution on a plane located between the patient and the collimator. Both the angular and energy distributions of this model will vary across the plane. The result of a numerical model of scatter will therefore be a matrix containing the angular and energy distributions in each pixel of the plane of measurement. This distribution of photons on a plane outside the object can be obtained by Monte Carlo simulation.

The method that will be used to simulate any phantom may be generalised. Photon histories are traced from randomly generated source positions within a defined source volume to the surface of the phantom. At emission the direction of the photon is assigned by sampling an isotropic angular distribution. Coherent scatter, Compton scatter and photoelectric absorption are simulated. For each photon reaching the surface of the phantom the following parameters of the photon are recorded: coordinates (x, y, z), energy (E), polar and azimuthal angles (θ,ϕ) and a scatter index (n), denoting the types of scatter undergone (n=0 for no scatter, n=1 for a single Compton, n=2 for a single coherent, n=3 for multiple Compton, n=4 for multiple coherent and n=5 for mixed scatter).

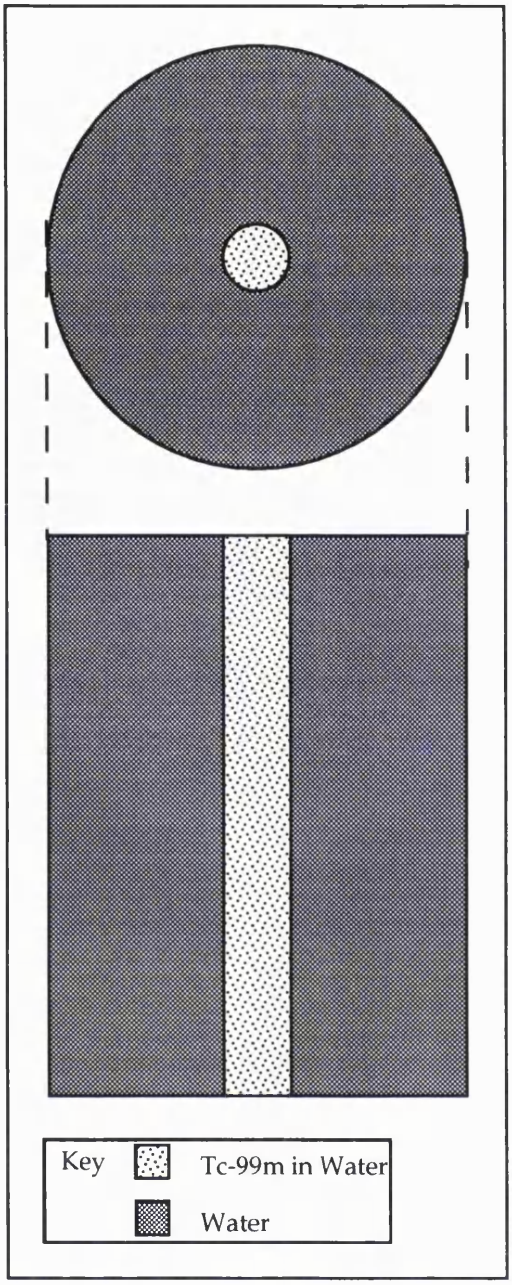

Figure 2.19 Prelimary phantom model.

Initially a simple geometry was selected so that the code could be easily verified experimentally. Figure 2.19 shows the phantom simulated. Photons were generated with random coordinates within the central cylinder and isotropic distributions were sampled. The initial photon energy was set at 140 keV. The number of photon histories traced was 10^9. Photons were traced until they were either photoelectrically absorbed, or they reached the external boundary of the outer cylinder. The coordinates, direction, energy and scatter index were recorded for photons reaching the external boundary.

To determine the photon distribution at a plane external to the phantom, the symmetry of the phantom was utilised. in order to increase the efficiency. Since the photon distribution on any plane tangential to a virtual cylinder surrounding the phantom

should be statistically identical, to determine the photon distribution on a plane a given distance from the phantom, To utilise this, the phantom was considered to be surrounded by 64 equidistant planes. A test is made on each photon to determine whether it will intersect any of the planes. Thus each photon can be 'detected' more than once depending on the number of planes with which it will interact. Since the distributions on the 64 planes should be identical, the distributions can be superimposed resulting in an increased efficiency. The planes modelled are situated 18 cm from the phantom centre. All photons incident on the central pixel (0.5 cm x 0.5 cm) of a plane are stored according to their angle of incidence on the plane.

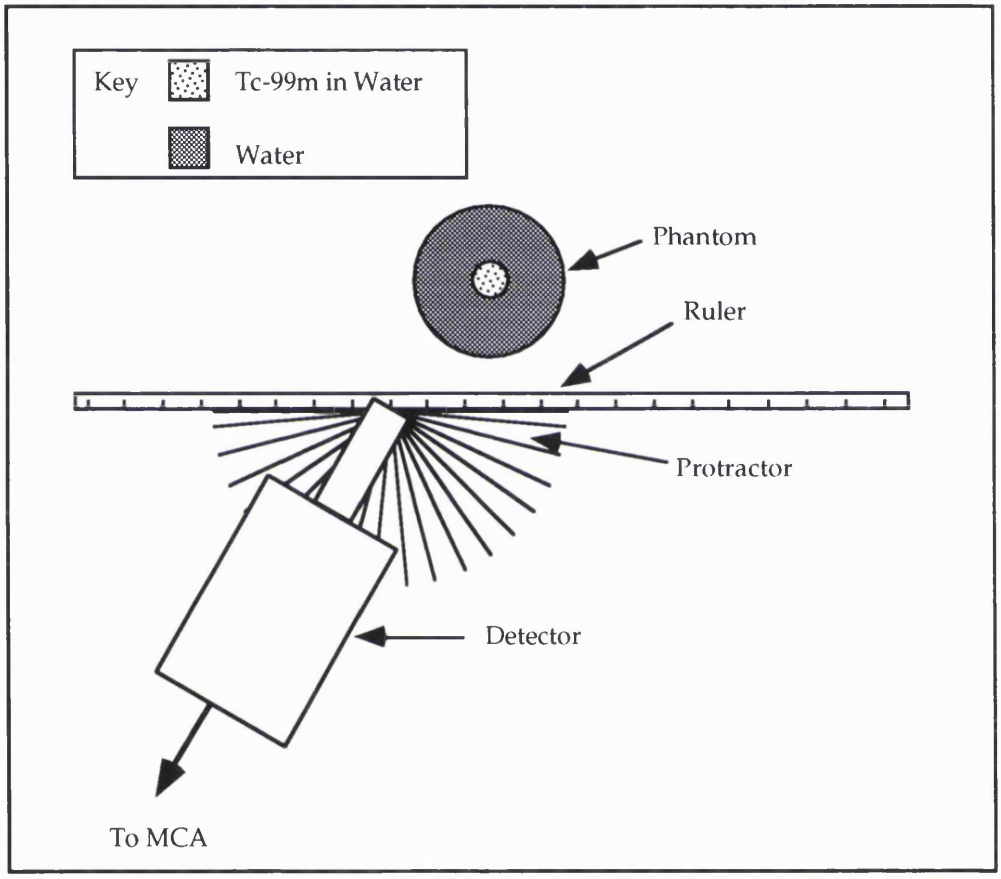

Figure 2.20 Experimental validation of source distribution at collimator plane.

2.3.2.3 Experimental validation of preliminary source distribution model

In order to test the EGS4 code a simple experiment was set up (figure 2.20). A 1.25 cm radius cylinder, of height 4 cm filled with technetium and water was placed at the centre of a cylindrical water phantom (8 cm radius, 10 cm height). Photon detection was performed using a high purity germanium detector (EG&G Ortec model no. GLP 36385/10P). The detector was placed at several positions along a plane situated 18 cm from the centre of the phantom. For each detector position spectra were recorded at various angles to the detection plane. A single hole lead collimator, with hole radius 0.25

cm and length 4.9 cm was attached to the front of the detector in order to limit the angle of incidence of the photons. Errors involved in the experimental measurement were the positioning of the detector, both in distance from the phantom and distance from the central axis. The error on each of these was estimated to be ± 0.25 cm maximum. The angular positioning of the detector also led to an estimated error of less than ± 1 degree. The use of the collimator gave maximum positioning uncertainties of ± 0.25 cm and angular uncertainties of ± 3 degrees.

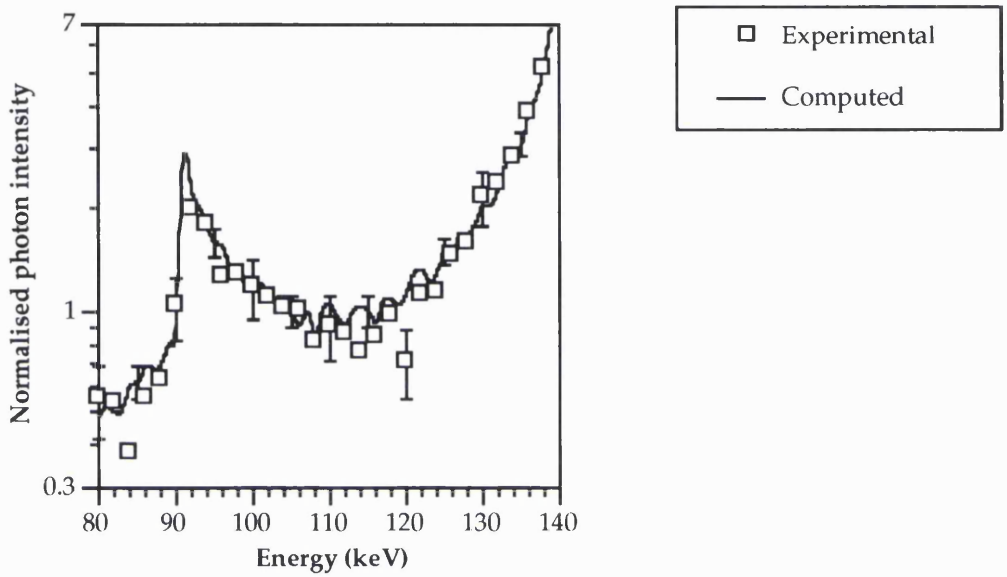

Figure 2.21 Energy spectrum at incident angle of 0°.

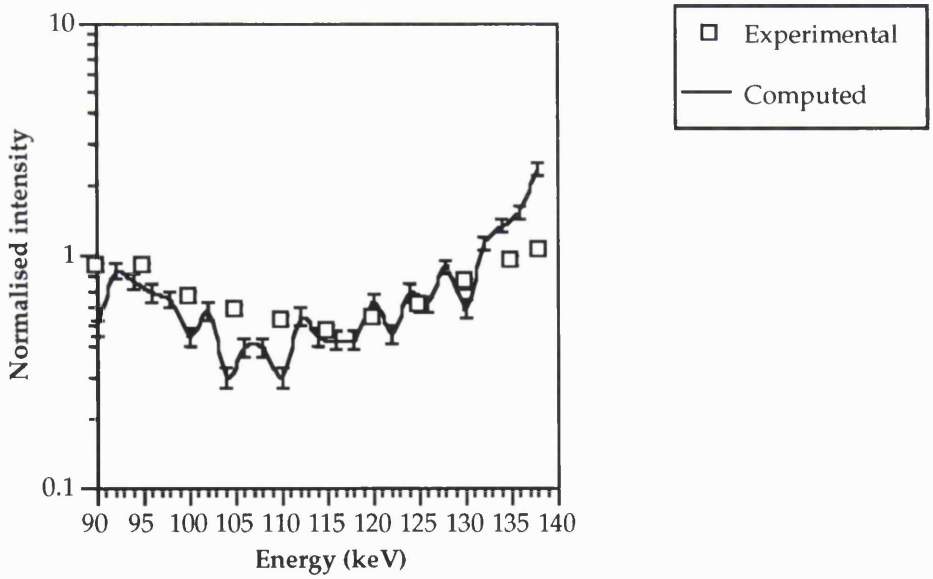

Figure 2.22 Energy spectrum at incident angle of 5°.

Figures 2.21 and 2.22 show the spectra obtained from the experiment and the simulation for two different angles. An accurate comparison is difficult due to the uncertainties involved in the experimental technique, however strong similarities are seen between the results. Figure 2.21 shows the results obtained at a normal incident photon angle. Two main peaks exist at 140 keV and 91 keV. These peaks are expected and are due to the source energy and the backscattered photon energy. No obvious peaks exist between these values in either technique. The results obtained for an incident photon angle of 5° are shown in figure 2.22. Once again both set of results produce a dominant peak at 140 keV with a much less significant back scatter peak. Both curves show the Compton continuum rising to 140 keV.

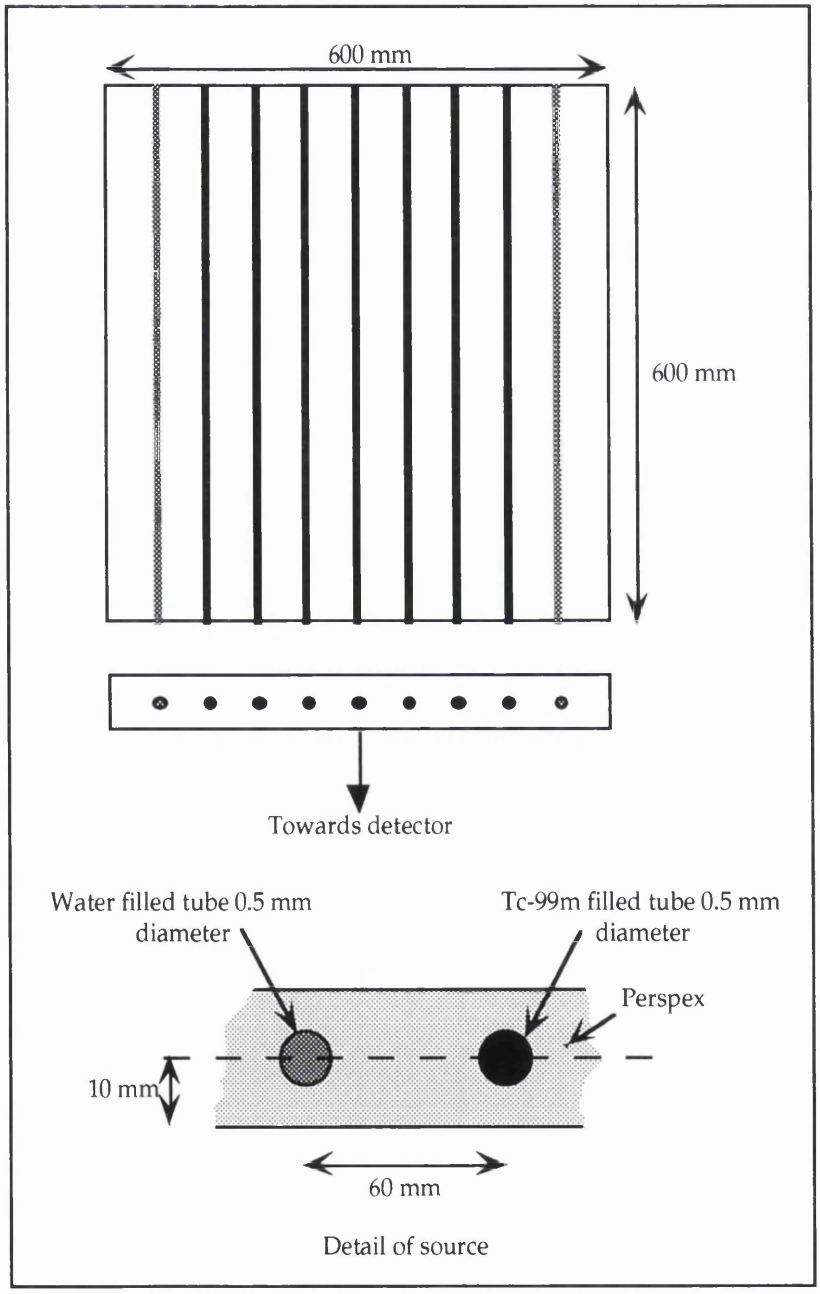

Figure 2.23 Phantom simulated for system resolution and distortion measurements.

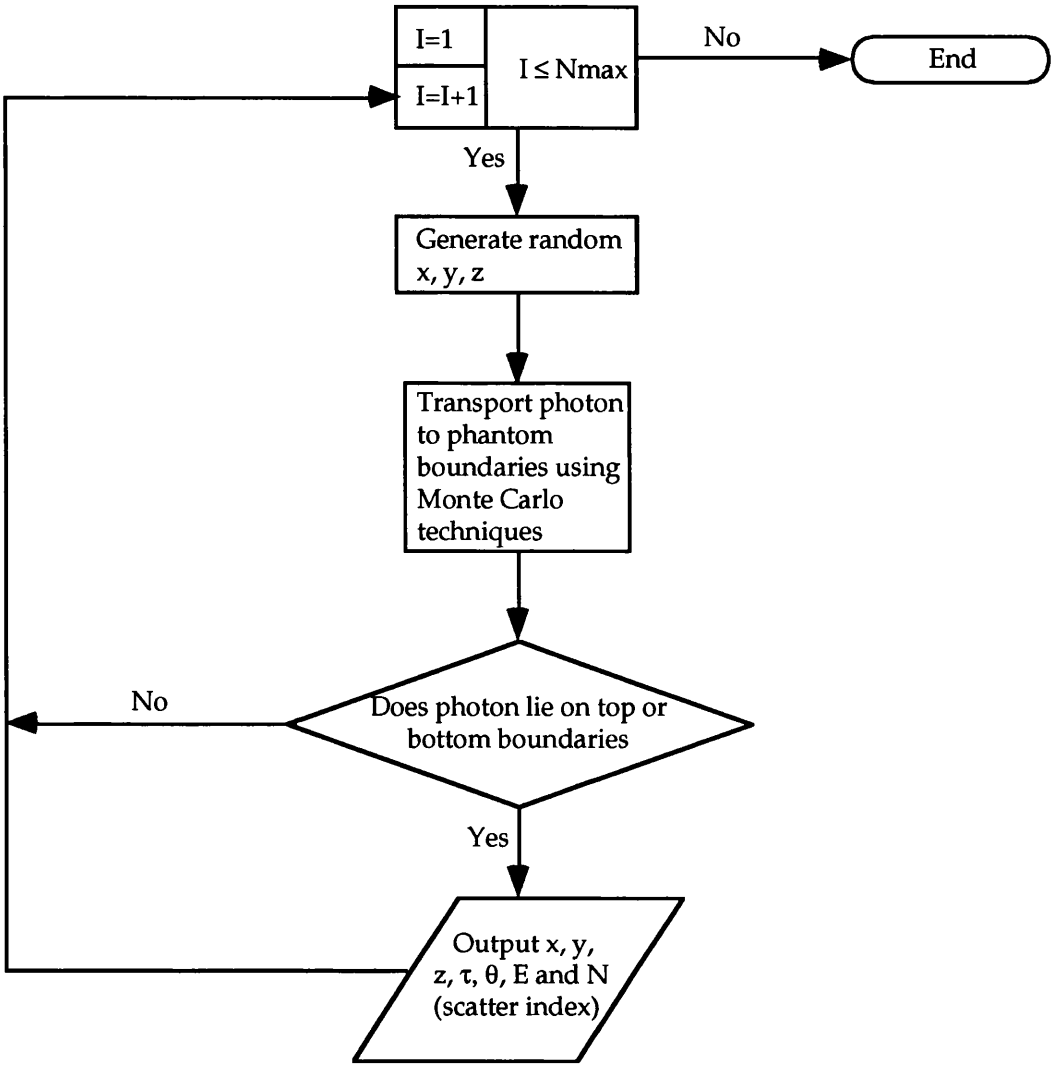

Figure 2.24 Monte Carlo simulation of photon transport in line source phantom.

2.3.2.4 Line source phantom Monte Carlo simulation

Having validated the EGS4 computer code model of a simple phantom experimentally it is necessary to extend it to simulate a more complicated phantom. Elliott *et al* (1986) describe a line source phantom which is used for gamma camera assessment. The line source phantom consisted of 19 parallel line sources comprising 0.5 mm bore glass capillary tubing positions in slots in a perspex base at 30 mm separation. The perspex base had overall dimensions 600 mm x 600 mm x 20 mm. Alternate lines were filled with technetium-99m to avoid overlap of adjacent line spread functions. To provide both forward and backward scattering, a further 18 sheets of perspex each of dimensions 600 mm x 600 mm x 10 mm were used producing an overall phantom thickness of 200 mm. The line source layer could be positioned at several different distances from the collimator. This phantom was used as the basis for a numerical simulation of a line source phantom. The phantom simulated is depicted in figure 2.23.

For the Monte Carlo simulation, the external dimensions of the phantom are kept the same as the phantom of Elliott *et al* (1986), but some other modifications have been made. Nine cylinders of 0.5 mm diameter are located with 60 mm separations. For attenuation and scatter purposes all cylinders are considered to be water filled. Photons of 140 keV energy are generated from a uniform distribution of spatial coordinates within the seven innermost cylinders. To reduce the CPU time the two outer cylinders do not contain activity.

Monte Carlo techniques are used to trace photons from their generation in the cylinders until they either reach the external boundaries of the phantom or are terminated, whichever occurs first. Parameters of the photons reaching the top and bottom of the phantom are written to file, while all other photons are discarded since they cannot be detected. The photon parameters stored are x, y, z coordinates, energy, polar and azimuthal angles of direction and index of scatter. A flow chart of the code is given in figure 2.24.

An experimental validation of the line source phantom model was not possible as the actual phantom was unavailable. However, since the code was simply an extension of the simple phantom it was assumed that the Monte Carlo techniques used were correct. The initial coordinates of photons within the phantom were tested to confirm that they were uniformly distributed within the line sources, and the isotropic distribution of photons was also confirmed.

2.3.3 Experimental measurement of the response of the uncollimated camera

Chapter one has discussed the fact that the camera (crystal, PM tubes and associated electronics) degrade both the spatial and energy resolutions of the gamma camera system. The intrinsic response of the camera is determined using a phantom similar to that shown in figure 2.25.

The phantom is placed centrally on the gamma camera face with the collimator removed. The area of the field of view outside the edge of the phantom is masked with lead. An uncollimated source is placed at a distance of 2 m above the centre of the camera. The phantom is positioned with the central slit along the electronic axis of the detector. Response profiles are obtained for the line sources. The camera resolution is determined by measuring the FWHM and FWTM of the line sources.

2.3.4 Image production using response functions

The method of image formation was discussed in section 2.2.1. The possibility of using convolution techniques for the formation of the image was limited to the convolution of the image formed by the collimator with the intrinsic camera response. It was decided that it would not be possible to convolve the collimator response function

with the source distribution because of the shift-variance caused by scatter in the object. The following method is therefore suggested for image formation.

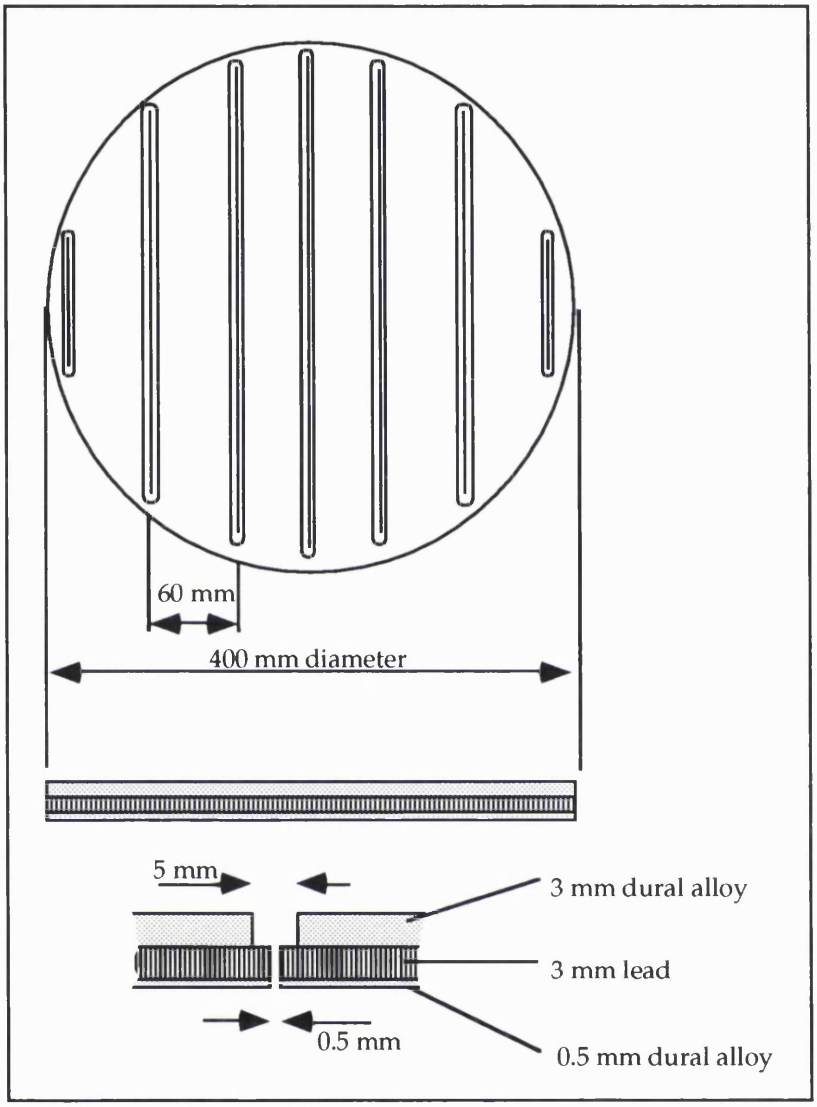

Figure 2.25 Phantom for measurement of intrinsic resolution showing detail of slit.

The first stage in the process is to determine the photon distribution on the entrance face of the collimator. To achieve this the program depicted by the flow chart in figure 2.26 is used. To utilise the symmetry of the line source phantom, photons which lie on both the upper and lower planes are used for image formation. This is done by considering two collimator planes at equal distances from the upper and lower phantom planes. When the line sources are centred in the depth of scatter, photons on the upper and lower planes contribute to the same image, however when the line sources are not at the centre different images are formed by the photon distribution on the upper and lower surfaces. Having read the photon parameters, a test is made to determine whether the photon lies on the upper plane. The photon's coordinates and directions are transformed

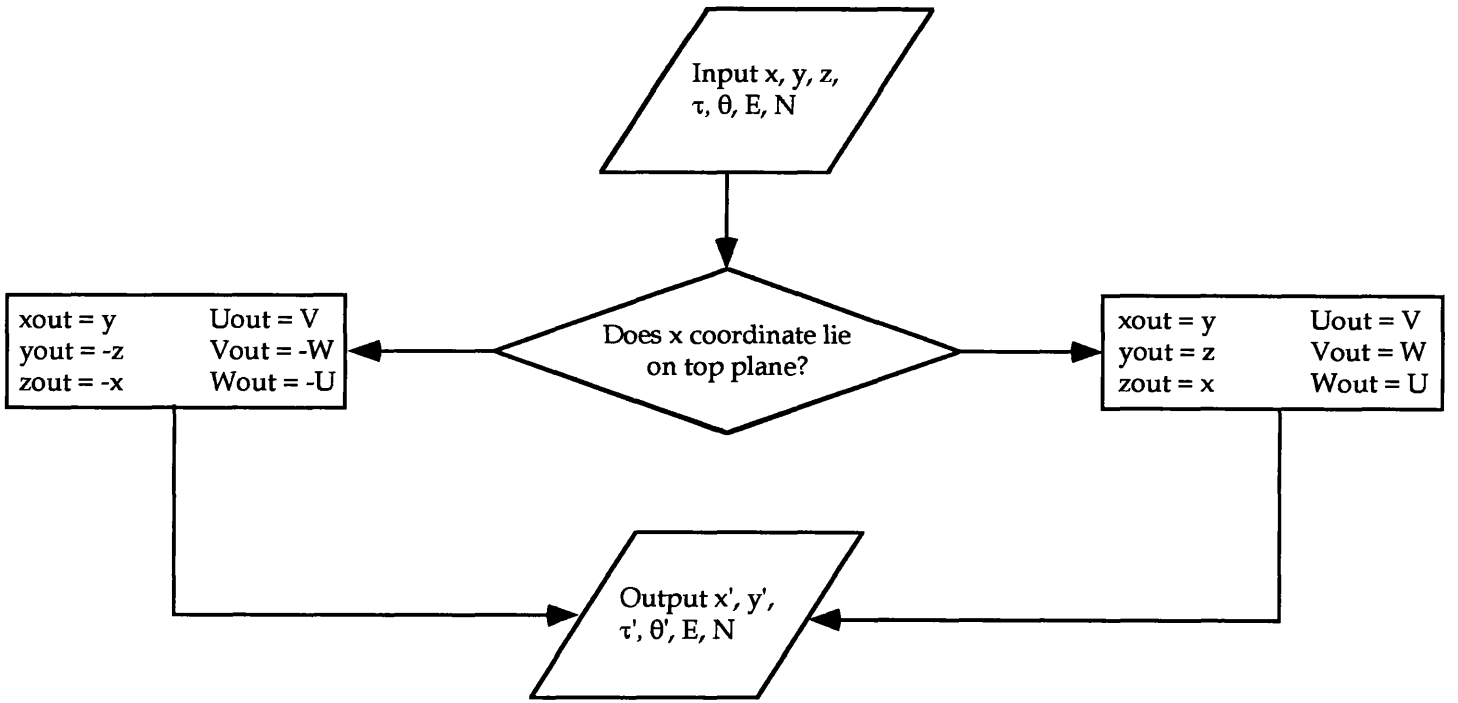

Figure 2.26 Tranformation of coordinates.

detected and is designated to be either geometric, penetrated or scattered in the collimator. This is achieved by randomly sampling a uniform distribution between 0 and N, the number of photons generated per azimuthal angle in the collimator response program. From the direction of the photon the required offset position of the response function is determined and the numbers of primary, penetrated, scattered and absorbed photons for that position are read from the response function. Finally the process is chosen according to the following tests:

If $0 \leq R < G$ then the photon will be geometric

else if $G \leq R < G + P$ then the photon will have penetrated the septa

else if $G + P \leq R < G + P + S$ then the photon will be scattered

else the photon will be absorbed

where R is the random number generated,

G = number of geometric photons in response at offset position,

P = number of penetrated photons in response at offset position,

S = number of scattered photons in response at offset position

and $0 \leq R < N$.

For each detected photon, the pixel location in the image is calculated. The photon data are written to one of 15 image files according to the interactions in the object (primary or scattered), the photon energy on entering the collimator ($125 \leq E < 130$, $130 \leq E < 135$, $135 \leq E < 140$, and $E = 140$ keV) and interactions in the collimator (geometric, penetrated or scattered).

Having formed the image in the crystal in this way a digital convolution of the intrinsic response with this image produces the system image.

2.3.5 Analysis of images

Standard methods exist for the quantitative assessment of gamma camera imaging. Such methods are described by Elliott *et al* (1986) in a programme of measurements for the Department of Health and Social Security (DHSS). These tests include measurements of the intrinsic and system resolutions and the spatial distortion and are carried out in the presence of a scattering medium to reflect clinical use and performance in accordance with the International Electrotechnical Commission (British Standards Institution) recommendations (1984). The tests were performed with technetium-99m using a window width of 20% centred on 141 keV. As an assessment of the numerical simulation methods described in this thesis and of the various collimators modelled it was decided to use two of the tests formulated in the DHSS report, namely a quantitative measurement of both system resolution and spatial distortion. The line source phantom described in section 2.3.2.4 forms the basis for a numerical simulation of these tests so that the collimators described in section 2.3.1 can be compared and assessed.

To determine the spatial resolution of the collimator and camera systems a program was written to compute the FWHM, FWTM and centroid of each line in each

profile of the line source phantom image. This was achieved by assuming the line spread functions to be Gaussian and using a linear least squares fitting routine. Although a Gaussian curve is a non-linear function, it can be transformed into a linear function by taking natural logs. Consider a Gaussian function

$$y = \frac{1}{\sqrt{2\pi\sigma_x^2}} \exp\left[\frac{-(x-\bar{x})^2}{2\sigma_x^2}\right] \tag{2.19}$$

where $\bar{x}$ is the centroid position

and $\sigma_x = \frac{FWHM}{2\sqrt{2\ln(2)}}$. (2.20)

By taking natural logs the following expression is obtained

$$\ln(y) = a_3x^2 + a_2x + a_1 \tag{2.21}$$

where $a_1 = \ln\left[\frac{1}{\sqrt{2\pi\sigma_x^2}} - \frac{\bar{x}^2}{2\sigma_x^2}\right]$, (2.22)

$$a_2 = \frac{\bar{x}}{\sigma_x^2} \tag{2.23}$$

and $a_3 = -\frac{1}{2\sigma_x^2}$. (2.24)

The parameters a_1, a_2 and a_3, and hence the FWHM, FWTM and centroid can therefore be obtained from a weighted least squares fit to the logarithmic values of the data using a polynomial of the second order. These parameters are obtained for each line within each profile of the image. The spatial distortion of the image was measured by averaging the calculated centroid positions of each profile of a particular line and determining the absolute magnitudes of the differences between the fitted and mean positions.

2.4 Application of these techniques

This chapter has dealt with the formation of images from gamma camera systems from the combination of source distributions with response functions of system components. The remaining chapters will use the techniques introduced in this chapter to determine response functions of various collimators and to form images using those collimators. The images produced will be analysed using the Gaussian fitting routine in order to determine the quality of the collimators used.

- 3 -

Collimator response functions

Chapter two has described the method in which images will be formed by numerical simulation in this thesis. This chapter will deal with the response functions of the various collimators obtained using the Monte Carlo collimator simulation.

3.1 Use of response functions for collimator assessment

While, ultimately, it is the investigation of an image which determines the suitability of a particular collimator for imaging, a detailed knowledge of the response function will provide indispensable information on the collimator and a good indication of its suitability for imaging. In the description of the collimator model in chapter two, the simulation was shown to provide information on photon histories in the collimator, enabling the geometric, penetrated and scattered components to be individually investigated. In this chapter the different types of collimators will be assessed in terms of the individual components of the response function to provide an indication of their imaging capabilities.

The same basic pattern of investigation will be followed for each collimator type. Firstly, for collimators of identical geometries, the geometric component of the response function should be identical; this will be verified. An ideal collimator should absorb all photons entering the septa, resulting in no penetrated or scattered photons being detected. Any deviation from this ideal situation will, as has been discussed previously, degrade the image. In practice no collimator will provide total photon absorption, and so for each collimator modelled both the penetration and scatter components will be investigated. Having investigated the individual components, the total collimator response function will then be presented and analysed. Each of these components and the total collimator response will be analysed in terms of the resolution and half maximum, tenth maximum and one hundredth maximum. Finally, the efficiencies of each collimator will be given.

3.2 Collimator parameters

A description of all the collimators modelled for this thesis is given in table 3.1. The various collimators are described in terms of their dimensions, hole angulations, number of layers (one for single material collimators) and materials (MAT 1, MAT 2). All modelled collimators had a flat-to-flat hole size of 0.25 cm and were 4.1 cm in length.

NAME	Septal thick-ness (mm)	Hole angul-ation (°)	No of layers			MAT 1	MAT 2	Layer thickness (cm)		% Mat 1 in height
			Tot	Mat 1	Mat 2			Mat 1	Mat 2	
C10	0.10	0.00	1	1	0	Pb	/	4.1	/	100
C15	0.15	0.00	1	1	0	Pb	/	4.1	/	100
C20	0.20	0.00	1	1	0	Pb	/	4.1	/	100
C24	0.24	0.00	1	1	0	Pb	/	4.1	/	100
C30	0.30	0.00	1	1	0	Pb	/	4.1	/	100
C35	0.35	0.00	1	1	0	Pb	/	4.1	/	100
C40	0.40	0.00	1	1	0	Pb	/	4.1	/	100

Table 3.1 (a) Parameters of conventional collimators.

NAME	Septal thick-ness (mm)	Hole angul-ation (°)	No of layers			MAT 1	MAT 2	Layer thickness (cm)		% Mat 1 in height
			Tot	Mat 1	Mat 2			Mat 1	Mat 2	
AS000	0.24	0.00	1	1	0	Pb	/	4.1	/	100
AS005	0.24	0.05	1	1	0	Pb	/	4.1	/	100
AS010	0.24	0.10	1	1	0	Pb	/	4.1	/	100
AS015	0.24	0.15	1	1	0	Pb	/	4.1	/	100
AS020	0.24	0.20	1	1	0	Pb	/	4.1	/	100
AS025	0.24	0.25	1	1	0	Pb	/	4.1	/	100
AS030	0.24	0.30	1	1	0	Pb	/	4.1	/	100
AS035	0.24	0.35	1	1	0	Pb	/	4.1	/	100
AS040	0.24	0.40	1	1	0	Pb	/	4.1	/	100
AS045	0.24	0.45	1	1	0	Pb	/	4.1	/	100
AS050	0.24	0.50	1	1	0	Pb	/	4.1	/	100
AS055	0.24	0.55	1	1	0	Pb	/	4.1	/	100
AS060	0.24	0.60	1	1	0	Pb	/	4.1	/	100
AS065	0.24	0.65	1	1	0	Pb	/	4.1	/	100
AS070	0.24	0.70	1	1	0	Pb	/	4.1	/	100
AS075	0.24	0.75	1	1	0	Pb	/	4.1	/	100
AS080	0.24	0.80	1	1	0	Pb	/	4.1	/	100
AS085	0.24	0.85	1	1	0	Pb	/	4.1	/	100
AS090	0.24	0.90	1	1	0	Pb	/	4.1	/	100
AS095	0.24	0.95	1	1	0	Pb	/	4.1	/	100
AS100	0.24	1.00	1	1	0	Pb	/	4.1	/	100

Table 3.1 (b) Parameters of slanted collimators.

NAME	Septal thickness (mm)	Hole angulation (°)	No of layers			MAT 1	MAT 2	Layer thickness (cm)		% Mat 1 in height
			Tot	Mat 1	Mat 2			Mat 1	Mat 2	
M0100	0.24	0.00	409	205[1]	204	Pb	Al	0.0100	0.0100	50.24
M0100	0.24	0.00	41	21	20	Pb	Al	0.1000	0.1000	51.22
M1640	0.24	0.00	25	13	12	Pb	Al	0.1640	0.1640	52.00
M2158	0.24	0.00	19	10[2]	9	Pb	Al	0.2158	0.2158	52.63
M3727	0.24	0.00	11	6[3]	5	Pb	Al	0.3727	0.3727	54.55
M8200	0.24	0.00	5	3	2	Pb	Al	0.8200	0.8200	60.00

Table 3.1 (c) Parameters of laminated collimators.

[1] Bottom layer is double thickness of lead.

[2] Bottom layer is 0.2156 cm lead.

[3] Bottom layer is 0.3730 cm lead.

NAME	Septal thickness (mm)	Hole angulation (°)	No of layers			MAT 1	MAT 2	Layer thickness (cm)		% Mat 1 in height
			Tot	Mat 1	Mat 2			Mat 1	Mat 2	
S49	0.24	0.00	3	2	1	Pb	Al	1.0	2.1	49
S73	0.24	0.00	3	2	1	Pb	Al	1.5	1.1	73
S88	0.24	0.00	3	2	1	Pb	Al	1.8	0.5	88
S98	0.24	0.00	3	2	1	Pb	Al	2.0	0.1	98

Table 3.1 (d) Parameters of sandwich collimators.

NAME	Septal thickness (mm)	Hole angulation (°)	No of layers			MAT 1	MAT 2	Layer thickness (cm)		% Mat 1 in height
			Tot	Mat 1	Mat 2			Mat 1	Mat 2	
W24	0.24	0.00	1	1	0	W	/	4.1	/	100
U24	0.24	0.00	1	1	0	U	/	4.1	/	100
U20	0.20	0.00	1	1	0	U	/	4.1	/	100
U15	0.15	0.00	1	1	0	U	/	4.1	/	100
U10	0.10	0.00	1	1	0	U	/	4.1	/	100
U05	0.05	0.00	2	1	0	U	/	4.1	/	100

Table 3.1 (e) Parameters of alternative material collimators.

The basic types of collimators modelled were: conventional (table 3.1 a), angulated (table 3.1 b), laminated (table 3.1 c), sandwich (table 3.1 d) and alternate materials (table 3.1 e). The response functions of each type will be discussed in the following sections.

3.3 Response functions of collimators

3.3.1 Conventional lead collimator response functions

The majority of gamma camera collimators are constructed from lead or a lead alloy, and have hexagonal holes in a close packed hexagonal array. Several conventional lead collimators [C10, C15, C20, C24, C30, C35, C40; table 3.1(a)] were modelled and their resolutions for a point source height of 0 cm are presented in table 3.2.

NAME	FWHM (cm)			FWTM (cm)			$FW\frac{1}{100}M$ (cm)		
	G	G+P	G+P+S	G	G+P	G+P+S	G	G+P	G+P+S
C10	0.252	0.257	0.257	0.508	0.521	0.521	0.608	1.158	1.169
C15	0.254	0.259	0.259	0.509	0.522	0.523	0.607	1.148	1.189
C20	0.253	0.258	0.258	0.508	0.517	0.517	0.609	0.632	0.632
C24	0.253	0.258	0.258	0.507	0.518	0.518	0.602	0.630	0.630
C30	0.254	0.258	0.258	0.508	0.517	0.517	0.606	0.631	0.632
C35	0.253	0.257	0.257	0.507	0.517	0.517	0.608	0.632	0.632
C40	0.252	0.257	0.257	0.507	0.517	0.517	0.607	0.631	0.631

Table 3.2 Resolutions of conventional lead collimators. Error on resolutions is ± 0.001 cm. G, P and S represent the geometric, penetrated and scattered components of the response functions, respectively.

3.3.1.1 Geometric resolution

It is useful to be able to compare the geometric resolutions of each of the collimators modelled as a test of the geometry routines in the Monte Carlo code. The geometric resolutions at half maximum given in table 3.2 give approximately the same value (0.253 ± 0.001 cm) for each of the septal thicknesses considered. The same is true at one tenth and one hundredth of the maximum where the resolutions are 0.508 ± 0.001 cm and 0.607 ± 0.002 respectively. The shape of the average geometric collimator response is triangular (figure 3.1)

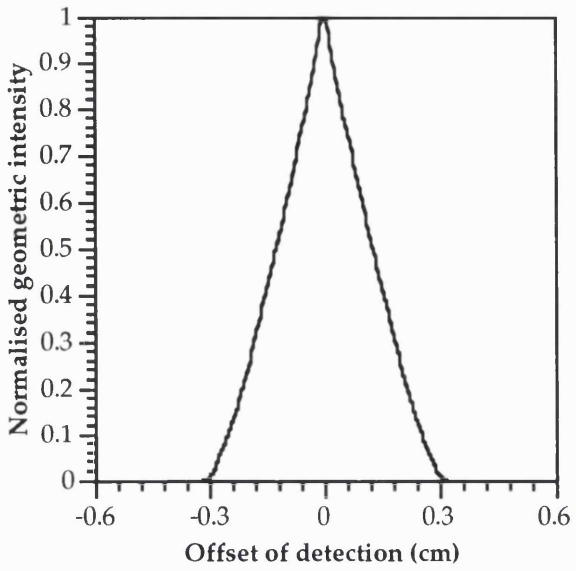

Figure 3.1 Shape of geometric component of response function.

3.3.1.2 Geometric and penetrated resolution

Figure 3.2 shows the shape of the penetration component of collimator C24. The graph shows the small amount of penetration contributing to the centre of the response function. This is due to the large thickness of lead that would need to be traversed (4.1 cm) by penetrating photons at this position.

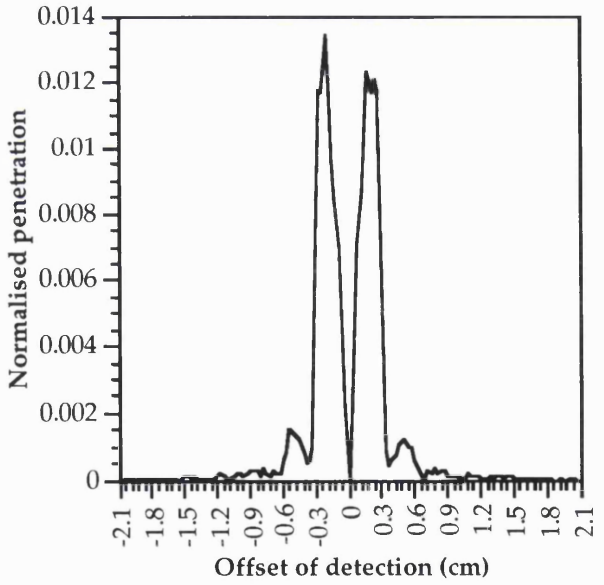

Figure 3.2 Typical shape of penetration component of response function.

Moving outwards from the centre, initially the proportion of penetrated photons detected increases. This increase corresponds to those photons penetrating the edges of septa. As the photon angle increases further, the proportion of penetrated photons

decreases again, due to edge penetration decreasing and photons undergoing full septal penetration contributing. The response rises and falls according to the typical thickness of lead that would need to be traversed by photons at particular angles. Eventually the response falls to zero, when many septa would have to be penetrated for a photon to be detected.

Figure 3.3 is a logarithmic plot of the penetration components of collimators C10, C24 and C35. The total amount of penetration can be seen to decrease with increase in septal septal thickness. Collimator C10 has excessive penetration.

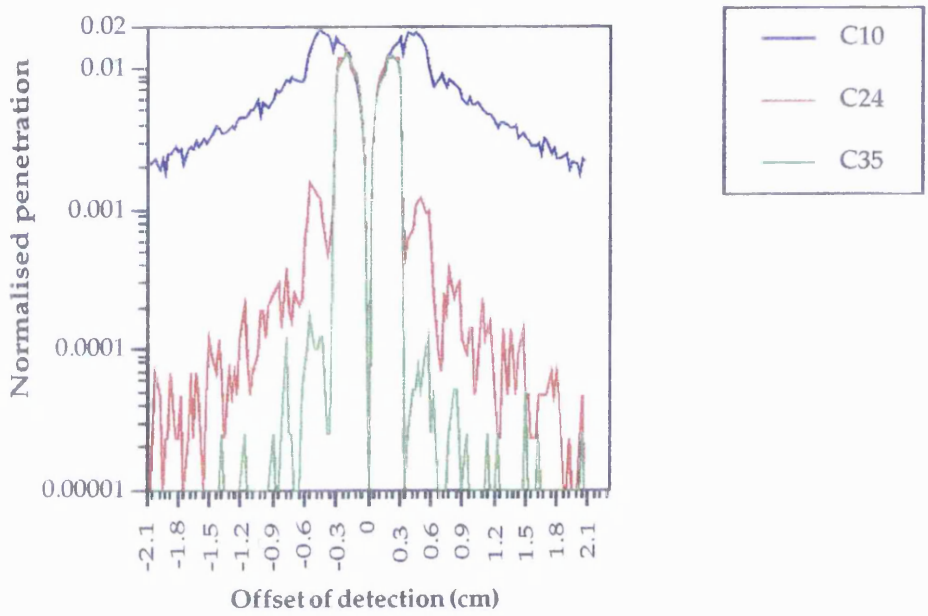

Figure 3.3 Penetration component variation with septal thickness.

Analysis of the values of resolution (table 3.2) for geometric and penetrated photons indicate that penetrated photons do not greatly affect the FWHM values for any of the septal thicknesses modelled. When the FWTM is considered, the width of the geometric and penetrated resolution increases slightly for the collimators C10 and C15, however collimators C20 to C40 produce a similar value of FWTM. While for septal thicknesses between 0.020 cm and 0.040 cm the increase in width at tenth maximum when penetration is included is on average 2.0%, for septal thicknesses of 0.010 cm and 0.015 cm the increase in width is approximately 2.6%. The increase in resolution for the narrower septal thicknesses occurs to a greater extent at the FW$\frac{1}{100}$M where the average increase in width for inclusion of penetration is 89.8% compared with only 4.1% for the larger septal thicknesses. Thus, unless a higher efficiency is required, the use of the two narrowest septal thicknesses would result in an undesirable loss in resolution. Any of the larger septal thicknesses will produce a similar resolution, however, the efficiency will suffer as the septal thickness increases. Table 3.3 gives the predicted geometric efficiencies for each of the conventional lead collimators modelled.

Collimator	Efficiency (%)
C10	0.0241
C15	0.0232
C20	0.0224
C24	0.0217
C30	0.0208
C35	0.0201
C40	0.0194

Table 3.3 Efficiencies of conventional lead collimators.

To minimise penetration it is therefore necessary to use a septal thickness of 0.020 cm or thicker. However increasing the septal thickness above about 0.020 cm or 0.024 cm does not result in the detection of fewer penetrated photons. The reason for this is that for all septal thicknesses, the probability of edge penetration is equal, while full septa penetration will virtually be prohibited by a certain thickness of lead (figure 3.4).

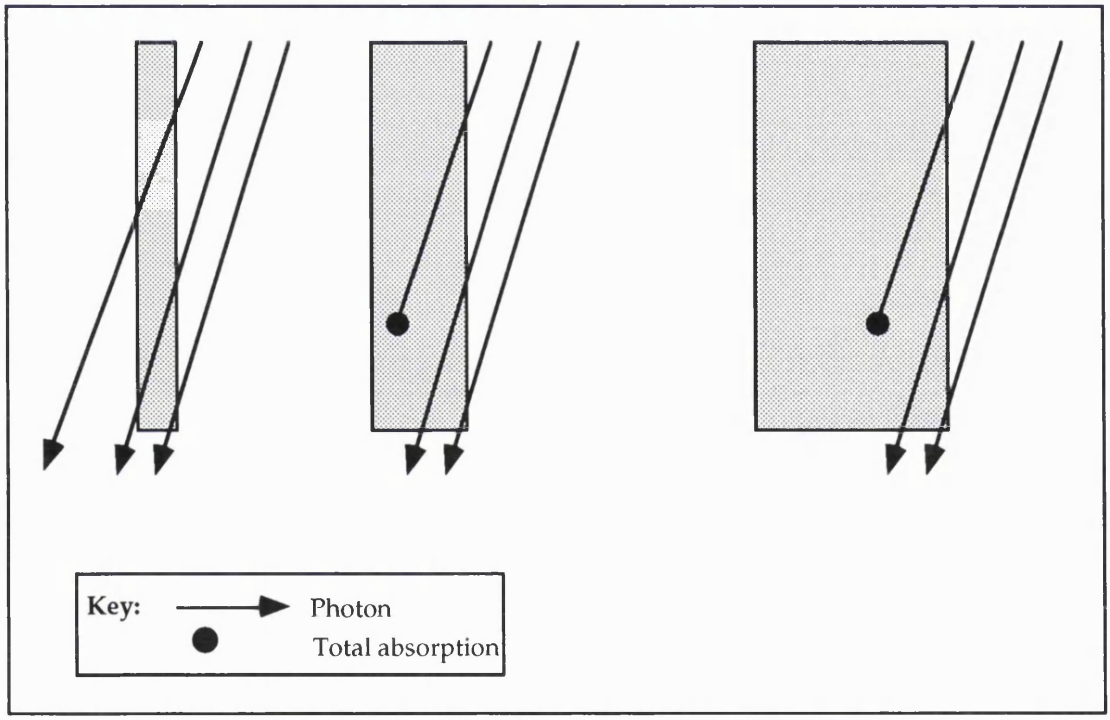

Figure 3.4 Effect of septal thickness on penetration. The quantity of edge penetration is unaffected by the thickness of the septum, however the quantity of photons detected which have penetrated a full septum decreases with increase in septal thickness.

For the thicknesses modelled the results indicate little advantage in having septal thicknesses greater than about 0.020 cm, while an unacceptable degree of septal penetration occurs for the two narrowest septal thicknesses modelled. For the best efficiency and spatial resolution therefore, a septal thickness of 0.020 cm or 0.024 cm

should be chosen. The slightly thicker septa of 0.024 cm will be easier to cast accurately than 0.020 cm.

3.3.1.3 Geometric, penetrated and scattered resolution

Analysis of table 3.2 shows that scatter is not a significant problem, it only affects the tails of the response functions by increasing the FW$\frac{1}{100}$M for C10 and C15. The effects due to penetration which were described previously are much more significant.

The total response functions for three of the collimators, C10, C24 and C35 are shown in the logarithmic plot of figure 3.5. The tails of collimator C10 have an intensity of approximately 0.5% of the peak. This is mainly due to penetration. The response functions of both C24 and C35 are acceptable, the intensity in the tails being about 0.05% of the peak. However, the efficiency of C24 makes it more suitable than C35.

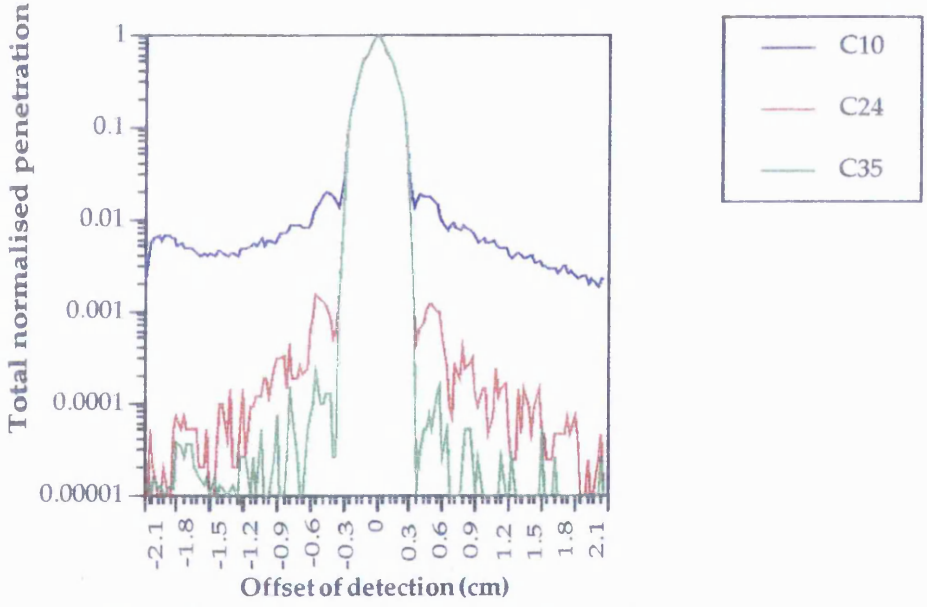

Figure 3.5 Total response function variation with septal thickness.

3.3.2 Angulated lead collimator response functions

Chapter two has discussed the fact that collimator holes are often not precisely orthogonal to the collimator surface, resulting in non-uniformity and spatial distortion. This section examines the response functions of a series of collimators each of which has a particular hole angulation. The results obtained in this section will be used in chapter four to assess collimators with random angulations throughout. All the results presented for angulated collimators are for collimators with a 0.25 cm flat-to-flat hole size and 4.1 cm hole length. The collimator resolutions are given in table 3.4 for a source height of 0 cm.

NAME	FWHM (cm)			FWTM (cm)			$FW\frac{1}{100}M$ (cm)		
	G	G+P	G+P+S	G	G+P	G+P+S	G	G+P	G+P+S
AS000	0.253	0.258	0.258	0.507	0.518	0.518	0.602	0.630	0.630
AS005	0.258	0.263	0.264	0.510	0.519	0.520	0.609	0.630	0.631
AS010	0.264	0.269	0.269	0.510	0.520	0.520	0.614	0.630	0.631
AS015	0.268	0.273	0.273	0.512	0.522	0.522	0.616	0.627	0.628
AS020	0.270	0.275	0.275	0.512	0.523	0.523	0.616	0.624	0.625
AS025	0.275	0.280	0.281	0.512	0.524	0.524	0.618	0.626	0.626
AS030	0.274	0.280	0.280	0.512	0.523	0.524	0.618	0.626	0.627
AS035	0.277	0.283	0.283	0.513	0.524	0.525	0.619	0.627	0.627
AS040	0.278	0.283	0.283	0.520	0.523	0.523	0.618	0.636	0.636
AS045	0.281	0.286	0.287	0.515	0.526	0.526	0.622	0.639	0.639
AS050	0.284	0.290	0.295	0.517	0.527	0.527	0.627	0.640	0.640
AS055	0.287	0.293	0.293	0.517	0.526	0.527	0.631	0.642	0.642
AS060	0.289	0.295	0.295	0.518	0.528	0.528	0.632	0.643	0.643
AS065	0.291	0.298	0.298	0.518	0.526	0.527	0.632	0.643	0.644
AS070	0.293	0.299	0.299	0.517	0.528	0.529	0.630	0.643	0.643
AS075	0.292	0.298	0.298	0.519	0.531	0.531	0.631	0.646	0.647
AS080	0.293	0.299	0.299	0.519	0.531	0.531	0.632	0.651	0.651
AS085	0.294	0.298	0.299	0.519	0.531	0.532	0.635	0.654	0.655
AS090	0.300	0.307	0.307	0.520	0.531	0.531	0.640	0.654	0.655
AS095	0.300	0.306	0.307	0.521	0.532	0.533	0.648	0.661	0.661
AS100	0.301	0.308	0.308	0.513	0.533	0.533	0.648	0.658	0.659

Table 3.4 Resolutions of angulated lead collimators. Error on resolutions is ± 0.001 cm.

3.3.2.1 Geometric resolution

Since the collimators considered have different degrees of hole angulation, the geometric resolution cannot be expected to be identical. Table 3.4 shows that the geometric resolution generally increases with hole angulation at FWHM, FWTM and $FW\frac{1}{100}M$. In increasing the hole angulation from 0° to 1°, the geometric resolution at FWHM increases from 0.253 to 0.301 cm, an increase of almost 19%. More significantly perhaps than the change in resolution with angulation is that the peak position of the response function is displaced. The displacement is given by $x = A\tan\theta$ where A is the hole length and θ the hole angulation. The displacements with hole angulation are given in table 3.5.

Collimator	Displacement (cm)
AS000	0.000
AS005	0.004
AS010	0.007
AS015	0.011
AS020	0.014
AS025	0.018
AS030	0.021
AS035	0.025
AS040	0.029
AS045	0.032
AS050	0.036
AS055	0.039
AS060	0.043
AS065	0.047
AS070	0.050
AS075	0.054
AS080	0.057
AS085	0.061
AS090	0.064
AS095	0.068
AS100	0.072

Table 3.5 Displacement of peak position with collimator angulation.

The displacements are small for all the angulations modelled (less than 1 mm). In practice, a collimator would contain a range of hole angles between these extremes, randomly orientated. The displacement and resolution would therefore vary over the surface of the collimator. Different adjacent angulations could therefore lead to the recorded intensity being increased in one location and decreased in another, when compared with the image from a perfect collimator, producing false hot and cold spots. This will be investigated in chapter four where images are assessed.

3.3.2.2 Geometric and penetrated resolution

Since the collimator dimensions and material are the same as the conventional collimator, apart from the hole angulation, a similar increase in width would be expected when penetrated photons are included. At FWHM and FWTM this is generally seen to be the case, with an average increase of 2.0% and 2.1%, respectively for the ideal case. The average increase in spatial resolution due to penetration measured at one hundredth of the

maximum is slightly less on average for the angulated collimators at 2.1% compared with 4.7% for the conventional collimator. Since it is at one hundredth of the maximum that the greatest effects of penetration are seen, this change in the average increase in spatial resolution with penetration is not too surprising. The smaller value can be explained when the thickness of lead that would be penetrated for photon angles corresponding to the FW $\frac{1}{100}$M is considered. Figure 3.6 depicts this situation, showing how for the photon direction τ a greater thickness of lead will be traversed by some photons for the non-zero value of hole angulation.

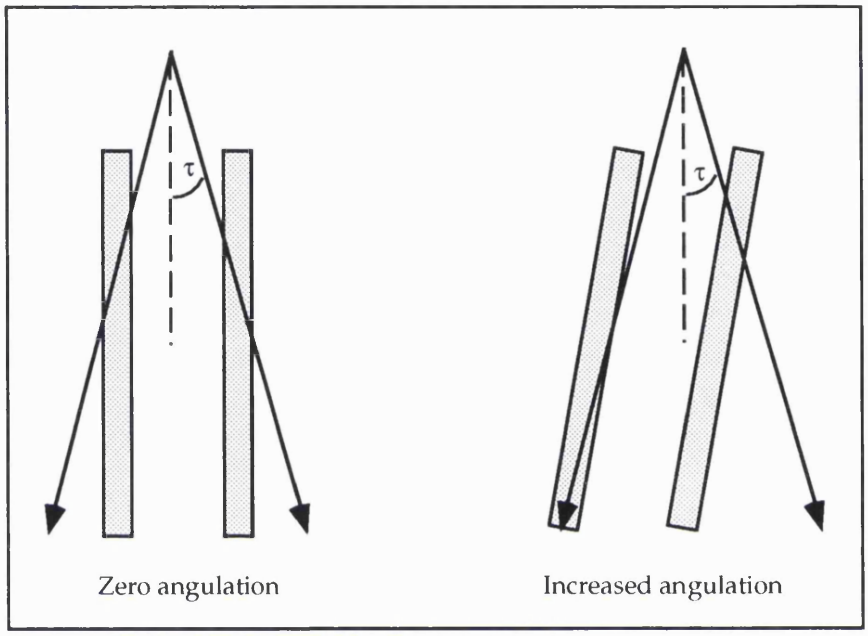

Figure 3.6 Effect of hole angulation on thickness of lead traversed.

For the case depicted in figure 3.6 the thickness of lead traversed by the photon travelling to the left is increased significantly, while the photon travelling to the right passes through a slightly decreased thickness.

3.3.2.3 Geometric, penetrated and scattered resolution

In the conventional collimator situation, there was little or no increase in the spatial resolution due to scattered photons. This would also be expected to be the case for the angulated collimators, since the collimator dimensions and materials do not change with hole angulation. Analysis of table 3.4 confirms this expectation at all measured spatial resolution heights.

Hole angulation in collimators therefore has two main effects; the first is that spatial resolution worsens with increase in hole angulation and the second is that the location of the peak position varies with hole angulation. For collimators with random hole angulations throughout these effects would result in a variable resolution over the surface of the collimator and spatial distortion, as previously described.

3.3.3 Laminated collimator response functions

The design and modelling of the laminated collimator were discussed in chapter two. To investigate the viability of a laminated structure, response functions were obtained for different layer thicknesses while keeping the hole length constant. The resolutions of the collimators, whose parameters are listed in table 3.1 are given in table 3.6.

NAME	FWHM (cm)			FWTM (cm)			FW $\frac{1}{100}$ M (cm)		
	G	G+P	G+P+S	G	G+P	G+P+S	G	G+P	G+P+S
M0100	0.253	0.264	0.266	0.511	0.531	0.536	0.616	1.047	1.157
M1000	0.256	0.275	0.277	0.519	0.548	0.553	0.634	3.447	3.456
M1640	0.255	0.281	0.283	0.527	0.565	0.569	0.644	3.937	3.942
M2158	0.255	0.289	0.290	0.534	0.576	0.579	0.647	3.309	3.319
M3727	0.254	0.313	0.315	0.558	1.276	1.282	0.660	3.921	3.928
M8200	0.255	0.352	0.355	0.575	1.766	1.769	0.701	1.988	2.008

Table 3.6 Resolutions of laminated collimators. Error on resolutions is ± 0.001 cm.

3.3.3.1 Geometric resolution

As expected, the geometric resolution for each of the laminated collimators is similar to that of the conventional lead collimator of the same dimensions.

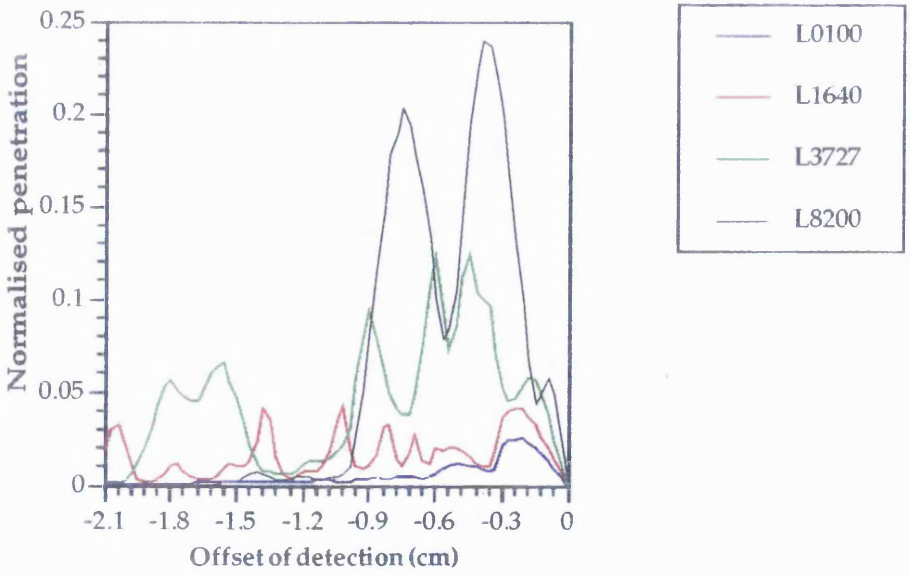

Figure 3.7 Penetration components of laminated collimators.

3.3.3.2 Geometric and penetrated resolution

Since there is a smaller quantity of lead in the laminated collimators, a greater degree of penetration is expected than in the case of the conventional lead collimator. The penetration components of four of the laminated collimators are shown in figure 3.7. The quantity of penetration increases with increase in layer thickness, despite the fact that the total quantity of lead in each of the laminated structures is approximately equal. The reason for the increase in penetrated photons with layer thickness is because the chances of a photon travelling through a septum without entering lead are increased as the thickness of the layers increases as shown in figure 3.8.

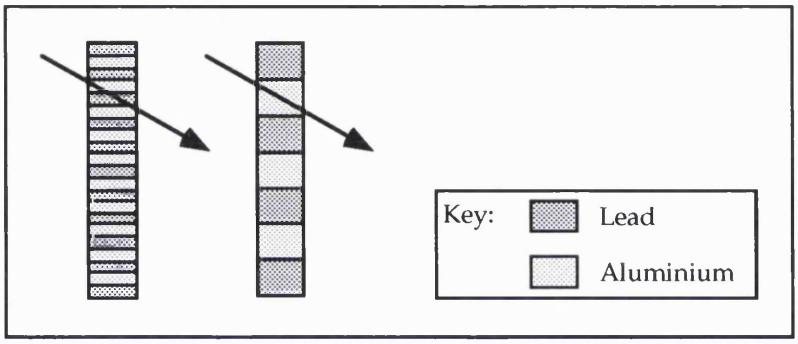

Figure 3.8 Diagram to indicate the increased probability of a photon passing through a septum in aluminium as the layer thickness is increased.

The geometric and penetrated resolution components listed in table 3.5 are greater than the corresponding resolution of the conventional lead collimator, for each of the laminated structures modelled. At FWHM and FWTM, the geometric and penetrated resolution worsens with increase in layer thickness. The resolution measured at one hundredth of the maximum initially increases with increase in layer thickness and then fluctuates, always remaining higher than the collimators with the narrowest layer thickness. The decrease in resolution at FW$\frac{1}{100}$M for collimator M8200 is due to the increased amount of lead that would need to be traversed.

From the laminated collimators modelled therefore, M0100 provides the best resolution when geometric and penetrated photons are considered. A comparison with the conventional lead collimator, C24 shows M0100 to have a very slight increase in resolution ant FWHM and FWTM while the increase in resolution at FW$\frac{1}{100}$M is greater.

3.3.3.3 Geometric, penetrated and scattered resolution

The inclusion of scattered photons produces a slight increase in resolution measured at FWHM, FWTM and FW$\frac{1}{100}$M for all the laminated collimators modelled. In the case of the conventional collimator (C24), however, the inclusion of scattered photons did not affect the resolution. For the laminated collimator with the best resolution

(M0100), scattered photons worsen the resolution by approximately 10% (1.1 mm) at FW$\frac{1}{100}$M and less than 1% (~0.05 mm) at FWHM and FWTM.

3.3.3.4 Assessment of laminated structure response functions

From the discussion on laminated collimator response functions it would appear that the laminated structure might provide a viable alternative to the conventional lead collimator. The best of the response functions obtained produced very similar resolutions to the conventional collimator at FWHM and FWTM and a slightly worse resolution at FW$\frac{1}{100}$M. The degradation in resolution is caused by both penetrated and scattered photons, penetration having the greatest effect. The values obtained suggest that collimator M0100, which has a layer thickness of 0.01 cm would produce a viable alternative to the conventional lead collimator.

3.3.4 Sandwich collimator response functions

The sandwich structure collimators, which were discussed in chapter two, consist of two layers of lead of equal thickness separated by a layer of aluminium. The resolutions of four such collimators are given in table 3.7.

NAME	FWHM (cm)			FWTM (cm)			FW$\frac{1}{100}$M (cm)		
	G	G+P	G+P+S	G	G+P	G+P+S	G	G+P	G+P+S
S49	0.255	0.488	0.495	0.579	1.748	1.753	0.712	2.491	2.559
S73	0.253	0.365	0.368	0.584	1.174	1.749	0.764	1.353	1.391
S88	0.254	0.337	0.339	0.588	0.629	0.637	0.795	1.317	1.331
S98	0.255	0.336	0.338	0.590	0.597	0.602	0.826	0.873	0.970

Table 3.7 Resolutions of sandwich collimators. Error on resolutions is ± 0.001 cm.

3.3.4.1 Geometric resolution

Once again, the geometric resolutions of all sandwich collimators are similar to the conventional lead collimator, as expected with identical collimator dimensions.

3.3.4.2 Geometric and penetrated resolution

The geometric and penetrated resolution of the sandwich structure collimators improves as the thickness of aluminium is reduced, as expected. However the best resolution obtained, from S98, is significantly worse than the conventional lead collimator with increases of 30% (0.78 mm), 15% (0.79 mm) and 39% (2.43 mm) at

FWHM, FWTM and FW$\frac{1}{100}$M, respectively, despite the small quantity of aluminium present.. This type of structure is therefore not a viable alternative to the conventional lead collimator.

3.3.4.3 Geometric, penetrated and scattered resolution

For the best of the sandwich structure collimators, the amount of scatter detected is small. The resolution is however poor, as was discussed when geometric and penetrated photons alone were considered.

3.3.4.4 Assessment of sandwich structure response functions

The response functions obtained from the sandwich collimator do not suggest that such a structure is a possible alternative to the conventional lead collimator. Excessive penetration and scatter occurs and there is little advantage in weight or rigidity of the collimator.

3.3.5 Alternative material collimator response functions

Collimator response functions have been obtained for two alternative materials - tungsten and uranium using the conventional collimator dimensions. As discussed in chapter two, these materials have better attenuation properties than lead so that fewer non-geometric photons will be expected in an image. The resolutions of the uranium, tungsten and lead collimators, with conventional dimensions are given in table 3.8 and the total response functions are plotted in figure 3.9.

NAME	FWHM (cm)			FWTM (cm)			FW$\frac{1}{100}$M (cm)		
	G	G+P	G+P+S	G	G+P	G+P+S	G	G+P	G+P+S
U24	0.252	0.254	0.255	0.507	0.511	0.511	0.604	0.618	0.618
W24	0.256	0.259	0.259	0.513	0.514	0.517	0.604	0.625	0.626
C24	0.253	0.258	0.258	0.507	0.518	0.518	0.602	0.630	0.630

Table 3.8 Resolutions of uranium, tungsten and lead collimators of conventional dimensions. Error on resolutions is ± 0.001 cm.

3.3.5.1 Geometric resolution

As expected the geometric component of the response function is very similar for the three collimators modelled.

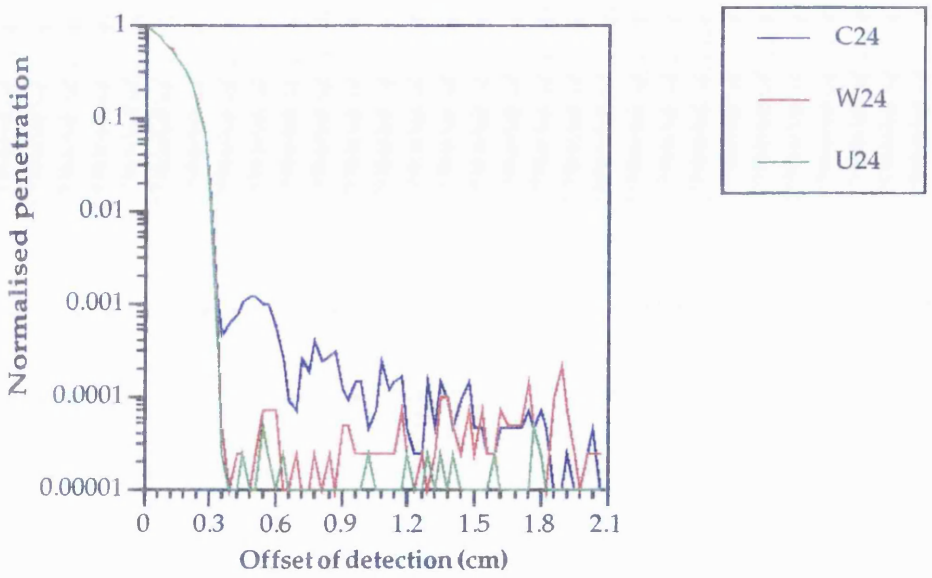

Figure 3.9 Response functions from alternative material collimators.

3.3.5.2 Geometric and penetrated resolution

Similar values are obtained for the geometric and penetrated resolutions of the three different material collimators indicating that uranium and tungsten are equally as good as lead for use as collimator materials. Since no significant advantage is seen in the resolutions of the uranium and tungsten, however, the increased cost of constructing conventional dimension collimators from these materials would not be sensible.

3.3.5.3 Geometric, penetrated and scattered resolution

At FWHM, FWTM and FW$\frac{1}{100}$M, the resolution values of the three collimators are similar. The log plot of figure 3.9 shows that the total response functions differ in the tails, fewer photons contributing to the uranium collimator than the other two. The result, however, does not indicate a real advantage in the use of either uranium or tungsten in collimators of these dimensions.

3.3.5.4 Assessment of alternative material collimators of conventional dimensions

Uranium and tungsten were chosen as possible alternatives to lead for use in collimators due to their high attenuating properties. A comparison of their response functions with that of lead, however, does not indicate any significant improvement in resolution. However, due to the improved attenuation properties of uranium and tungsten, equally good resolution might be attainable with narrower septa, which would result in an improved efficiency.

3.3.6 Response functions of uranium collimators of various septal thicknesses

Uranium has been shown to have better attenuation properties than either lead or tungsten and therefore a uranium collimator with narrow septa might produce a similar resolution to that of a lead collimator of conventional dimensions. This section presents the response functions obtained from uranium collimators with different septal thicknesses. The resolutions of these collimators are presented in table 3.9 while plots of the response functions are given in figure 3.10.

NAME	FWHM (cm)			FWTM (cm)			FW$\frac{1}{100}$M (cm)		
	G	G+P	G+P+S	G	G+P	G+P+S	G	G+P	G+P+S
U05	0.252	0.255	0.255	0.508	0.514	0.514	0.607	0.966	0.971
U10	0.253	0.255	0.256	0.506	0.510	0.511	0.606	0.620	0.620
U15	0.253	0.255	0.255	0.508	0.512	0.512	0.603	0.617	0.618
U20	0.255	0.257	0.257	0.507	0.512	0.512	0.605	0.619	0.619
U24	0.252	0.254	0.255	0.507	0.511	0.511	0.604	0.618	0.618

Table 3.9 Resolutions of uranium collimators of various septal thicknesses. Error on resolutions is ± 0.001 cm.

3.3.6.1 Geometric resolution

The geometric resolutions obtained for each septal thickness give approximately the same value as the conventional lead collimator. This is to be expected since the geometric resolution is not dependent on the septal thickness.

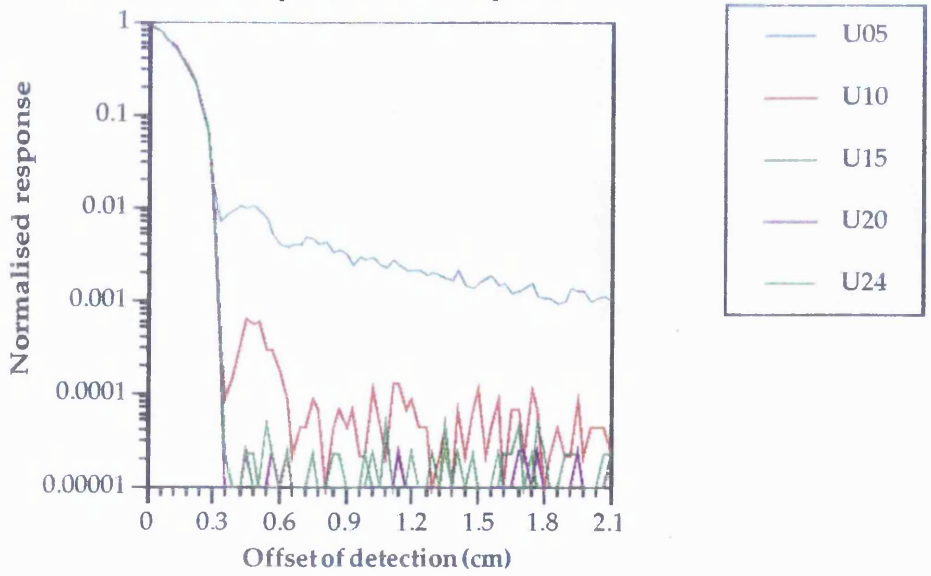

Figure 3.10 Response functions of uranium collimators of various septal thicknesses. Hole size flat-to-flat = 0.25 cm, hole length = 4.1 cm.

3.3.6.2 Geometric and penetrated photons

The main advantage in the use of uranium in a collimator is that its high photon attenuation should enable thinner septa to be used, thus improving efficiency without degrading resolution. Analysis of the geometric and penetrated resolutions given in table 3.8 shows that at FWHM and FWTM each of the collimators modelled produces similar resolution values to those of the conventional lead collimator. However at FW$\frac{1}{100}$M, excessive penetration occurs in the case of U05, which has a septal thickness of 0.005 cm. The remaining collimators behave similarly to one another. Using Anger's efficiency equation (equation 1.3), collimator U10 (septal thickness = 0.010 cm) is 11% more efficient than collimator U24 (septal thickness = 0.024 cm). Providing the scattered component of the response functions is also similar to that of the conventional lead collimator, U10 would appear a good choice in terms of resolution and efficiency.

3.3.6.3 Geometric, penetrated and scattered photons

The inclusion of scattered photons only affects the response function of collimator U05 significantly. The remaining collimators all produce resolutions similar to each other and to that of the conventional lead collimator.

3.3.6.4 Assessment of narrow septa uranium collimator response functions

Of the collimators modelled, the resolutions of all, except the narrowest septa collimator U05, were comparable to that of the conventional lead collimator. The efficiencies of the collimators increases as the septal thickness decreases, a fact probably more significant in SPECT imaging than in planar imaging. From these considerations, collimator U10, of septal thickness 0.010 cm, will be selected as a collimator to be modelled.

3.4 Conclusions on collimator response functions

This chapter has been concerned with assessing the response functions of various types of collimator. Firstly, response functions were obtained for conventional lead collimators of various septal thicknesses. Excessive penetration occurred in collimators with septal thicknesses of less than 0.020 cm, and a septal thickness of 0.024 cm was selected as a suitable thickness for good spatial resolution.

The main effects of hole angulation on response functions were found to be a worsening of the spatial resolution together with spatial distortions. The response functions obtained were for slant hole collimators. The effects of random hole angulations on images will be assessed in the next chapter.

Two types of layered collimator structure were assessed as alternatives to the conventional lead collimator. The purpose behind assessing these types of structure was to provide an increased rigidity to the collimator together with a slight reduction in weight. One type of layered structure considered was a sandwich structure. This was not found to be successful, resulting in significant penetration causing a worsening in spatial resolution. The second type of layered collimator considered was a laminated structure. Layer thicknesses of 0.010 cm were found to produce a spatial resolution similar to that of the conventional lead collimator at FWHM and FWTM. At FW$\frac{1}{100}$M the spatial resolution of this layered collimator was increased by approximately 1.1 mm. The laminated collimator would give an added rigidity, and a layer thickness of 0.01 cm is thin enough for mechanical pressing of the holes.

Finally, alternative materials were investigated for use in collimators. Two different material collimators were modelled — uranium and tungsten. Both materials have better attenuation properties than lead which should decrease the quantity of non-geometric photons in an image. When conventional dimensions were used for the collimators, however, no significant benefit was seen in the use of either uranium or tungsten. This is due to the fact that the penetrated photons contributing to the response function are mainly those that have penetrated the edges of the septa, rather than penetrating whole septa. The benefit of using alternative materials was seen when narrower septa collimators were considered. Little difference was made to the resolution at FWHM, however a uranium collimator of septal thickness 0.010 cm provided a resolution at FWTM, which was as good as that of the lead collimator of 0.024 cm septal thickness.

The following chapter will investigate images of the line source phantom using some of these collimators. The effects of random hole angulation on images will be considered. Images will be obtained from the laminated collimator and for the uranium collimators of conventional and narrow septal thicknesses.

- 4 -

New Collimators

Although the collimator response functions presented in chapter three provide useful information about gamma camera collimators, the true test of any collimator is in the quality of image it produces. Image quality can be assessed both quantitatively and qualitatively and this chapter seeks to do the former.

Images are presented which have been formed by the techniques described in chapter two using the collimator response functions presented in chapter three. Images are presented for five types of collimator: a perfect conventional lead collimator, a conventional lead collimator with random hole angulations, a laminated collimator, a uranium collimator of conventional septal thickness and a narrow septa uranium collimator. Each of these collimators has a flat-to-flat hole size of 0.25 cm, and a hole length of 4.1 cm. The first three collimators, all of which contain lead, and the first of the uranium collimators have a septal thickness of 0.024 cm, while the septal thickness of the narrow septa uranium collimator is only 0.010 cm.

4.1 Method of analysis of images

The data produced for each image is in the form of a series of arrays of photon positions. Each array contains photons which have undergone a particular interaction and have energies within a particular range. The arrays obtained have been listed in chapter two (section 2.3.1.4). The analysis of each image will be divided into two main sections; the first section will consider photons detected which have not undergone scatter in the object.

This section will the subdivide the photons detected into three subsections related to the transport of photons in the collimator: geometric photons, geometric and penetrated photons, and geometric, penetrated and scattered photons. The second main section to be considered will investigate photons which contribute to the final image that have undergone scatter in the object, looking at the contribution of photons in particular energy ranges to the final image. Finally, the complete image of all photons detected will be presented. In each of these sections, where relevant, the Gaussian fitting routine described in chapter two will be used to provide a measure of the resolution and spatial distortion of the images. The conventional lead collimator will be used as a standard with which all other collimators will be compared.

4.2 Images obtained from a conventional lead collimator

The images that are presented in this thesis have all been generated from the line source phantom simulation with the source at a distance of 10 cm from the collimator in the perspex scattering medium. All images are 40.96 cm x 40.96 cm square containing 2048 pixels of length 0.02 cm in the x direction and 16 pixels of length 2.56 cm in the y direction.

4.2.1 Comparison of the image obtained from geometric photons with the original source distribution

The ideal spatial resolution of a gamma camera collimator was seen in equation 1.3 to be proportional to the hole diameter; a high quality resolution being obtained for a small hole diameter. This was however shown to be in contradiction to the large hole diameter required for high efficiency. There is also a disagreement in the consideration of the optimum hole length, a short hole being desirable for high efficiency, while a long hole is required for high resolution. Since a compromise between resolution and efficiency is required, the PSF of the collimator has a finite width rather than being a delta function, and similarly, the width of a line in an image will be greater than the width of the line source.

Figure 4.1 Geometric image from (a) hypothetical situation where no spread occurs and (b) conventional lead collimator.

Figure 4.1 shows the images obtained from (a) a hypothetical situation where there is no spread in the response function due to collimator dimensions (i.e. no angular spread in detected photons), and (b) from an ordinary collimator, considering only those photons which do not enter the lead septa. The line sources are situated 10 cm above the collimator, in a perspex scattering medium. Only those photons which do not undergo scattering in the phantom are considered. The image using the ordinary collimator is therefore the best possible image that could be obtained from it, since no penetration or scatter is included.

Table 4.1 compares the average resolution of the true image of geometric photons in the ordinary collimator with that of the hypothetical situation.

	Hypothetical situation (mm)	Ordinary collimator (mm)	Increase in width (mm)	% increase in width
FWHM	0.5	7.88 ± 0.11	7.38 ± 0.11	1475
FWTM	0.5	14.35 ± 0.20	13.85 ± 0.20	2771

Table 4.1 Geometric resolutions for an ideal collimation system and a conventional lead collimator.

At this source height, there is a large increase in the line width when an ordinary collimator is used which is due to the angular range of the photons which pass through the collimator holes. At smaller heights this spread would be smaller, and would increase with increase in source height. The change in resolution with source height has consequences when imaging a patient, since not all activity will be at the same depths.

4.2.2 Effect of collimator penetration on images

Section 4.2.1 showed that an ordinary collimator, while clearly showing the seven lines in the phantom, accepts a much wider angular range of photons than would an ideal collimation system, producing a wider line than is present in the phantom. Although this spread is undesirable, for a particular collimator an image which consists only of geometric photons is the best possible image which could be obtained when using that collimator, i.e. we have 100% absorption of photons entering the septa. In practise it has been seen that some of the photons entering the septa will be detected.

Figure 4.2 considers the effect that penetrated photons have on the image. In (a) the ideal case of no penetration is seen. The image of the penetrated photons alone is seen in (b) while (c) shows the image of the combined geometric and penetrated photons. The seven lines are clearly visible but are broader in (b) than in (a) as expected due to the wider angular range of the penetrated photons. The intensity of penetrated photons is much smaller than that of the geometric photons. The combination of the penetrated photons with the primary photons, produces the image shown in figure 4.2 (c), and the resolution values obtained from the Gaussian fitting routine are tabulated in table 4.2.

Figure 4.2 Effect of collimator penetration on image: (a) Geometric photons alone, (b) Penetrated photons alone, (c) Geometric and penetrated photons.

	Geometric photons (mm)	**Geometric and penetrated photons (mm)**	**Increase in width (mm)**
FWHM	7.88 ± 0.11	7.98 ± 0.15	0.11 ± 0.19
FWTM	14.35 ± 0.20	14.55 ± 0.28	0.19 ± 0.34

Table 4.2 Effect of penetrated photons on resolution of conventional lead collimator images.

The measurements on the resolution given in table 4.2 indicate only a small increase in the width (approx. 0.1 mm) of the FWHM when penetrated photons are added to the image.

4.2.3 Effect of collimator scatter on the image

In addition to the geometry of the collimator, and the effects of penetrated photons, a further inherent defect in collimators which causes a worsening of images is scatter. At the energies used for gamma camera imaging the two types of scatter which occur are Compton and coherent scatter. Compton scatter is inelastic, the energy of the scattered photon being dependent on the angle through which it has been scattered. Because of this it is possible to limit the scattered photons which contribute to an image by setting an energy window on the camera. A typical window setting used for Tc-99m is 20% of the 140 keV photon peak, i.e. ± 10%, this corresponds to photons of energies between 126 keV and 154 keV. The maximum angle through which a photon can be scattered in lead (single Compton scatter) and for its energy still to lie within the window is approximately 55° (calculated using the Compton wavelength shift formula; appendix 3). If a photon entering the collimator was immediately scattered through 55° subsequently being detected with no further scatter it would have deviated from the position it would have been detected by 5.9 cm. Thus it is possible for single Compton scattered photons to undergo a considerable displacement, worsening the image. At these energies coherently scattered photons will typically be scattered through angles smaller than 10°, resulting in a shift of less than 1 cm. Greater deviations than these can occur if multiple scatter takes place, although multiple Compton scattered photons will probably have energies below the cut off energy.

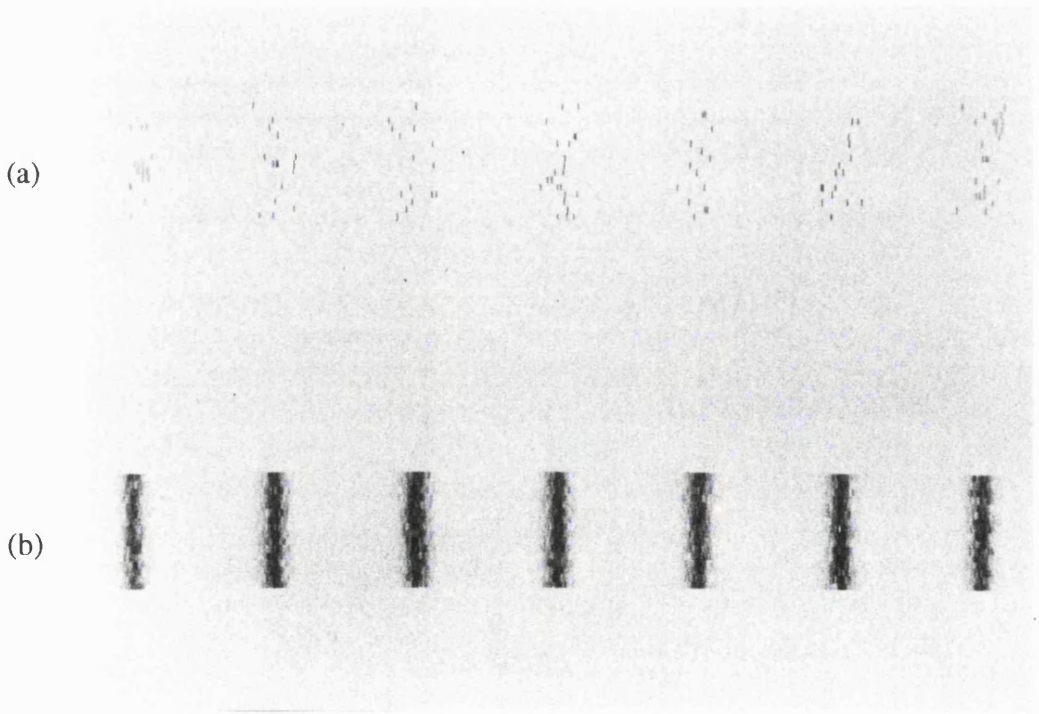

Figure 4.3 Effect of collimator scatter: (a) Image of photons scattered in collimator, (b) Image of geometric, penetrated and scattered photons.

The image of photons scattered in the collimator (but not in the phantom) is shown in figure 4.3(a). The figure shows very few scattered photons in the image, and that the detected photons are positioned where the image of the line source would be expected. Thus only photons scattered through small angles will be detected. Figure 4.3(b) shows the image obtained when photons which are not scattered in the phantom but reach the crystal (i.e. geometric, penetrated and scattered) are included in the image. The seven lines are clearly visible and do not appear noticeably different from the image containing geometric and penetrated photons alone.

Table 4.3 shows how the inclusion of scatter and penetration with the geometric photons changes the resolution when compared with the geometric and penetrated photon image. The increase in width is negligible.

	Geometric and penetrated photons (mm)	Geometric, penetrated and scattered photons (mm)	Increase in width (mm)
FWHM	7.98 ± 0.15	8.00 ± 0.22	0.02 ± 0.27
FWTM	14.55 ± 0.28	14.59 ± 0.40	0.04 ± 0.48

Table 4.3 Effect of penetrated and scattered photons on resolution of a conventional lead collimator.

4.2.4 Effect of object scatter on the image

Whereas the proportion of photons which have undergone septal penetration and collimator scatter can be changed by collimator design, the degree of scatter in the object is independent of the collimator. The photons detected which have undergone scatter in the object can only be minimised by setting an appropriate energy window on the camera. For completeness, however, the effect on the image of object scatter is shown in figure 4.4 for both the collimator image (b), and the system image (c) (collimator image convolved with intrinsic resolution). The image of photons not scattered in the phantom is shown for purposes of comparison in (a).

Including scatter from the phantom clearly gives a less distinct image due to the photons which are detected in between the line sources. However the line sources are still clearly visible and distinguishable. Convolving the collimator image with the intrinsic resolution gives a smoother image in which the line sources appear straighter. Setting a window to exclude all counts below a minimum value from the image gives a much clearer image for the system image (d) without seeming to lose information within the lines.

Figures 4.5, 4.6 and 4.7 show the images formed by photons scattered in the phantom when the transport through the collimator is considered. Photons which pass through the holes, not entering lead are shown in figure 4.5 for energy ranges (a) $125 \leq E < 135$ keV, (b) $130 \leq E < 135$ keV, (c) $135 \leq E < 140$ keV and (d) $E = 140$ keV.

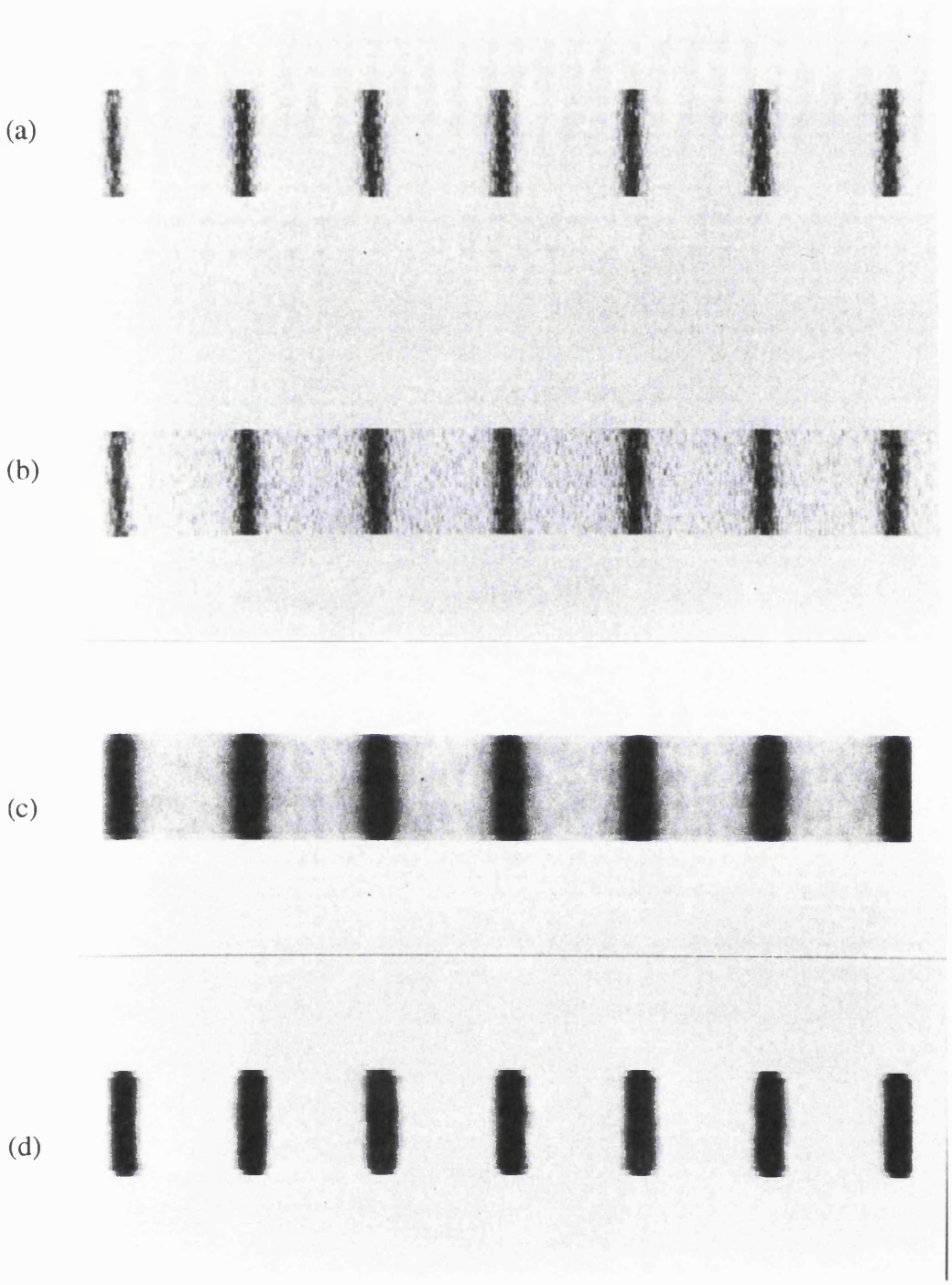

Figure 4.4 Effect of object scatter on the image: (a) Image of all detected photons not scattered in object, (b) Image of all photons at crystal face, (c) System image obtained by convolution with intrinsic resolution, (d) System image with count window set.

No obvious structure is visible in figure 4.5 (a) to (c) while (d) shows some photons where the line sources would be expected and very little elsewhere, as would be expected due to the small scattering angle if $\Delta E = 0$.

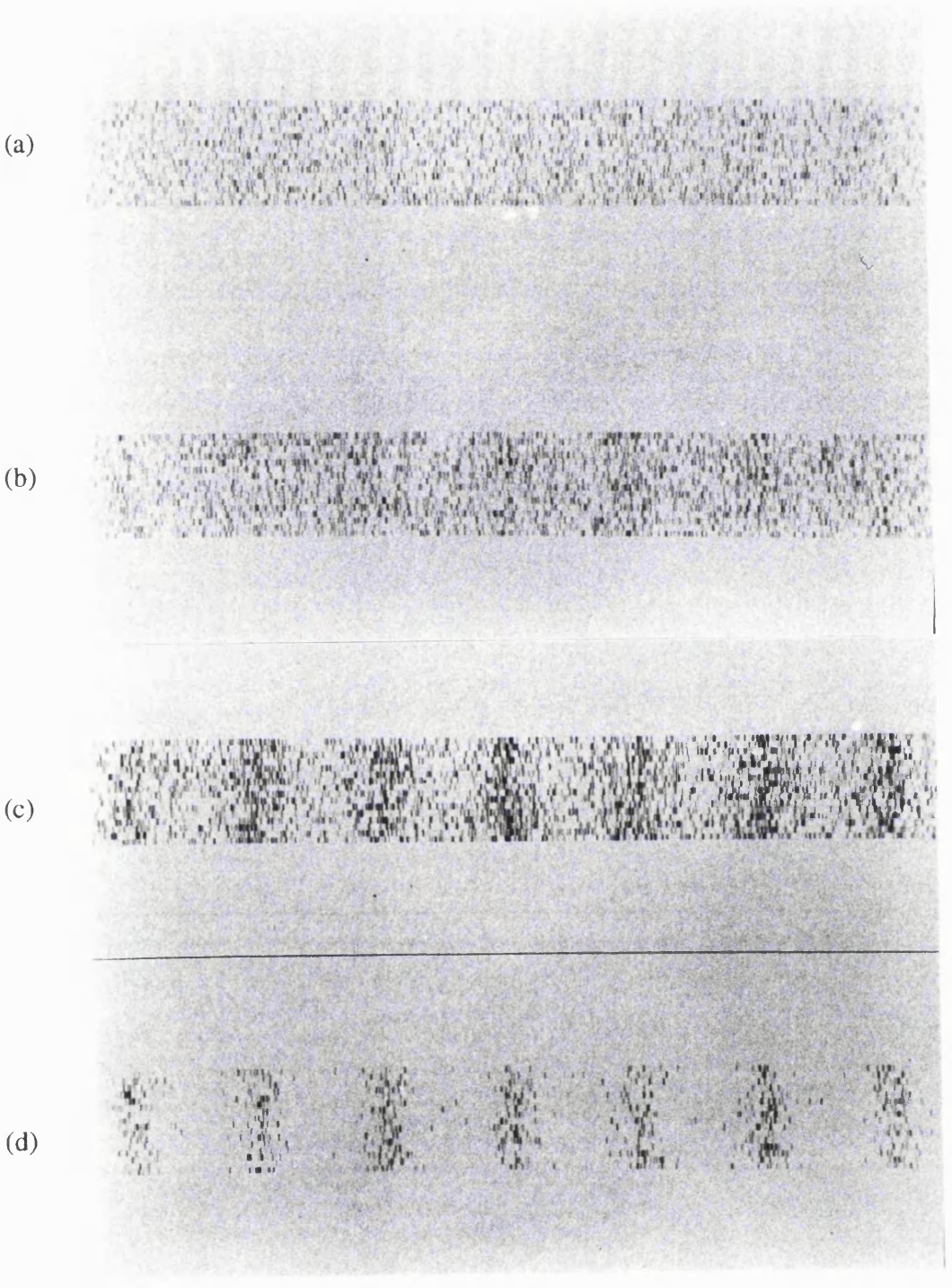

Figure 4.5 Image of photons which have been scattered in the object but pass geometrically through the collimator holes for the energy ranges: (a) $125 \leq E < 130$ keV, (b) $130 \leq E \leq 135$ keV, (c) $135 \leq E \leq 140$ keV, (d) $E = 140$ keV.

In figure 4.6 those photons which penetrate lead without undergoing scatter in the collimator are shown for the same energy ranges. Again no obvious structure is evident for

the three lower energy ranges [(a), (b) and (c)] while for E = 140 keV [(d)] some photons are present under the line sources producing broad lines.

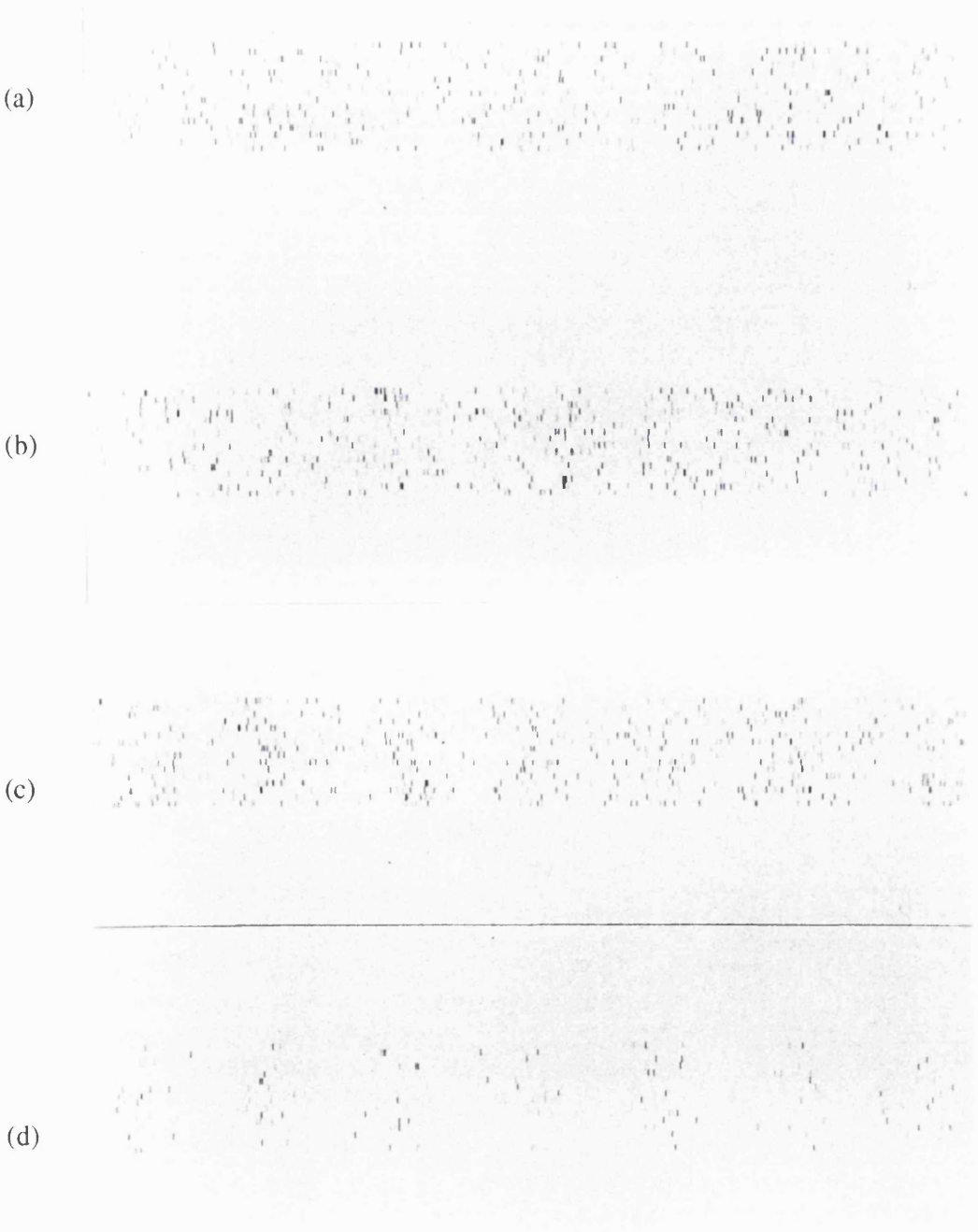

Figure 4.6 Image of photons which have been scattered in the object and penetrate collimator septa without scattering for the energy ranges: (a) $125 \leq E < 130$ keV, (b) $130 \leq E \leq 135$ keV, (c) $135 \leq E \leq 140$ keV, (d) $E = 140$ keV.

Figure 4.7 shows the images obtained from photons scattered in both object and collimator. There are very few photons in any of the energy ranges, which is expected from the consideration of collimator scatter in the previous section.

(a)

(b)

(c)

(d)

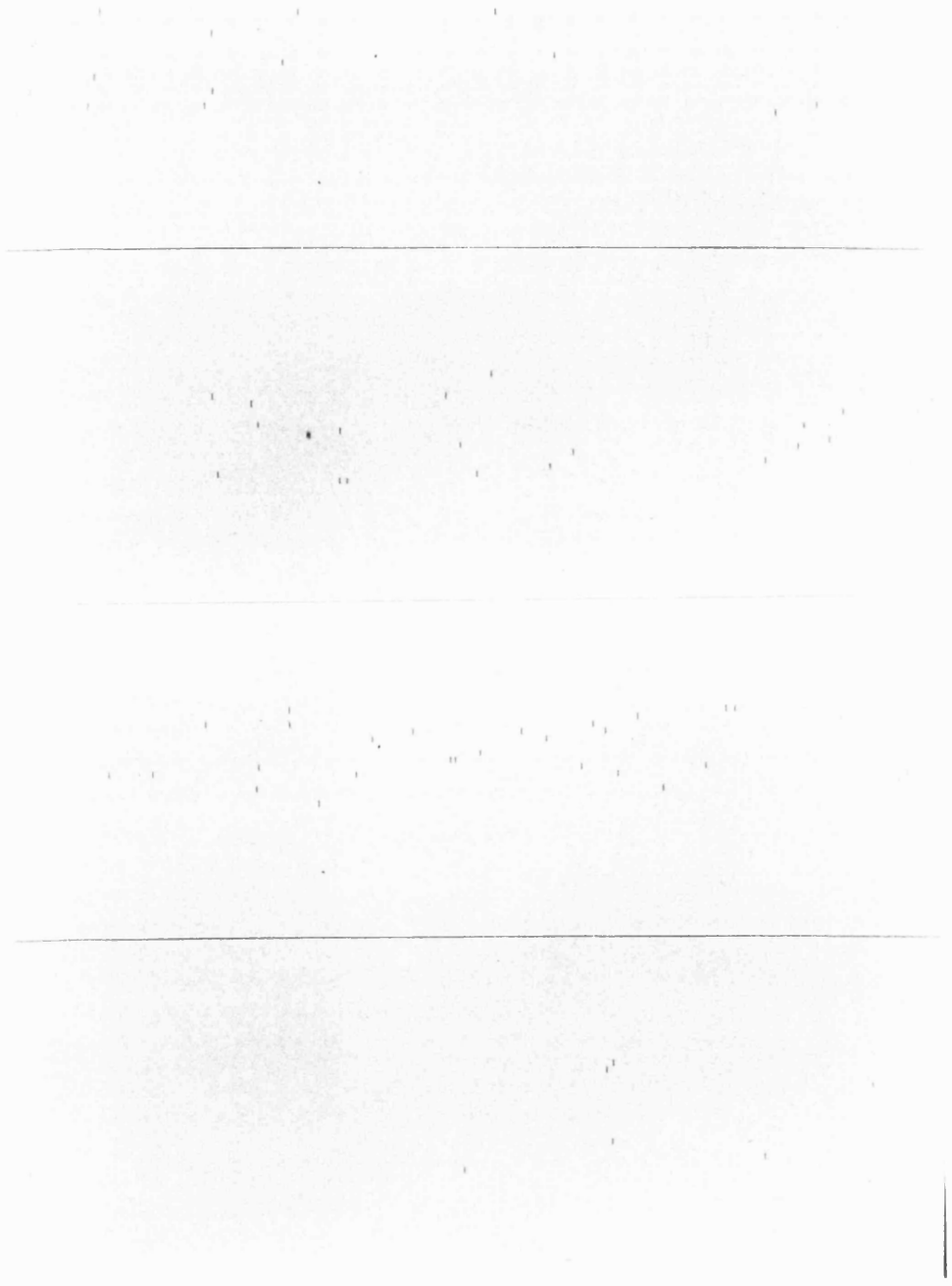

Figure 4.7 Image of photons which have been scattered in the object and scatter in collimator septa for the energy ranges: (a) $125 \leq E < 130$ keV, (b) $130 \leq E \leq 135$ keV, (c) $135 \leq E \leq 140$ keV, (d) $E = 140$ keV.

The inclusion of object scatter has been shown to worsen the image in figure 4.4. Table 4.4 lists the mean values of the FWHM and FWTM for the lines with the inclusion of object scatter (unconvolved and convolved) compared with the case of no object scatter.

	No object scatter	Object scatter		Increase in unconvolved resolution (mm)
	Unconvolved resolution (mm)	Unconvolved resolution (mm)	Convolved resolution (mm)	
FWHM	8.00 ± 0.22	11.67 ± 1.47	9.19 ± 0.37	3.67 ± 1.49
FWTM	14.59 ± 0.40	21.27 ± 2.68	16.76 ± 0.67	6.68 ± 2.71

Table 4.4 Effect of object scatter on image resolution.

The actual increase in the width of the lines in the unconvolved images is very large (approximately 50% of the increase from the width of the line sources to the image of geometric photons). However, the standard deviations on the measurements in the unconvolved image when object scatter is included indicate the range of widths obtained suggesting a problem with fitting a Gaussian to each line segment. The resolution values obtained for the convolved image and the corresponding image in figure 4.4 shows that the non-uniformity of the scatter in the unconvolved case is dealt with by the smoothing effect of the convolution.

4.2.5 Discussion on image formation using a conventional collimator

Sections 4.2.1 to 4.2.4 presented the images obtained when various collimator effects were added. The major effect on the resolution from the ideal image is known to be due to the hole diameter and length, but considerations of efficiency limit the quality of resolution possible were the collimator to be otherwise ideal (no penetration or scatter). For the collimator imaged, the effect of penetration on the image is worse than the effect of scatter, due to the greater number of penetrated photons. The addition of penetrated photons to the image increase the mean width of the line at FWHM by approximately 0.11 mm from the geometric image. The inclusion of photons scattered in the object also worsens the resolution noticeably, increasing the FWHM by approximately 1.31 mm from the geometric case.

4.3 Images obtained from collimators with random hole angulations

In order to investigate the effects of hole angulation on gamma camera images three different angulation files were generated. The angulations considered were distributed by assuming the width of the Gaussian at one hundredth of the maximum value to correspond to a particular angle. These angulations are tabulated in table 4.5.

Collimator	Width at 0.01 of maximum (°)
A1	1
A2	2
A4	4

Table 4.5 Angulated collimators.

The Gaussian distributions were only sampled between ±1°, as shown in figure 4.8. The images obtained from the line source phantom are described below and compared with the images of the conventional lead collimator.

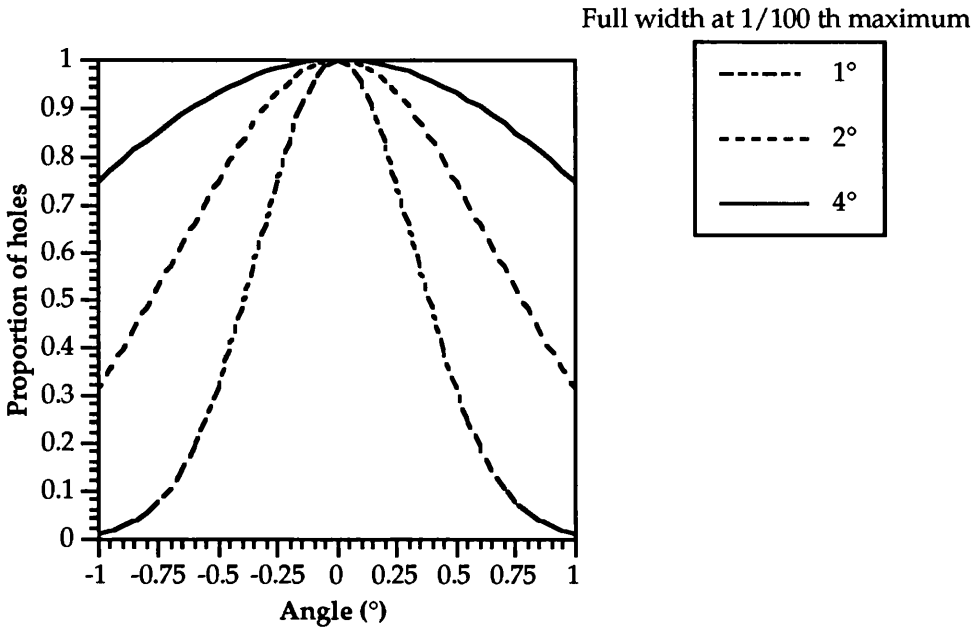

Figure 4.8 Gaussian distributions used for sampling of hole angulations.

4.3.1 Geometric photon image

The response functions for the angulated collimators were presented in section 3.3.2 and it was demonstrated that although the resolution did worsen with increase in hole angulation, the change was very small. The major difference seen in the consideration of the response functions was in the position of the peak of the response, which, for a source height of 10 cm and a hole angulation of 1°, shifted approximately 2.6 mm. When the randomly angulated collimator is considered, the holes have angles which are sampled from a Gaussian distribution, so that although an angle of 1° is possible, the majority of holes will have much smaller angles. Table 4.6 lists the percentage of holes with angles between particular values for each of the collimators considered in this section.

Collimator	Angular range (°)	%
A0	0.00 - 0.25	100
	0.25 - 0.50	0
	0.50 - 0.75	0
	0.75 - 1.00	0
A1	0.00 - 0.25	55
	0.25 - 0.50	32
	0.50 - 0.75	11
	0.75 - 1.00	2
A2	0.00 - 0.25	34
	0.25 - 0.50	29
	0.50 - 0.75	23
	0.75 - 1.00	24
A4	0.00 - 0.25	22
	0.25 - 0.50	24
	0.50 - 0.75	27
	0.75 - 1.00	27

Table 4.6 Percentage of holes within angular ranges for angulated collimators.

The average response functions for each of these collimators calculated from these percentages are shown in figure 4.9. The approximate FWHMs of the response functions vary from 0.26 mm for the perfect collimator (A0) to 0.29 mm for collimator A4, a difference of only 0.03 mm. A2 and A4 have very similar responses and are virtually indistinguishable in figure 4.9, forming the responses displaced furthest to the left. The position of the centroid can be seen to shift as the angulation increases.

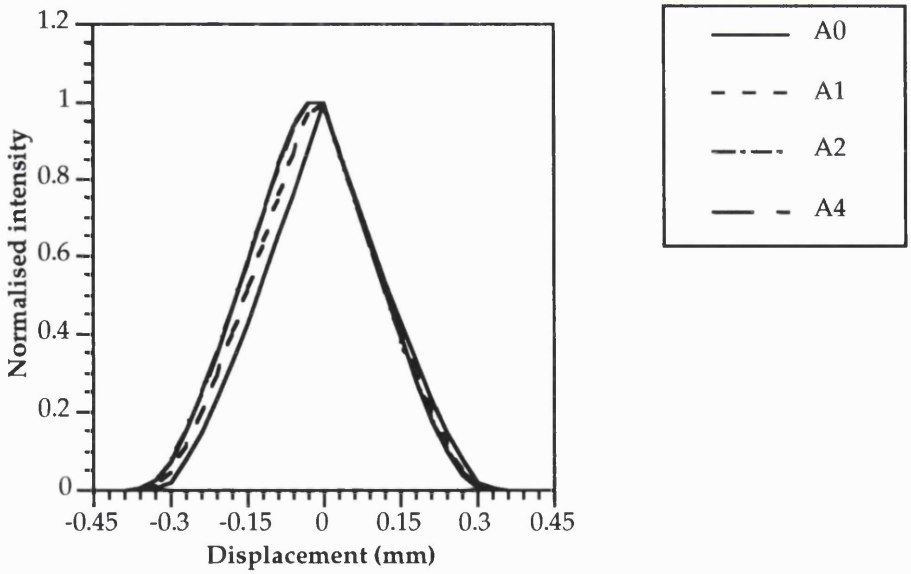

Figure 4.9 PSFs averaged over angular distribution for angulated collimators.

Figure 4.10 shows the images of the geometric photons for the conventional lead collimator (a) and the angulated collimators ((b)-(d)). The images are all very similar in appearance, no obvious difference in the width of the lines being evident, as is expected when the distribution of the holes is seen.

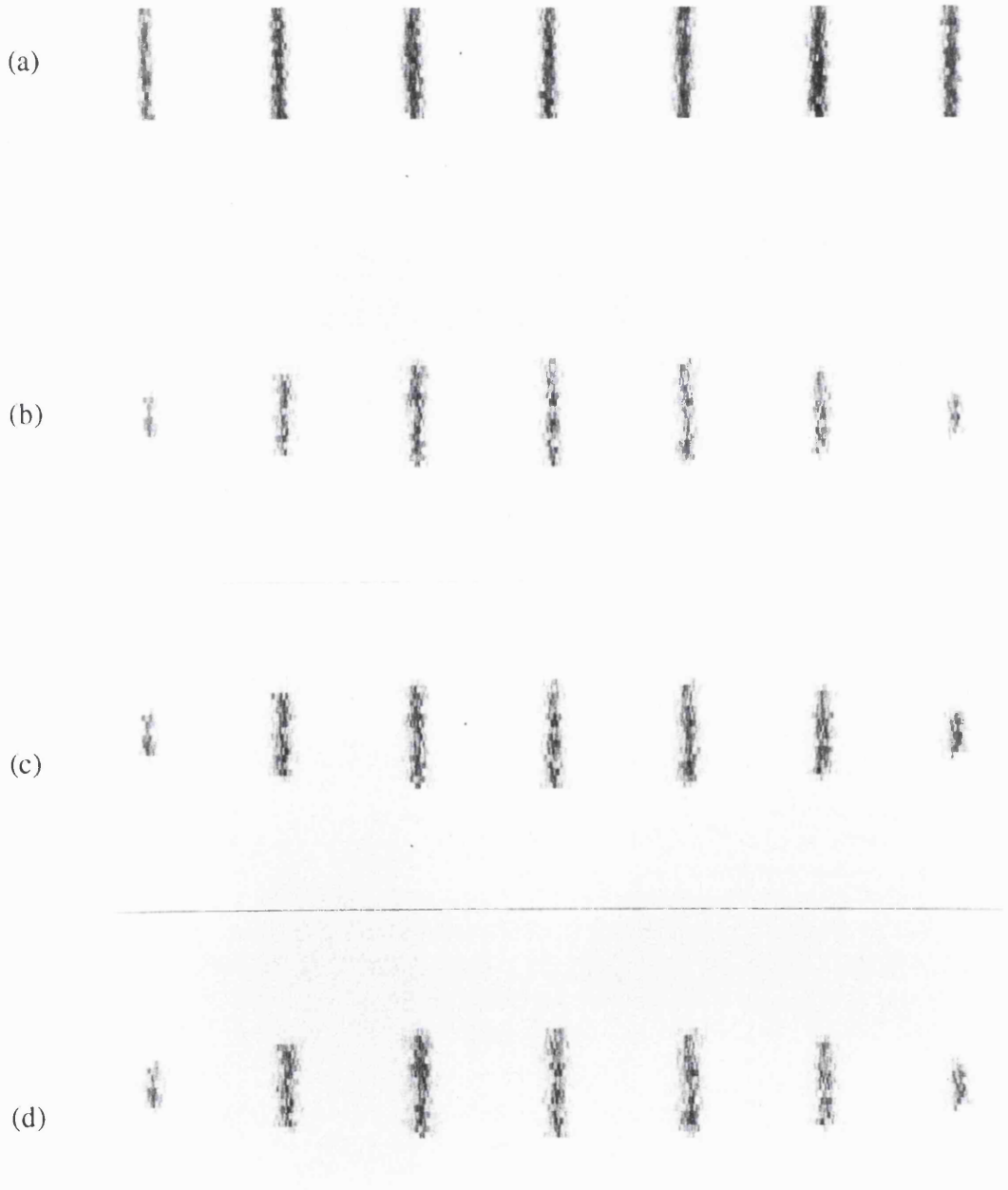

Figure 4.10 Geometric images: (a) A0; (b) A1; (c) A2 and (d) A4.

When a Gaussian fit is effected to each of the lines to determine the FWHM and FWTM a slight increase is seen as the angulation of the holes is increased (table 4.7).

Collimator	A0 (mm)	A1 (mm)	A2 (mm)	A4 (mm)
FWHM	7.88 ± 0.11	8.28 ± 0.15	8.43 ± 0.24	9.49 ± 0.57
FWTM	14.35 ± 0.20	15.10 ± 0.27	15.36 ± 0.44	17.29 ± 1.04

Table 4.7 Resolution of angulated collimator from line source measurements.

When the position of the peak of the fitted Gaussians in considered there is no obvious shift from the expected position, however, the mean and maximum deviations of the centroids worsen with increase in angulation (table 4.8).

Collimator	A0 (mm)	A1 (mm)	A2 (mm)	A4 (mm)
Mean deviation	0.16 ± 0.02	0.27 ± 0.16	0.36 ± 0.20	0.40 ± 0.15
Max. deviation	0.4	1.4	1.6	1.8

Table 4.8 Deviation of centroids in angulated collimators.

4.3.2 System images from angulated collimators

The images of the geometric photons showed few differences between the perfect collimator and the angulated collimators. The system images for the collimators are shown in figure 4.11. In viewing the penetration and scatter in between the line sources, the four images are virtually indistinguishable.

To compare the line sources, the images in figure 4.12 use a different colour scale to accentuate differences in the lines. The intensity along a line varies more for the angulated collimators than for the perfect collimator.

The measured resolutions of the collimators are presented in table 4.9. The FWHM and FWTM increase as the angulations worsen.

Collimator	A0 (mm)	A1 (mm)	A2 (mm)	A4 (mm)
FWHM	9.25 ± 0.01	10.06 ± 0.83	10.93 ± 1.08	11.31 ± 0.59
FWTM	16.86 ± 0.18	18.33 ± 1.51	19.92± 1.97	18.04 ± 0.94

Table 4.9 Measured resolutions of collimators using system images.

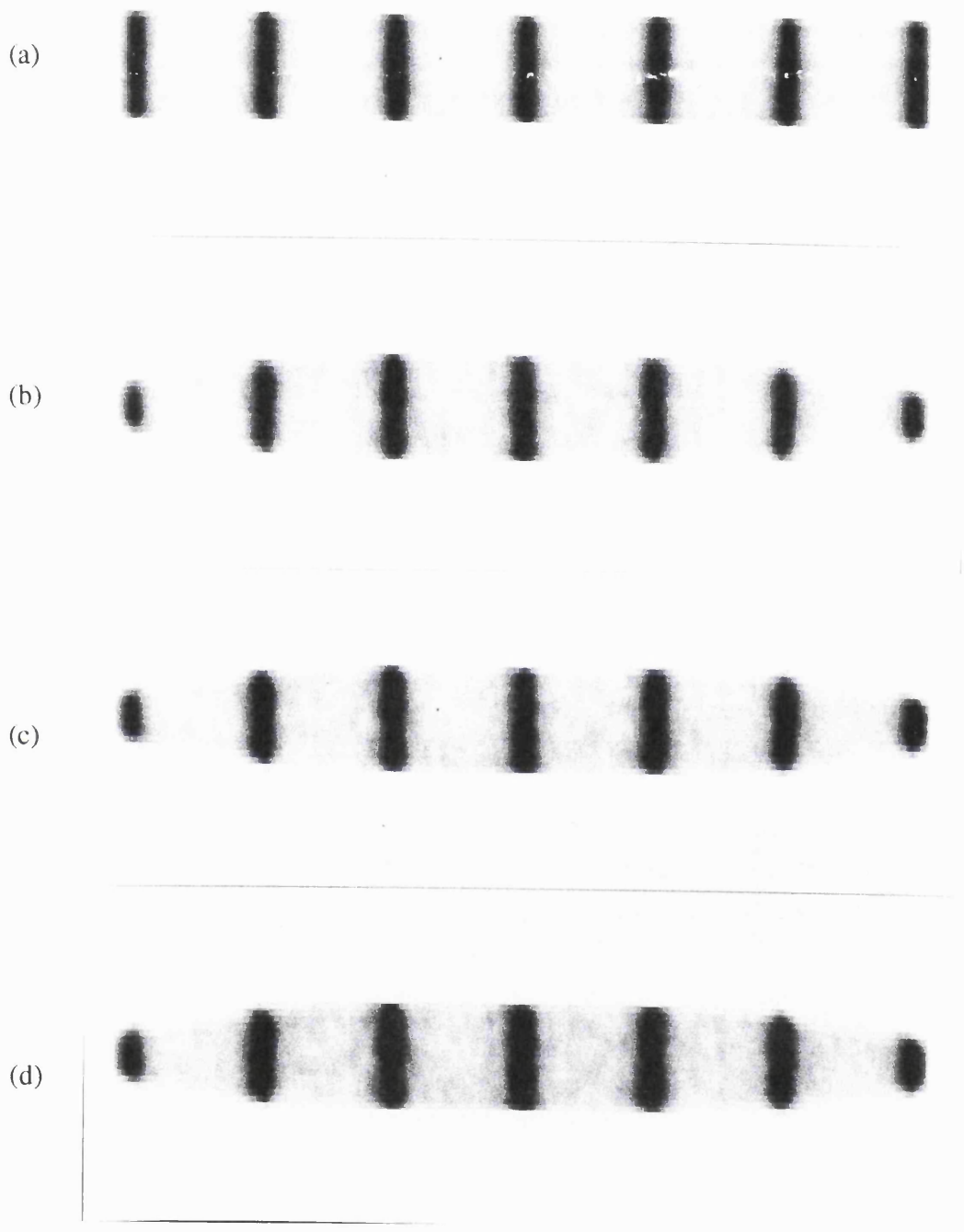

Figure 4.11 System images: (a) A0; (b) A1; (c) A2 and (d) A4.

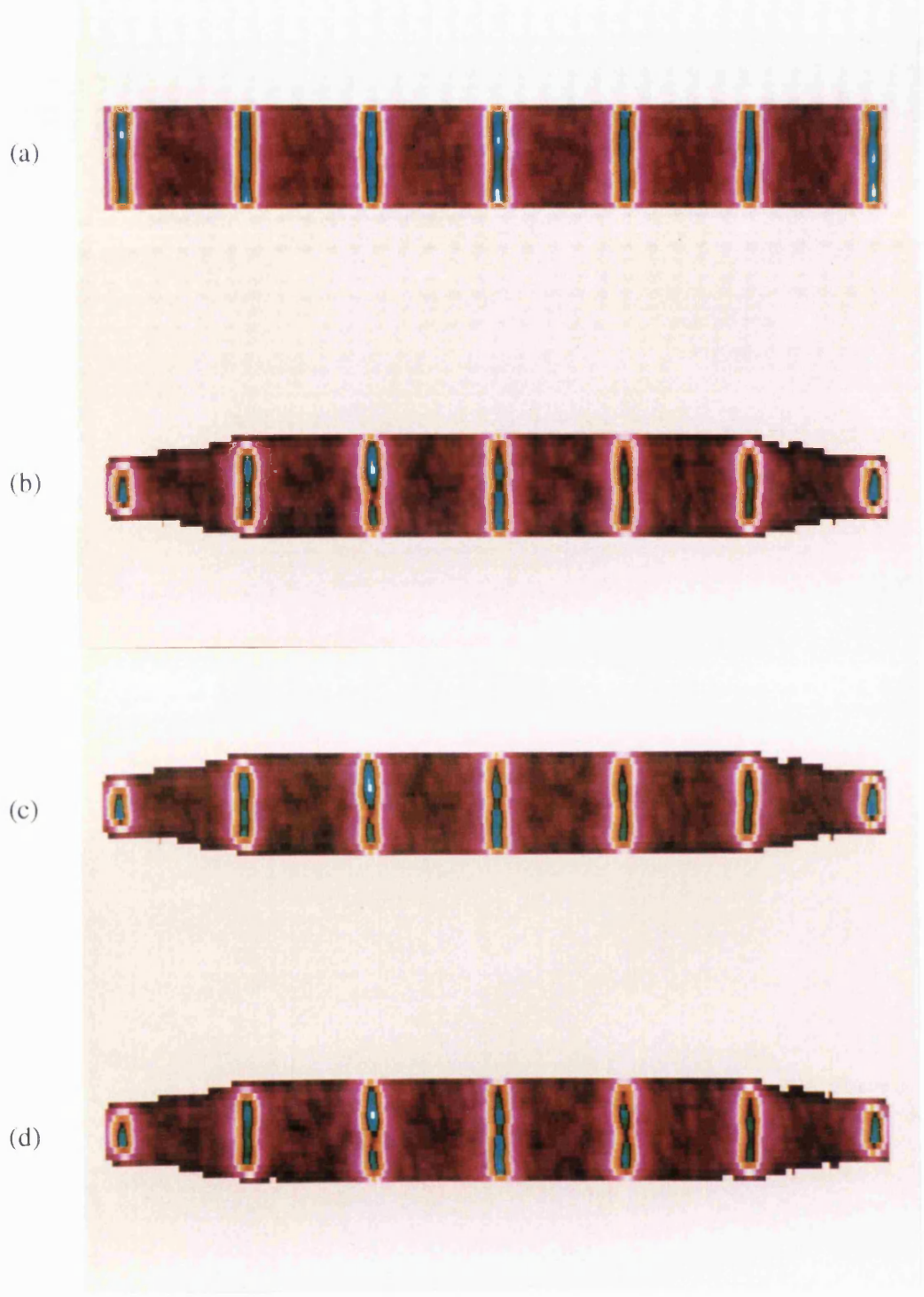

Figure 4.12 System images using alternative colour scale to accentuate differences: (a) A0; (b) A1; (c) A2 and (d) A4.

4.3.3 Discussion on image defects from angulated collimators

Sections 4.3.1 and 4.3.2 showed the effects that angulated collimators had on images. The measured resolutions were seen to worsen as the angulation of the collimator hole increased, as did the linearity of the images. Although the measured resolutions from the images do show a trend as the angulation increases, there is little to differentiate between the widths of the line sources when they are viewed in the image. The only noticeable difference between the perfect image and the angulated images is in the linearity of a line. Here the model of the collimator with the smallest angulation (a width of 1° at 0.01 of the peak value), where 55% of the holes deviate by a maximum of 0.25° from the preferred direction, shows a noticeable degradation in the images of the lines. Thus even in the case of planar imaging it is important that the holes are angulated correctly, since misalignment could lead to artefacts in the image.

4.4 Images from laminated collimators

In this section images of the laminated collimator are compared with those obtained from the simulation of a conventional collimator. The components that make up the image are discussed separately such that the effect that each component has on the final image may be ascertained. Particular attention is paid to the effects of penetration and scatter in the collimator so that the effects of the reduction in lead in the laminated collimator may be determined. The Gaussian fitting routine is used to determine the spatial resolution of the images.

4.4.1 Image from geometric photons not scattered in the object

The geometric component of the collimator response function is dependent only on the hole diameter, shape and length. This should be true also of the image, so that the image of geometric photons obtained using a laminated collimator should, within the limits of statistical error, be identical to that of a conventional collimator of the same dimensions. Figure 4.13 shows the image of geometric photons obtained from (a) a conventional collimator and (b) the laminated structure.

The images, which appear very similar, have resolutions which are the same within the limits of statistical error as shown in table 4.10.

	Conventional collimator resolution (mm)	Laminated collimator resolution (mm)	Difference (mm)
FWHM	7.88 ± 0.11	8.21 ± 0.22	0.33 ± 0.25
FWTM	14.35 ± 0.21	14.96 ± 0.42	0.61 ± 0.46

Table 4.10 Geometric resolutions of conventional and laminated structure.

Figure 4.13 Geometric photon image: (a) Conventional collimator, (b) Laminated collimator.

4.4.2 Image from penetrated photons not scattered in either the collimator or the object

When dealing with the images formed using the conventional collimator it was found that the penetration component was the component that had the greatest effect on the resolution of an image. In dealing with laminated collimators the effect of penetration on the image will be greater due to the poorer absorption properties of the aluminium layers compared with the lead they are replacing.

The comparison between the penetration component of the images for the conventional and laminated collimators is shown in figure 4.14 (a) and (b). While the photons contributing to the penetration component of the conventional collimator (figure 4.14 (a)) are located mainly in pixels under and spreading out from the line sources, in the case of the laminated collimator (figure 4.14 (b)) there appears to be a general background level of penetration as well as the photons under the line sources. This is also seen in one of the profiles of the penetration components of the conventional collimator (figure 4.14 (c)) and of the laminated collimator (figure 4.14 (d)) where the seven lines are seen in both cases, with no penetration in between the lines in the conventional case but a fairly constant background level of penetration in the laminated case. Figures 4.14 (e) and (f) show the summed images of geometric and penetrated photons for the conventional and laminated collimators, respectively. Figures 4.14 (g) and (h) respectively show the image and one of the profiles of the laminated collimator when all counts including and below that

background level are windowed out of the image. The windowed image (g) is similar to the image of the conventional collimator (e).

(a)

(b)

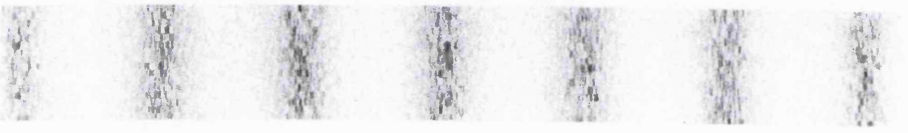

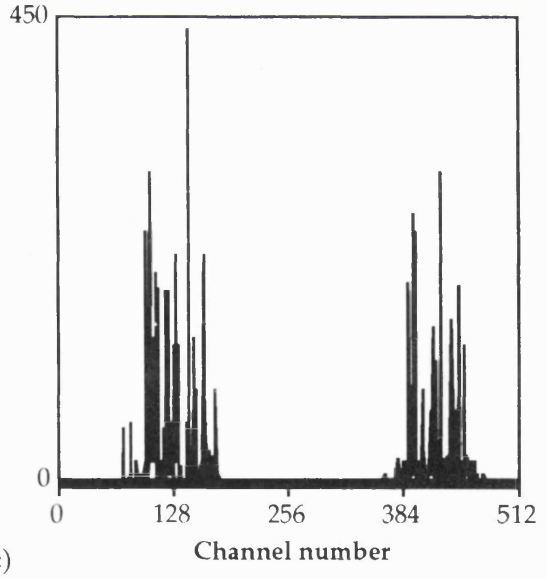

(c)

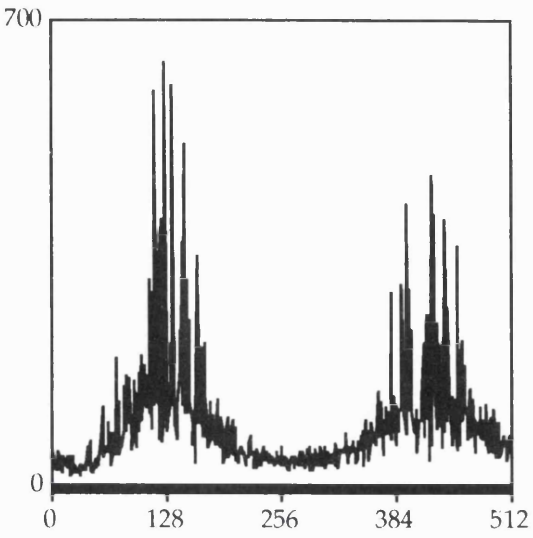

(d)

(e)

(f)

(g)

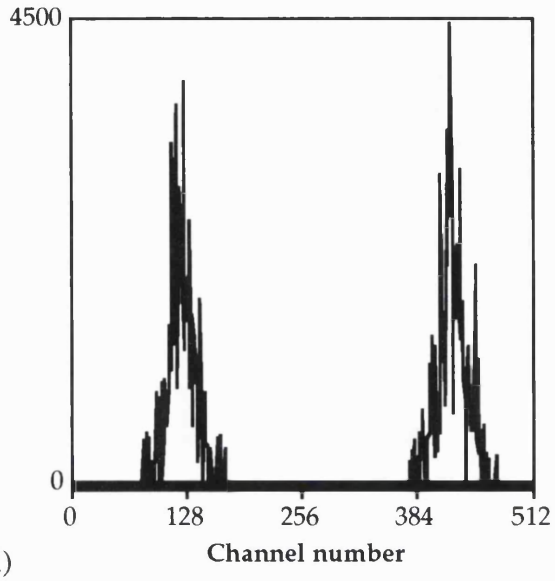

(h)

Figure 4.14 Effects of penetrated photons on images: (a) and (b) Penetrated component of conventional and laminated collimator images, respectively; (c) and (d) Profiles of penetration component of conventional and laminated collimators, respectively; (e) and (f) Image of geometric and penetrated photons from conventional and laminated collimators, respectively; (g) and (h) Image and profile from laminated collimator when count window has been set.

The mean resolutions from the geometric and penetrated photons for the two collimators, given in table 4.11, show a 14% increase in the width of the line source when the laminated collimator is used.

	Conventional collimator resolution (mm)	Laminated collimator resolution (mm)	Actual increase (mm)
FWHM	7.99 ± 0.15	9.13 ± 0.41	1.15 ± 0.44
FWTM	14.55 ± 0.28	16.64 ± 0.75	2.09 ± 0.80

Table 4.11 Mean resolutions of conventional and laminated collimators using only geometric and penetrated photons.

4.4.3 Image from photons not scattered in the object but scattered in the collimator

The scatter fractions of the images for (a) the conventional and (b) the laminated collimator are shown in figure 4.15, while (c) and (d) show the total images for these collimators. The scatter fraction for the conventional collimator shows some photons evident under the positions of the line sources but not elsewhere. In the case of the laminated collimator there seems to be a fairly uniform 'background' layer of scattered photons with seven faint, broad lines superimposed corresponding to the line sources. When the images of the summed geometric, penetrated and scattered components of photons which were unscattered in the source are considered, the conventional collimator (c) shows definite lines

with very little background but while the definite lines are still evident in the laminated collimator image (d) there is a fairly uniform background count over the image.

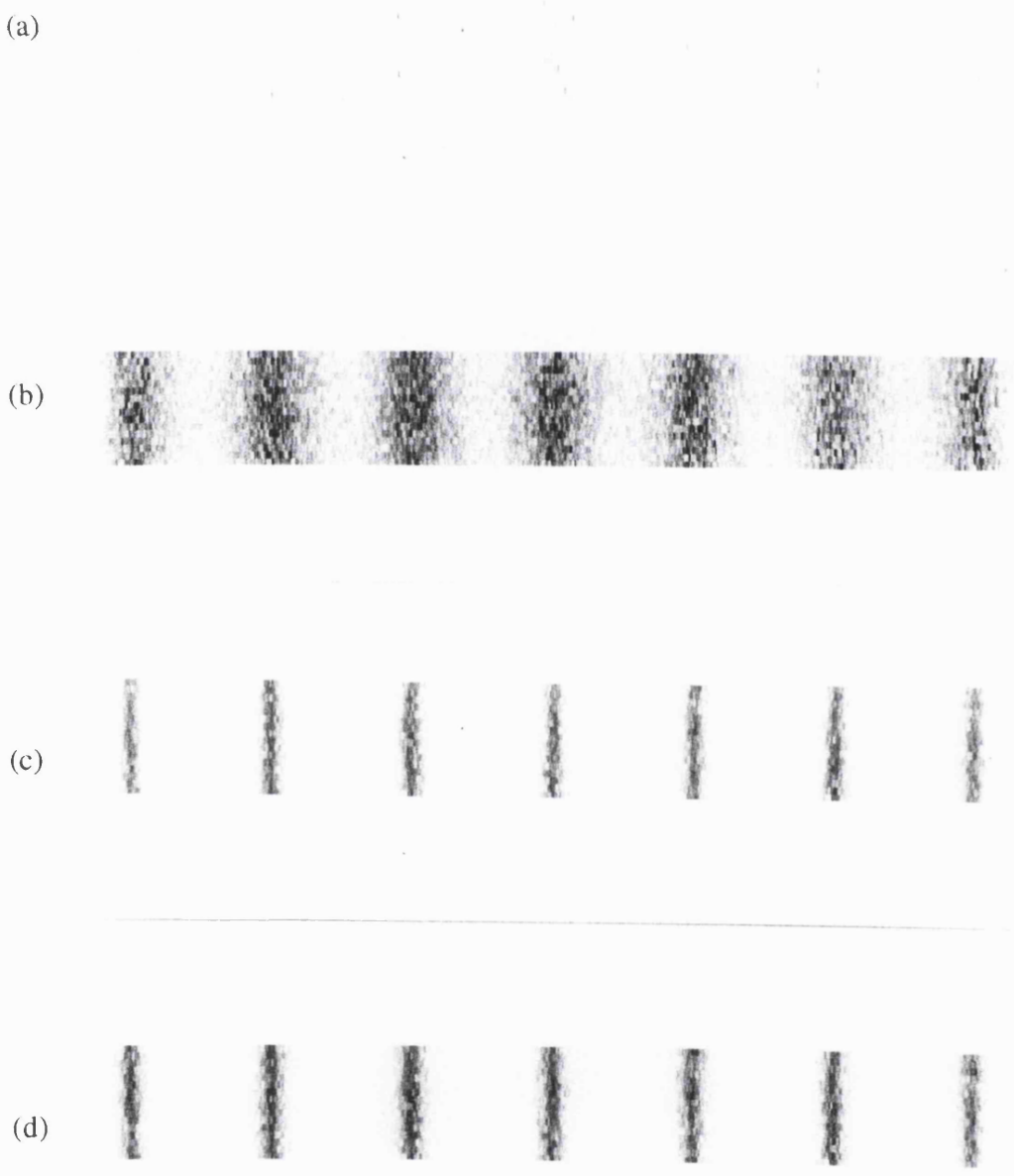

Figure 4.15 Effect of scatter in the collimator on images: (a) and (b) Scatter fractions of images from conventional and laminated collimators, respectively; (c) and (d) Images of geometric, penetrated and scattered photons from conventional and laminated collimators, respectively.

(a)

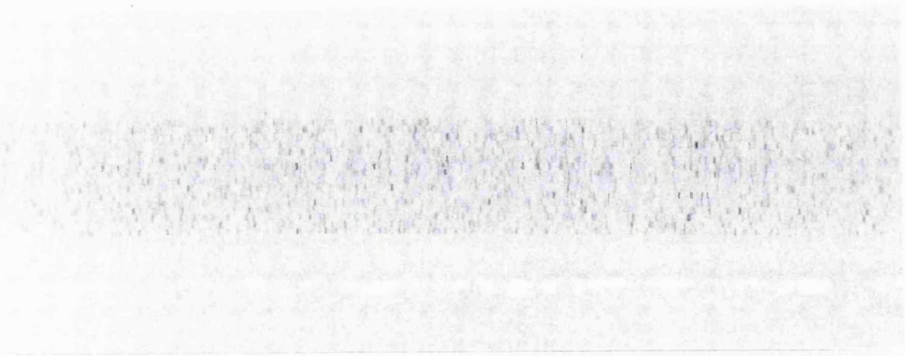

(b)

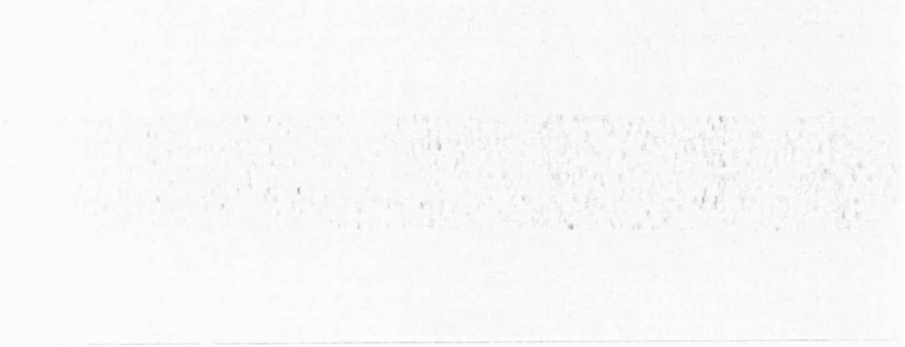

(c)

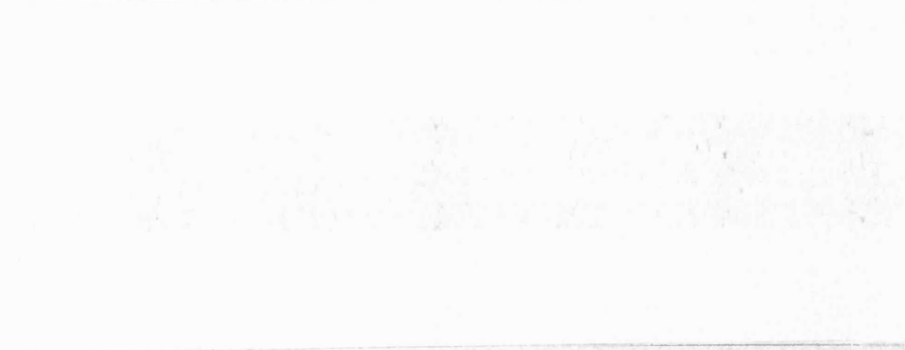

(d)

Figure 4.16 The contribution of photon scatter in the object to the final image for the energy ranges: (a) $125 \leq E < 130$ keV, (b) $130 \leq E < 135$ keV, (c) $135 \leq E < 140$ keV and (d) $E = 140$ keV.

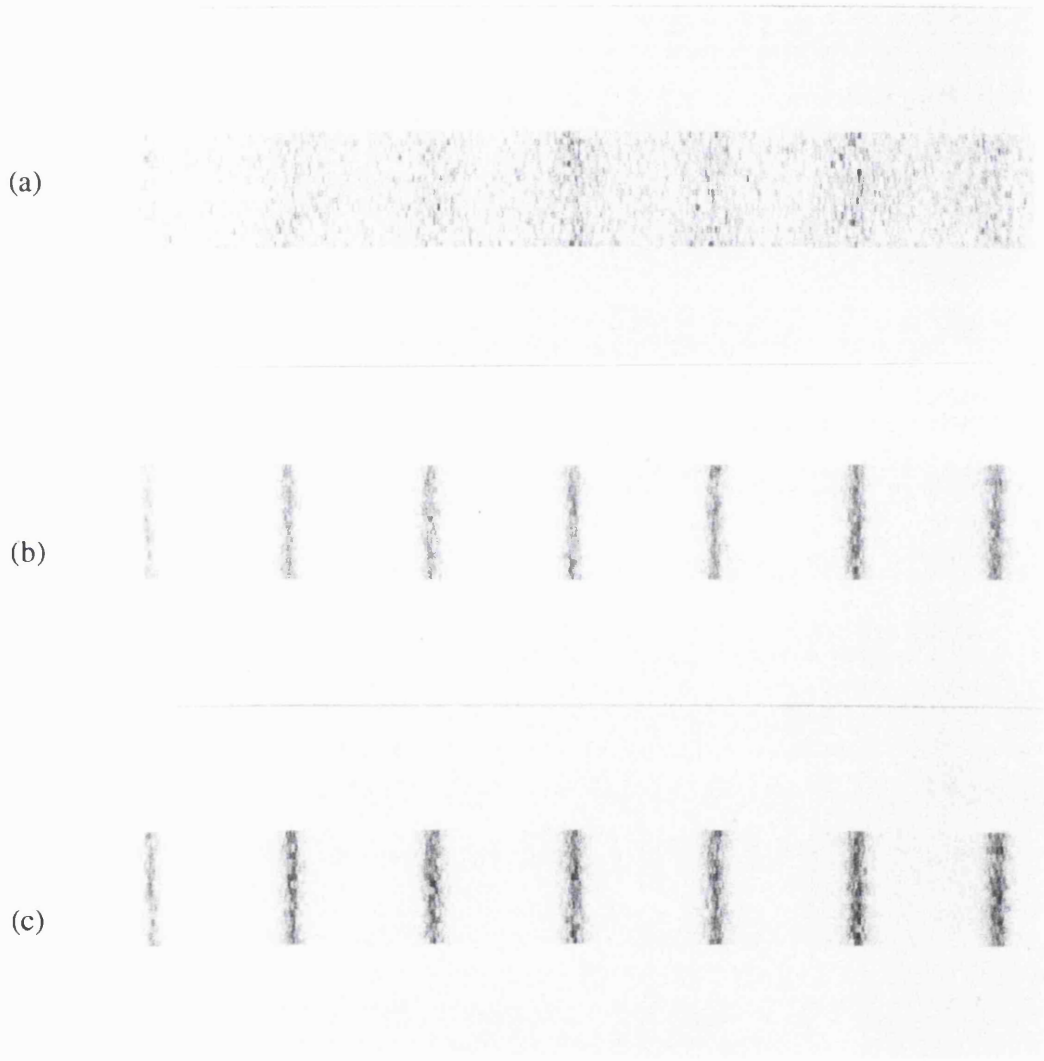

Figure 4.17 The overall effect of photon scatter in the object to the final image: (a) Image from laminated collimator of photons at crystal which have undergone scatter in source, (b) and (c) Images of all photons at crystal for laminated and conventional collimators, respectively.

4.4.4 Image containing all photons (not convolved with intrinsic resolution)

The contribution to the final image of photons scattered in the phantom for the energy ranges (a) $125 \leq E < 130$ keV, (b) $130 \leq E < 135$ keV, (c) $135 \leq E < 140$ keV and (d) $E = 140$ keV for the laminated collimator is shown in figure 4.16. For the three lower ranges (a), (b) and (c), the images have a fairly uniform distribution of photons throughout the image. Only in (d) are the line sources visible where they are very broad with a width of approximately 3 cm.

The overall effect on the image of scatter within the phantom is shown by the images of figure 4.17, where (a) shows the image using the laminated collimator of photons reaching the crystal which have been scattered in the source (i.e. images (a) to (d) of figure 4.16 summed), (b) the image of all photons which reach the crystal when the laminated collimator is used and (c) is the same as (b) but using the conventional collimator. Seven broad lines can only just be seen in (a) above the background level of scatter. The total images for the two collimators are very similar with the background level of scatter appearing more uniform for the laminated collimator (b) than for the conventional collimator (c).

The fitting of a Gaussian to each of these lines provides the overall resolutions given in table 4.12.

	Conventional collimator resolution (mm)	Laminated collimator resolution (mm)
FWHM	8.74 ± 0.06	7.91 ± 0.07
FWTM	15.94 ± 0.01	14.42 ± 0.01

Table 4.12 Resolutions of unconvolved total image for conventional and laminated collimators.

From the fit the values of the FWHM and FWTM appear to be better for the laminated collimator than for the conventional collimator although for all previous stages of the image the reverse was the case. This can be explained by looking at the level of background noise images of figure 4.17 where the conventional collimator appears more noisy than the laminated collimator. A line segment from one of the profiles of each of the total images is shown in figure 4.18 together with the fit to that segment. Due to the amount of noise present in the line segment in the conventional image the Gaussian fit is wider than for the corresponding line of the laminated image.

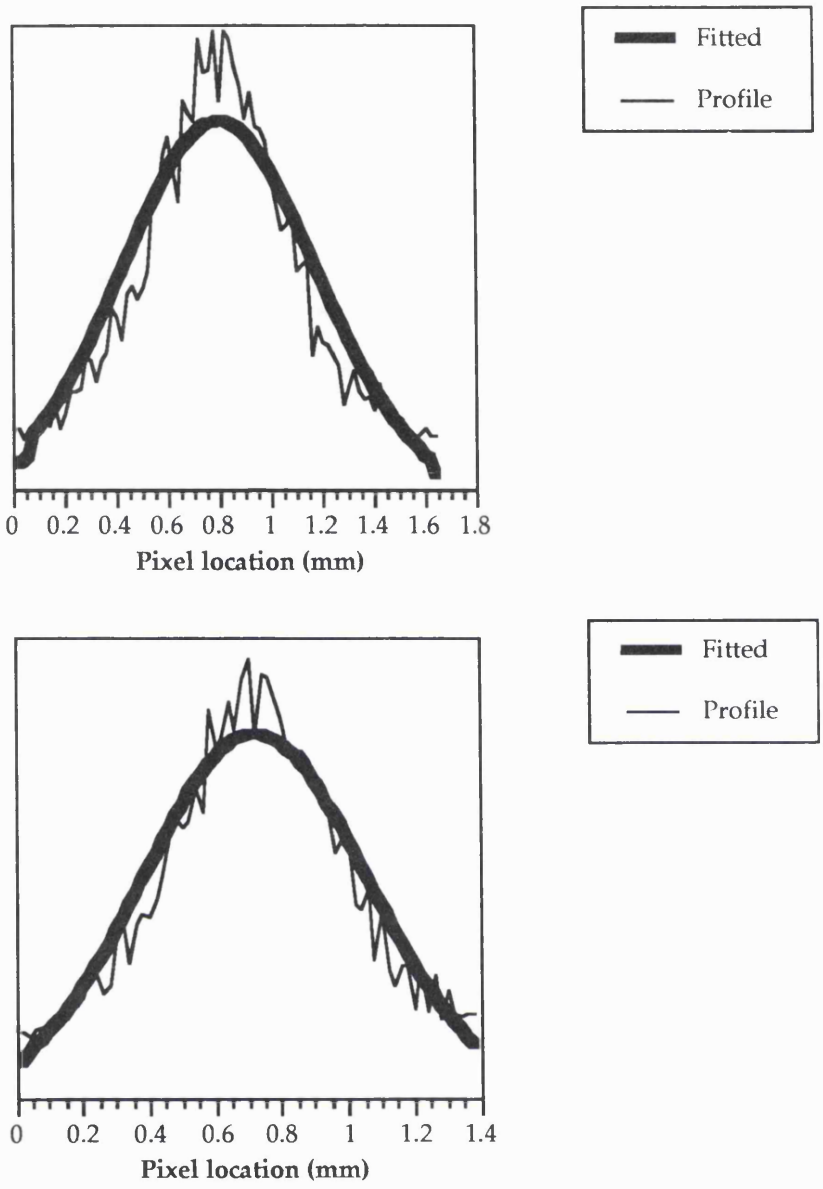

Figure 4.18 Line segments from total images of (a) Conventional collimator and (b) Laminated collimator.

4.4.5 System image from laminated collimator

When the results shown in section 4.4.4 are convolved with the intrinsic resolution of the camera the images shown in figure 4.19 are obtained. While the seven lines are clearly seen in both (a) the conventional image and (b) the laminated image, the regions in between the lines are different for each collimator.

(a)

(b)

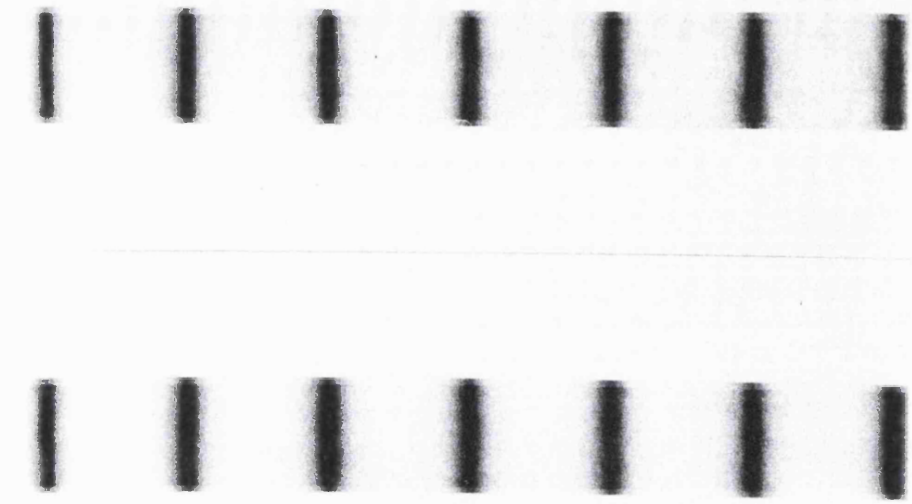

Figure 4.19 System images for (a) Conventional collimator and (b) Laminated collimator.

(a)

(b)

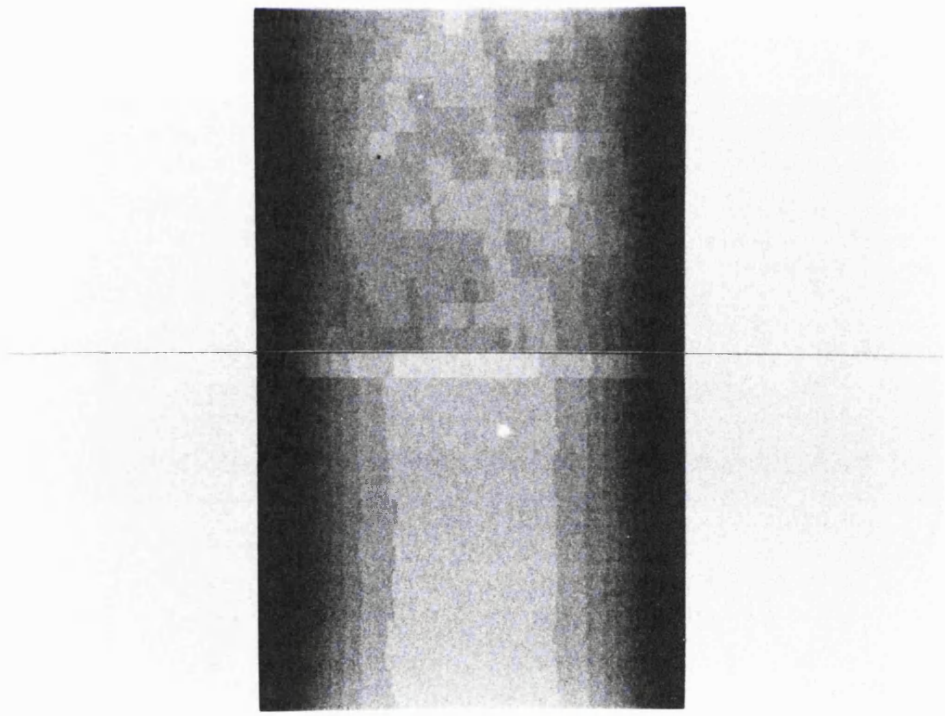

Figure 4.20 Zoomed image of the region between two of the lines for (a) Conventional collimator and (b) Laminated collimator.

Figure 4.20 shows a zoomed image of the region between two of the lines for both collimators. In the case of the conventional collimator a mottled effect exists while for the laminated collimator the intensity is symmetric between the lines falling down to a plateau before rising again back up to the line.

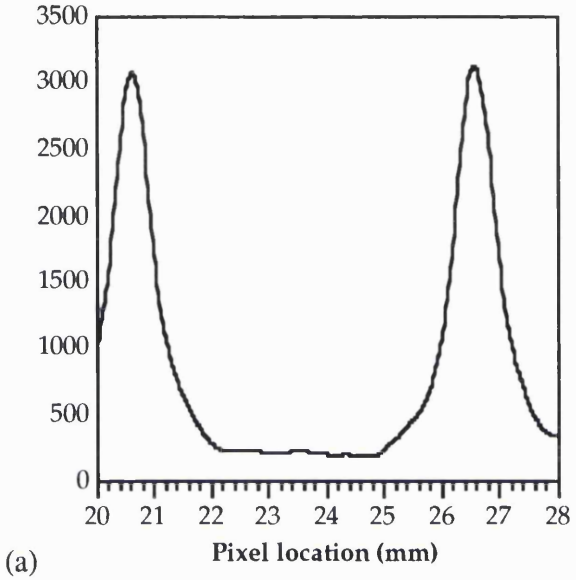

(a)

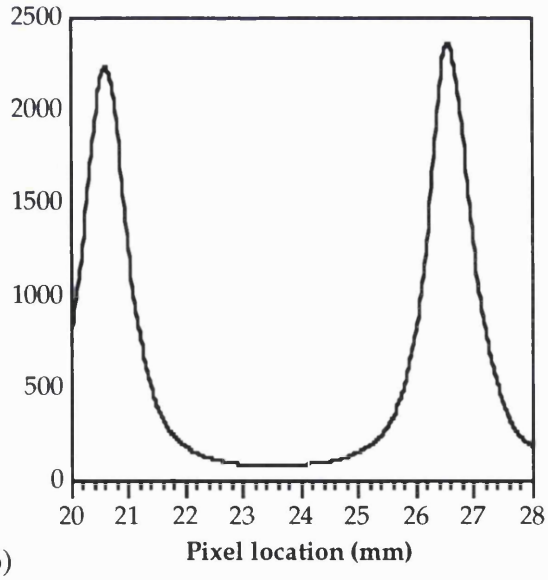

(b)

Figure 4.21 Profiles of system images for (a) Conventional collimator and (b) Laminated collimator.

When profiles of the images are plotted (figure 4.21) they appear very similar apart from the region in between the peaks where the profile for the laminated collimator (figure 4.21 (b)) is much smoother than that of the conventional collimator (a).

The fitted values of the FWHM and FWTM for both the conventional and laminated collimator are presented in table 4.13. Within the limits of statistical error the resolutions of the two collimators are almost identical.

	Conventional collimator resolution (mm)	**Laminated collimator resolution (mm)**	**Increase in width (mm)**	**% width increase**
FWHM	9.19 ± 0.37	9.29 ± 0.24	0.10 ± 0.44	1.08 ± 0.05
FWTM	16.76 ± 0.67	16.94 ± 0.44	0.18 ± 0.80	1.08 ± 0.05

Table 4.13 Resolutions of system image of conventional and laminated collimators.

When a window is set to exclude pixel counts below a certain threshold the images given in figure 4.22 are produced. These images appear very similar for both the laminated and conventional structures and suggest that setting a count threshold might remove some of the effects of penetration and scatter.

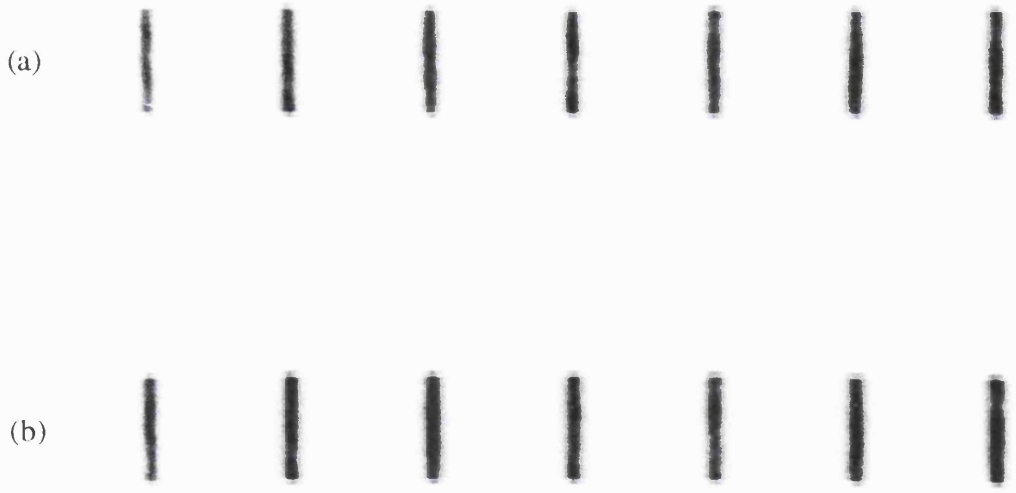

Figure 4.22 System images of (a) Conventional collimator and (b) Laminated collimator when a count threshold has been set.

4.4.6 Discussion on the use of a laminated collimator structure for gamma camera imaging

The original purpose in devising a laminated collimator structure was to produce a lighter-weight collimator which was less prone to damage than a conventional collimator. The images presented in sections 4.4.1 to 4.4.5 indicate that the laminated collimator compares very favourably with the conventional lead collimator in terms of spatial resolution. While there is increased penetration in the laminated collimator due to the decreased thickness of lead, this appears mainly as a fairly uniform background level which does not greatly affect the resolution of the image at FWHM and FWTM and can be removed by only selecting counts above a certain threshold. When the system image is considered (figure 4.17) the mean resolution (FWHM) of the laminated collimator image at 9.29 ± 0.24 mm is very similar to that of the conventional collimator at 9.19 ± 0.37 mm. If the weight of the collimator was not considered to be a problem then more dense materials could be used than aluminium which would have better absorption properties leading to a decrease in the penetration and scatter detected, and would still improve the rigidity over that of a conventional lead collimator.

4.5 Images from a uranium collimator of conventional dimensions

The uranium collimator modelled in this section will have identical dimensions to the conventional lead collimator, to determine what effect the uranium has on the degree of penetration and scatter in the final image.

4.5.1 Image from geometric photons not scattered in the object

As discussed previously, the geometric image from two collimators of identical dimensions should be the same. This is indeed seen to be the case in figure 4.23 where the geometric images of the lead and the uranium collimators are presented.

The fitted Gaussians produce values for the resolutions which are identical within statistical limits (table 4.14).

	Conventional collimator resolution (mm)	Uranium collimator resolution (mm)
FWHM	7.88 ± 0.11	8.08 ± 0.16
FWTM	14.35 ± 0.20	14.72 ± 0.29

Table 4.14 Fitted values for geometric resolutions of conventional and uranium collimator.

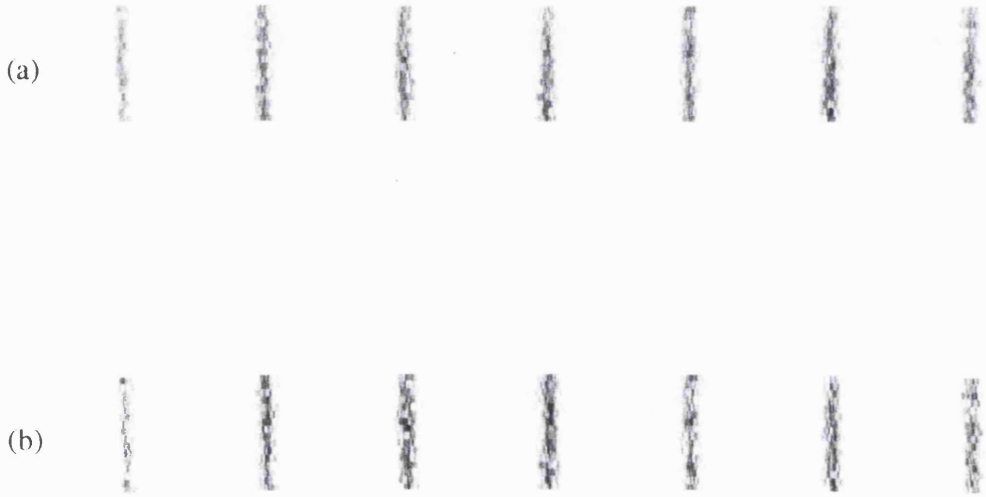

Figure 4.23 Geometric image: (a) Conventional collimator, (b) Uranium collimator.

4.5.2 Image from penetrated photons not scattered in either the collimator or the object

Uranium was chosen as an alternative collimator material due to its high absorption coefficient, meaning that fewer penetrated photons would contribute to an image. Images of penetrated photons are shown in figure 4.24 (a) and (b) for the conventional collimator and the uranium collimator, respectively, of the same dimensions.

The penetrated image using the uranium collimator has fewer photons than the conventional lead collimator. The combined images of primary and penetrated photons are shown in figures 4.24 (c) and (d) for the lead and uranium collimators respectively. The two images are very similar in appearance, the lines appearing of similar width. The percentage of penetrated photons in the uranium image is 1.67% compared with 4.02% in the conventional image. When the measured widths of the resolutions of the geometric images are compared with the summed geometric and penetrated images, there is an increase of only 0.24 ± 2.72 % for the uranium collimator while the conventional lead collimator has an increase of 1.27 ± 2.37 % in the width. Therefore although there is a reduction in the number of penetrated photons in the case of the uranium collimator, this appears as only a very small improvement in the resolution.

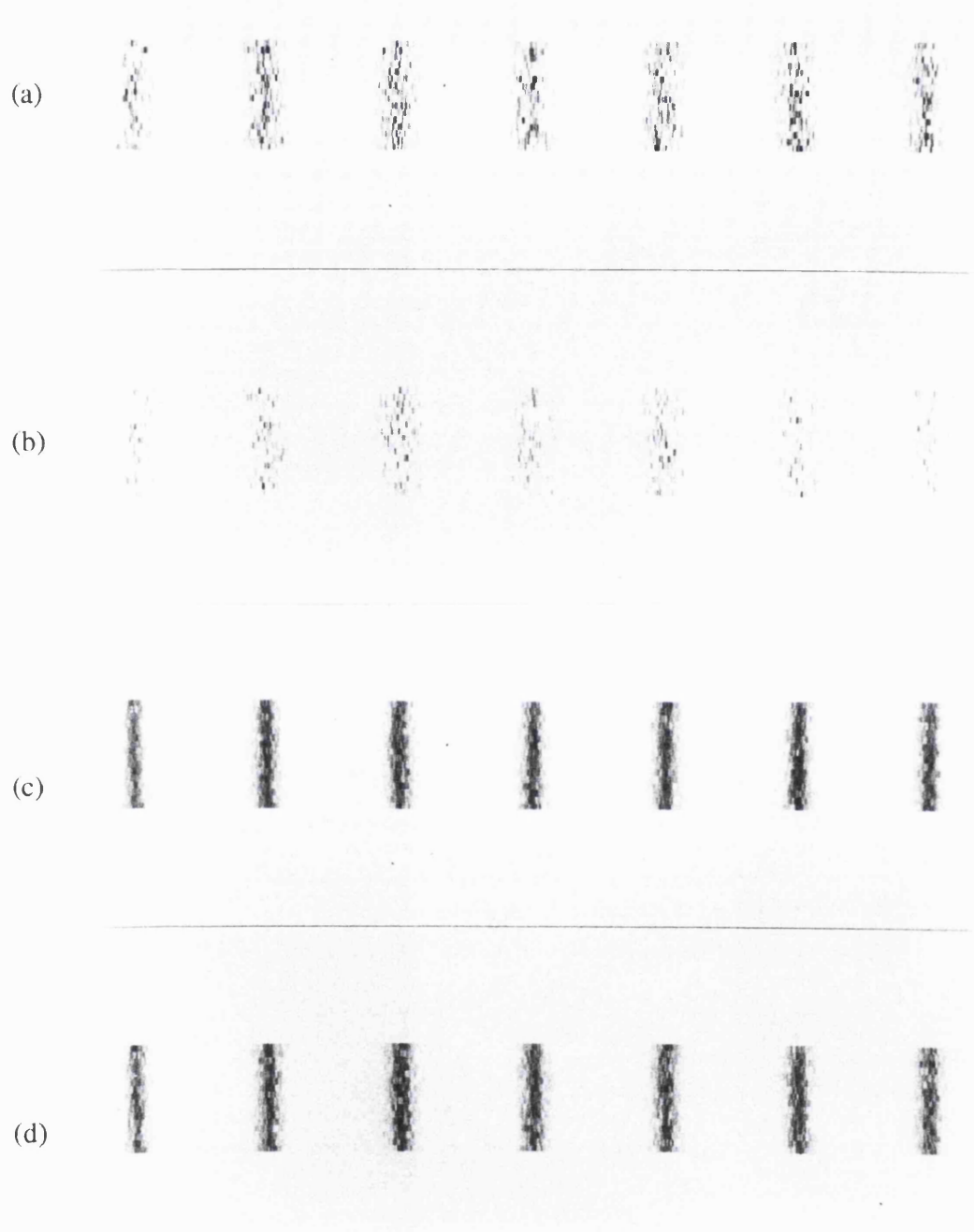

Figure 4.24 Effect of penetration on image: (a) and (b) Penetrated photons at crystal from conventional and uranium collimators, respectively; (c) and (d) Geometric and penetrated photons at crystal from conventional and uranium collimators, respectively.

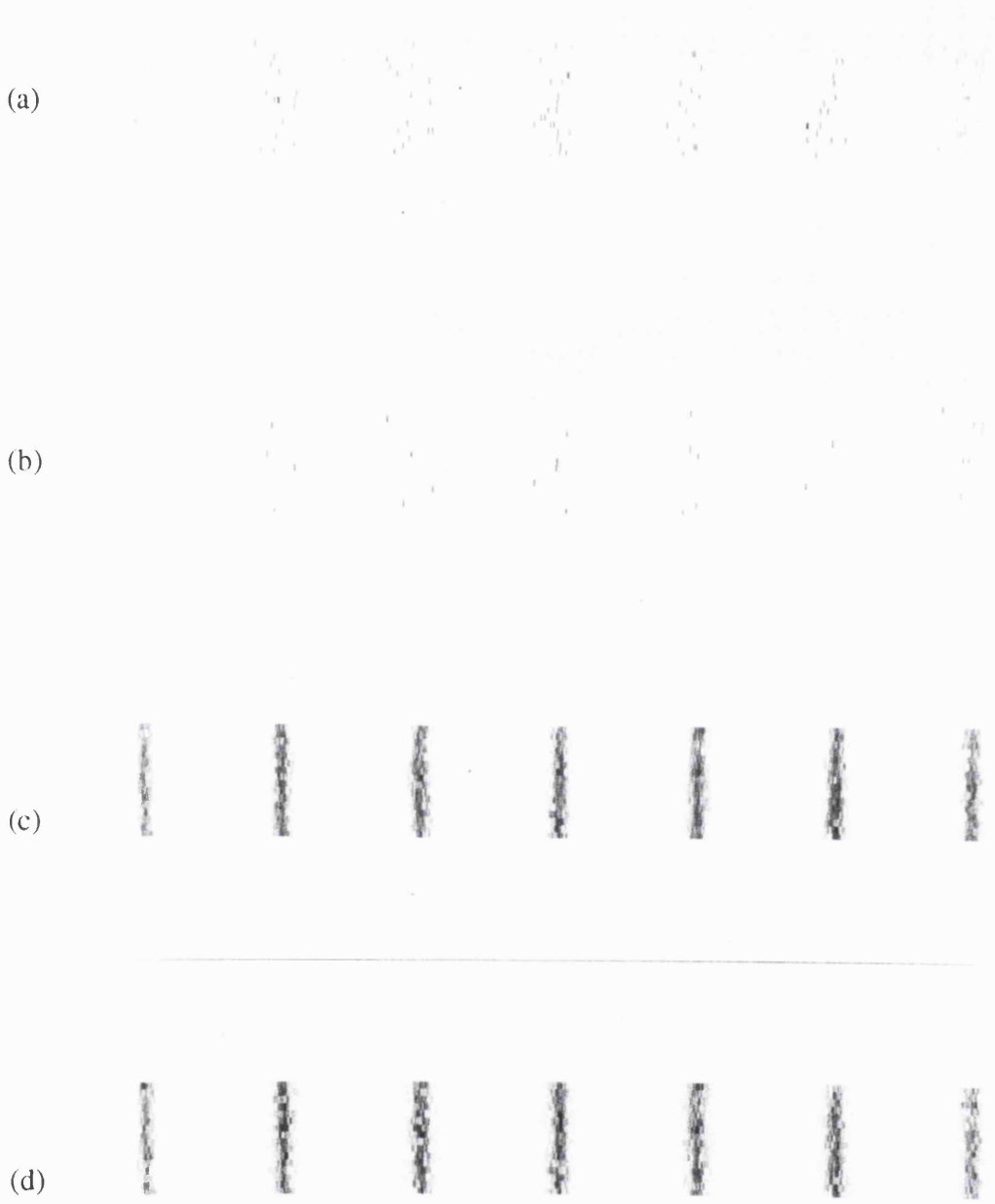

Figure 4.25 Effects of collimator scatter on images: (a) and (b) Scattered photons at crystal from conventional and uranium collimators, respectively; (c) and (d) Geometric, penetrated and scattered photons at crystal for conventional and uranium collimators, respectively.

4.5.3 Image from photons not scattered in the object but scattered in the collimator

In addition to expecting a smaller degree of penetration, fewer scattered photons are expected to be detected when the uranium collimator is used than when a lead collimator is used. This is seen to be the case when the images of the scattered photons are viewed (figure 4.25 (a) and (b)). The addition of so few photons to the image cannot be expected to alter the image significantly as was the case for the conventional lead collimator where there was a negligible increase in the width of the lines. Figure 4.25 (c) indicates that the inclusion of collimator scatter in the image from the uranium collimator does not affect the image, while (d) shows the corresponding image for the conventional lead collimator.

4.5.4 Discussion on the use of uranium in collimators of conventional dimensions

Uranium was selected as a possible improvement to lead as a material for gamma camera collimators due to its improved absorption properties. From the response function obtained for a uranium collimator of conventional dimensions, its main advantage appeared to be in the reduction in penetration in the tails of the response. From analysis of the images obtained of the line source phantom using the uranium collimator, while fewer penetrated photons are seen to contribute to the image, this does not constitute an overwhelming improvement in the resolution of the image.

In order to justify the use of a material such as uranium in a collimator it would be necessary to observe a significant improvement in either the resolution or the efficiency. Since no great improvement in the resolution has been obtained by the use of a uranium collimator of conventional dimensions, the following section will consider whether the efficiency of the collimator can be improved, without suffering a loss in the spatial resolution, by using a uranium collimator with narrower septa.

4.6 Images from a uranium collimator with narrow septa

Analysis of the response functions of uranium collimators with septal thicknesses varying between 0.10 mm and 0.24 mm indicated that a narrow septal thickness of 0.10 mm produced resolution which was comparable with that from a collimator of 0.24 mm septal thickness. Since a smaller septal thickness will produce a more efficient collimator while not affecting the spatial geometric resolution, images have been generated using a uranium collimator with a septal thickness of 0.10 mm and these images are analysed in the following sections.

4.6.1 Image from geometric photons not scattered in the object

Once again, since the hole size in the collimator is the same as that of all other collimators modelled, the geometric resolution should not change when a narrow septa uranium collimator is used. The geometric photon image obtained for this narrow septa collimator is compared with that of the conventional lead collimator in figure 4.26 and the resolutions obtained from the Gaussian fitting routine are given in table 4.15. Within the limits of statistical error the resolutions of the two collimators are identical.

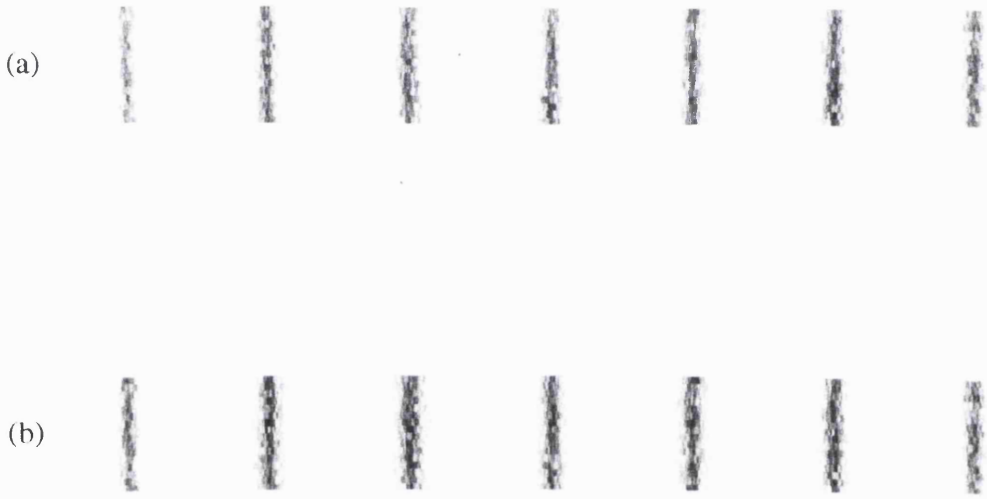

Figure 4.26 Geometric images: (a) Conventional lead collimator and (b) Narrow septa uranium collimator.

	Conventional lead collimator resolution (mm)	Narrow septa uranium collimator resolution (mm)
FWHM	7.88 ± 0.11	7.93 ± 0.13
FWTM	14.35 ± 0.20	14.45 ± 0.24

Table 4.15 Geometric resolutions for both conventional lead and narrow septa uranium collimators.

4.6.2 Image from penetrated photons not scattered in either the collimator or the object

The purpose of using uranium as a collimator material was that its absorption properties would mean that narrower septa could be used while still maintaining a similar degree of penetration in the image. In figure 4.27, which shows the image of the penetrated photons, there are fewer photons in the narrow septa uranium case (b) than the image of the conventional collimator (a).

Figure 4.27 Effect of penetration on image: (a) Conventional collimator and (b) Narrow septa uranium collimator.

When the penetrated photon image is added to the geometric image the images seen in figure 4.28 are obtained. The two images are virtually indistinguishable. The resolutions obtained from the images in figure 4.28 are also the same within statistical limits (table 4.16).

	Conventional lead collimator resolution (mm)	Narrow septa uranium collimator resolution (mm)
FWHM	7.98 ± 0.15	8.09 ± 0.16
FWTM	14.54 ± 0.28	14.76 ± 0.28

Table 4.16 Resolutions for summed geometric and penetrated photons of both conventional lead and narrow septa uranium collimators.

The percentage of penetrated photons in the image obtained using the uranium collimator is 1.75%, which is lower than the 4.02% in the conventional collimator image of geometric and penetrated photons. The addition of the penetrated photons to the image therefore shows that this septal thickness of 0.10 mm of uranium is sufficient to obtain a image of comparable quality to that of the conventional lead collimator of septal thickness 0.24 mm while achieving a higher efficiency due to the decrease in septal thickness.

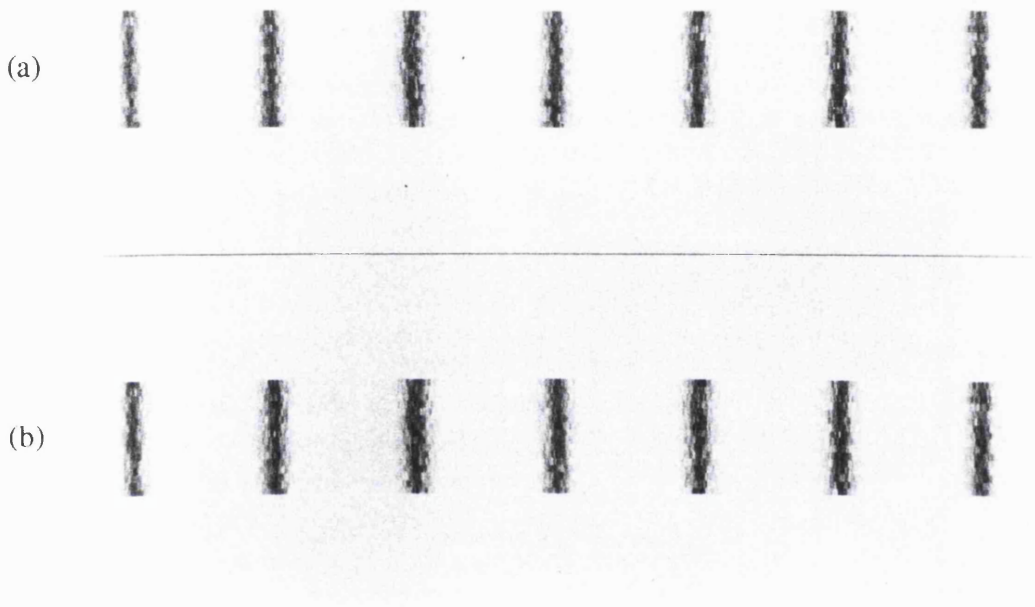

Figure 4.28 Image of geometric and penetrated photons: (a) Conventional collimator and (b) Narrow septa uranium collimator.

4.6.3 Image containing photons not scattered in the object but scattered in the collimator

Images of the scattered photons are presented in figure 4.29 for the conventional and narrow septa uranium collimator. Fewer scattered photons are present for the uranium collimator.

When these images are added to the image of the geometric and penetrated photons the images are again virtually indistinguishable (figure 4.30). Only 0.06% of the photons in the image of the uranium collimator in figure 4.30 are scattered photons.

(a)

(b)

Figure 4.29 Contribution of collimator scatter to image: (a) Conventional collimator, (b) Narrow septa uranium collimator.

(a)

(b)

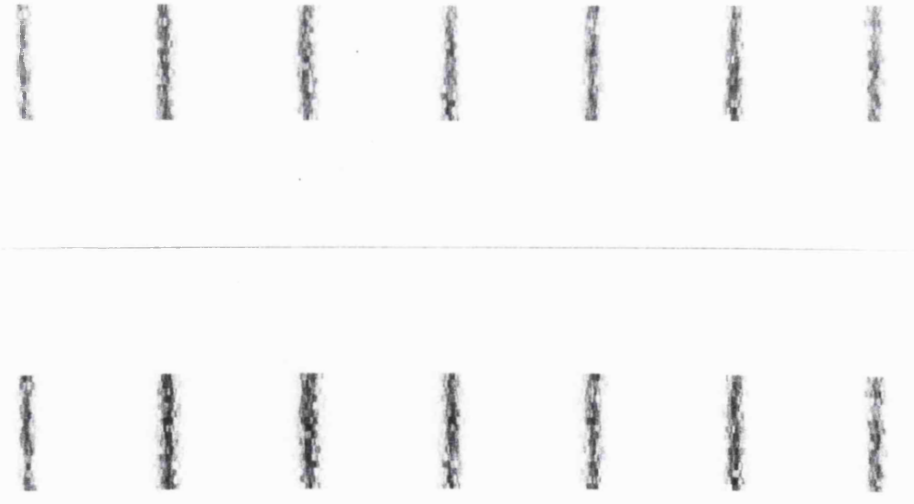

Figure 4.30 Images of geometric, penetrated and scattered photons: (a) Conventional collimator, (b) Narrow septa uranium collimator.

4.6.4 Image containing all photons (not convolved with intrinsic resolution)

The addition of photons scattered in the source to the image gives the results shown in figure 4.31. As is expected from the previous images little difference exists between the images using the narrow septa uranium collimator and the conventional lead collimator.

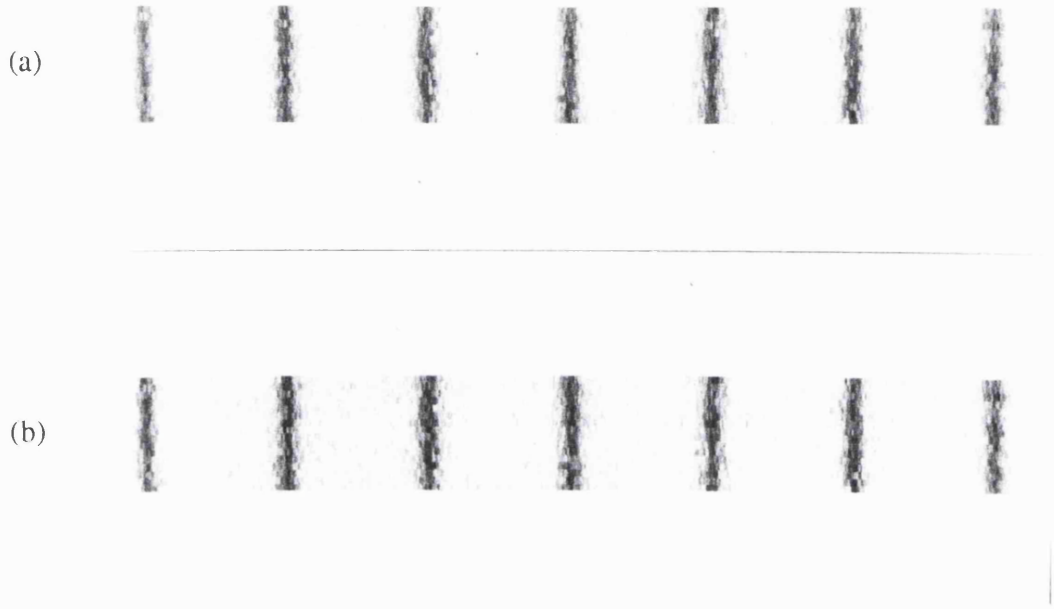

Figure 4.31 Images of all photons: (a) Conventional collimator, (b) Narrow septa uranium collimator.

4.6.5 System image from narrow septa uranium collimator

The convolution of the data in figure 4.31 with the intrinsic resolution of the system produces the images shown in figure 4.32. The image of the narrow septa uranium collimator (b) appears as good as the conventional lead collimator image (a) which is confirmed by the resolutions given in table 4.17, where the resolution of the uranium collimator is slightly better than the conventional lead collimator.

	Conventional lead collimator resolution (mm)	Narrow septa uranium collimator resolution (mm)
FWHM	9.25 ± 0.01	8.76 ± 0.16
FWTM	16.86 ± 0.18	15.98 ± 0.29

Table 4.17 Resolution values for system images of conventional lead and narrow septa uranium collimators.

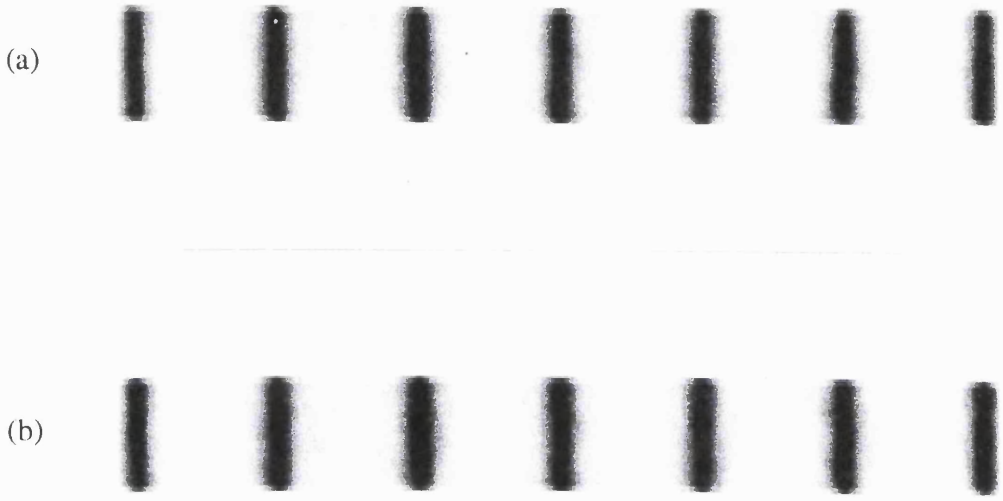

Figure 4.32 System images: (a) Conventional collimator, (b) Narrow septa uranium collimator.

Having achieved a resolution which is comparable to a conventional collimator, the main advantage of using narrower septa is that the number of holes per unit area is increased, resulting in an improved efficiency. As a measurement of the improved efficiency, the number of photons recorded in the average response functions of the narrow septa uranium collimator and the conventional lead collimator was determined and multiplied by the number of unit cells in the collimator. In this way the narrow septa uranium collimator had an efficiency which was approximately 20% higher than the conventional lead collimator.

4.6.6 Discussion on the use of narrower septa uranium collimators

The purpose of investigating uranium as a possible material for gamma camera collimators was to obtain an equally good spatial resolution while improving the efficiency. This improvement in efficiency is due to the increase in the number of holes per unit area which results from the decrease in septal thickness. The results obtained from the narrow septa collimator show that fewer photons are detected that have penetrated the septa either with or without undergoing scatter. The overall resolution obtained from this narrow septa collimator shows a slight improvement over the conventional collimator resolution, probably due to the decrease in detected penetrated and scattered photons.

4.6 Depleted uranium energy spectrum

A major concern with the use of uranium for a collimator material is its activity. This concern is more for the effect of the activity on images rather than the danger to patient or hospital staff, since the depleted uranium, if adequately shielded with aluminium to absorb alpha radiation does not constitute a hazard. As an indication of the activity a lump of depleted uranium 3/4'' thick was counted in a whole body counter. The uranium was covered by a sheet of aluminium to filter out the β radiation. The main peaks obtained were at 63, 92, 185.6, 766 and 1001 keV, the approximate number of counts recorded in a 10 minute period being 50 000, 150 000, 40 000, 10 000 and 20 000, respectively. Of these, only the three higher energies would pose a possible problem to gamma camera imaging with a Tc-99m isotope with a 20% energy window centred on the 140 keV peak isotope energy. Before constructing a collimator from depleted uranium it would be necessary to image a lump of depleted uranium on a gamma camera to determine the effect of the natural activity on the image. If the number of counts recorded from the depleted uranium was thought to be sufficiently low as not to adversely effect any image, then from the images obtained in this chapter, narrow septa uranium collimators offer images of comparable resolution and higher efficiency than a conventional lead collimator.

4.7 Conclusions on alternative collimators

The aim of this chapter has been to evaluate collimators of different designs, materials and accuracy. Three collimators with different degrees of random angulations were modelled and their images assessed. It was found that the measured resolutions from a line source image worsened as the angulation increased, although this effect was not evident when the images were viewed. The degradation of linearity with increase in angulation was a more significant factor. This effect was visible in images, leading to a conclusion that the correct angulation of holes is vital. Hole angulations should not deviate by more than 0.25° from their correct angulation.

To produce a collimator that was more robust than the conventional lead collimator, a laminated collimator structure was proposed with layer thicknesses of 0.01 cm. The images obtained from the laminated collimator structure compared favourably with those of the conventional lead collimator, the resolutions being identical within statistical limits. The advantage of using such narrow layers is that the hole structure could be pressed out mechanically, reducing the likelihood of hole angulation.

In considering alternative material collimators, depleted uranium was determined to be the optimum material due to its superior absorption properties. The only drawback of using uranium in a collimator is its natural radioactivity. Measurements made in a whole body counter on a lump of depleted uranium suggest that it would however be viable for use in collimators. The main advantage to using uranium as an alternative material is that more

efficient collimators can be constructed without compromising resolution, by using the same hole size as a conventional lead collimator but reducing the septal thickness. A thickness of 0.10 mm, which is less than half the septal thickness of a conventional lead collimator, gave similar values for the resolution and improved efficiency over that of the conventional collimator.

Of the two alternative types of collimator modelled in this chapter, the most promising would appear to be the narrow septa uranium collimator. The main advantages of the laminated collimator are its strength and reduction in mass, however, while the image quality obtained is comparable to a conventional lead collimator there is no improvement to image quality. The increased efficiency of the uranium collimator, obtained without a reduction in the spatial resolution would result in slightly better quality images. The overall mass of the collimator is also reduced by using narrow septa uranium from approximately 10kg to less than 5 kg. From the conclusions on the two types of collimator a laminated, narrow septa uranium collimator might result in increased efficiency without significant loss of resolution. The optimum layer thickness, however, might be different from that of the laminated collimator of conventional dimensions, which would cause manufacturing problems if it were significantly narrower, due to the pyrophoric nature of uranium.

-5-

Image contrast

Chapters three and four of this thesis have investigated the imaging properties of collimators by considering the effects on the spatial resolution of septal penetration and scatter. From this, a laminated collimator structure and a narrow septa uranium collimator were selected as possible alternatives to the conventional lead collimator. However, while the spatial resolution and geometric efficiency of these collimators may be considered to be suitable, ultimately it is the quality of a medical image, and the detail visible in it, that is of importance. Radioisotope imaging is concerned with visualising varying degrees of uptake by organs of the isotope. The spatial resolution, efficiency and uniformity of an imaging system are of obvious importance. If, however, the image produced provides no information as to the differences in uptake in different regions, it is of no use. Different concentrations of activity in the patient should therefore be reflected by differences in intensity in corresponding parts of the image.

5.1 Computer model for contrast

This chapter will compare three of the collimators introduced in previous chapters in terms of image contrast. The collimators that will be investigated are the conventional lead collimator (C24), the laminated collimator (M0100), both of which have the same dimensions, and the narrow septa uranium collimator (U10). Two different phantoms will be used for the investigation, one containing 'cold' spots (i.e. areas of reduced activity) and the other 'hot' spots (i.e. areas of increased activity). Each phantom contains square objects of varying size and contrast and plans of the two phantoms are shown in figure 5.1. The phantoms are based on the cold spot phantom described by Murray *et al* 1979 and modified and used by Elliott *et al* 1986. The phantom consists of objects containing different activities to enable contrast to be determined. To produce the image, the source distribution map within the phantom is digitally convolved with the line spread functions obtained in chapter four.

5.1.1 Object distribution

Contrast in the object was simulated by creating a matrix of count density values. The pixel length in the matrix was 0.08 cm. To obtain approximately 10^6 counts in the

final image, a count density of 20 was used for the background contrast pixels, described as A in figure 5.1.

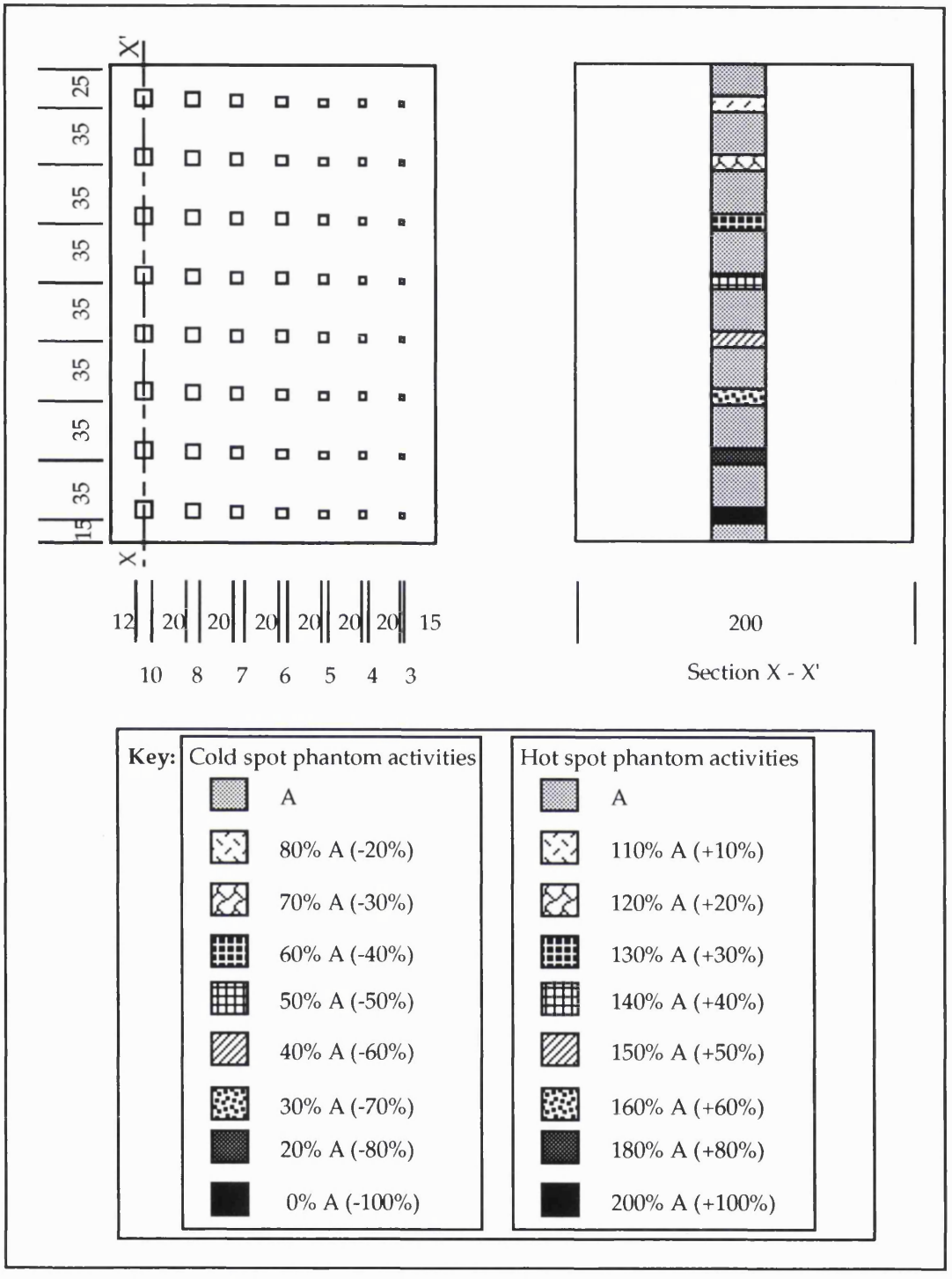

Figure 5.1 Contrast phantom. All dimensions are in mm.

5.1.2 Cold spot phantom results

The minimum object size detectable at each level of contrast for the collimators modelled using the cold spot phantom is given in table 5.1. The three collimators tested give very similar results for contrast. At 100% contrast, the smallest object detectable for

each of the collimators is used is 5 mm square, while none of the collimator can detect objects with contrast of 20% and lower. The same number of lesions are detectable when the conventional lead collimator and the narrow septa uranium collimator is used for each value of contrast. Use of the laminated collimator increases the minimum value of lesion detectable for contrast values between 40% and 80%. This is due to the increased penetration from the laminated collimator, effectively adding a background counting rate to the image around the sources.

Contrast (%)	Minimum detectable object (mm)		
	C24	M0100	U10
100	5	5	5
80	5	6	5
60	6	7	6
50	6	7	6
40	7	8	7
30	10	10	10
20	-	-	-
10	-	-	-

Table 5.1 Minimum detectable object size with contrast for cold spot phantom.

5.1.3 Hot spot phantom results

Table 5.2 lists the minimum object size detectable at each contrast level for the three collimators modelled.

Contrast (%)	Minimum detectable object (mm)		
	C24	M0100	U10
100	5	6	5
80	5	6	5
60	6	7	6
50	7	8	7
40	8	10	8
30	10	10	10
20	-	-	-
10	-	-	-

Table 5.2 Minimum detectable object size with contrast for hot spot phantom.

Once again, the narrow septa uranium collimator performs the same as the conventional lead collimator in terms of contrast detectability. The performance of the

laminated collimator is again poorer than that of the conventional lead collimator. Low contrast levels of 10% and 20% are not detectable for the object sizes modelled with any of the collimators used.

5.2 Conclusions from contrast measurements

The results obtained from the simulations of cold and hot spots of activity show that the narrow septa uranium collimator is capable of the same contrast detectability as the conventional lead collimator. The performance of the laminated collimator is worse than the others due to the higher degree of septal penetration present. Medium contrast values suffer the most when the laminated collimator is used.

In general however the three collimators behave very similarly in terms of contrast detectability and the results suggest that the narrow septa uranium collimator (U10) and the laminated collimator (M0100) would be suitable for the same types of examination as the conventional lead collimator (C24). Jarritt and Ell (1984) suggest the use of low energy general purpose collimators for a variety of SPECT studies including blood flow studies of the brain, liver studies, skeleton studies, lung perfusion studies, renal studies and cardiac studies. The narrow septa uranium and laminated collimators should therefore also be useful for such studies.

-6-

Conclusions and future work

The aim of this work was to investigate the effects that collimators have on gamma camera images. The collimator is generally considered to be the weak link of the gamma camera imaging system. This study has highlighted the following key areas in which changes could be made: improvements to the manufacturing accuracy of collimators by reducing hole misalignments, the design of laminated collimators to reduce collimator mass and to provide a more robust structure, and the use of alternative collimation materials for improved absorption, thus allowing the use of narrower septa to produce an improved efficiency while maintaining spatial resolution.

For the investigation a Monte Carlo simulation of photon transport through a multihole collimator was written which provided the average point source response function of a collimator in terms of the interactions undergone by the photons in the collimator. The code enabled collimator dimensions such as the hole size, septal thickness and length to be altered so that different collimators could be modelled. The collimator simulation also allowed collimator defects such as hole misalignment to be simulated. A minor modification to the code enabled the simulation of multi-layered collimator structures. To consider the effects of collimators on images a Monte Carlo simulation of a line source phantom was written, which modelled the transport of photons from their origin to a plane external to the phantom. Another program combined the photon distribution on this plane with the collimator response function for that particular collimator to form the image in the crystal. A digital convolution of this image with the intrinsic camera resolution produced the final system image. To quantify the various effects of collimators on images, a fitting routine was written which obtained the spatial resolutions and linearity of the images.

The collimator simulation was validated experimentally by obtaining single hole response functions for a range of source heights. Good agreement was seen for isotopes of two different energies at all source heights. The resolutions of the geometric response functions were then compared with theoretical expectations and good agreement found for a range of collimators and source heights. The effects caused by physical properties of perfect conventional lead collimators were investigated using the collimator simulation. Factors such as penetration and scatter, were considered and penetration was determined to cause a greater degradation to images than scatter. While penetrated photons caused an increase in the resolution of 1.27% photons scattered in the collimator (but not in the object) only increased the width by a further 0.25%. Although the hole diameter caused

the greatest degradation to an image because of the relatively large angular range of photons permitted, it could not be greatly reduced due to efficiency considerations.

In addition to considering perfect collimators the collimator simulation also enabled collimator defects to be modelled. The effects of hole misalignment on images were considered assuming a maximum hole angulation of 1°. This is a commonly quoted manufacturing accuracy. Collimator response functions were obtained for a range of collimators each with a given hole angulation of up to 1°. Images of the line source phantom from collimators with random angulations were then obtained by randomly selecting a given angulation for a particular location on the collimator. The angulations within each collimator were sampled from a Gaussian distribution. To simulate different degrees of collimator angulation, the width of the Gaussian distribution was changed. Only angulations up to 1° were simulated. The major effect of hole angulation seemed to be in the linearity of the images; in collimators where over 55% of the holes had angulations of less than 0.25° the degradation in linearity was noticeable. This could lead to false hot or cold regions on the image. The resolution was affected much less noticeably than the linearity, however it did worsen with increase in angulation. Although these effects would have greater significance in tomographic imaging, improvements in accuracy of manufacture would be beneficial to planar imaging.

Conventional lead collimators are heavy, due to the density of lead, and are prone to damage, because of the malleable nature of lead. In order to reduce the mass of a collimator and to provide a structure which is more robust, the Monte Carlo collimator code was modified to simulate layered collimator structures. From the response functions obtained from several different structures, a laminated collimator constructed from lead and aluminium was selected, with all layers of equal thickness. A layer thickness of 0.01 cm gave good results for the response function and was also a suitable thickness for machining. The images obtained with the laminated collimators compared very favourably with the conventional lead collimator, producing identical resolutions within statistical limits. The layer thickness selected produced a collimator with approximately 49% lead by height, resulting in a considerable reduction in mass. For a low energy general purpose collimator of the dimensions modelled throughout the thesis, this would produce a laminated collimator of approximately 6 kg compared with a lead collimator of approximately 10 kg. While this might not be significant for a low energy general purpose collimator, it would be of importance to higher energy collimators and high resolution collimators. For low energy general purpose collimators however, the main advantage would be in the strength and robustness of the laminated collimator over the conventional lead collimator.

Although lead has excellent attenuation properties making it a good material for photon collimation, other materials do exist with better attenuation properties. Other materials are also less malleable than lead which would result in collimators which would be less likely to be damaged. A disadvantage of these other materials is that they are

generally more expensive than lead. Any alternative collimator material for use in commercial collimators would need to have better attenuation properties than lead, be widely available, cheap and easily machineable. An investigation into possible materials suggested tungsten and uranium as alternatives to lead, uranium having the best attenuation properties. Depleted uranium, a form of uranium in which there is a lower concentration of the U235 isotope than in naturally occurring uranium is a by-product of the nuclear industry and has high strength. Images were produced using the Monte Carlo code for a depleted uranium collimator with the same dimensions as the conventional lead collimator. The improvement in the spatial resolution for the uranium collimator over the lead collimator was negligible when the same collimator dimensions were used. The advantage of using uranium, however, is that a narrower septa collimator could be constructed than with lead without producing an increase in the penetrated photons. The use of narrower septa, while not altering the spatial resolution, will result in an increased efficiency, which would either improve image quality, enable shorter measurement times, or possibly allow a reduction in the activity administered to the patient. When the response functions of several different septal thickness uranium collimators were obtained from the numerical model, it was found that septal thicknesses of less than half the conventional septal thickness produced similar absorption properties. When images were formed using a uranium collimator with narrow septa, the final spatial resolution values obtained were at least as good as those of the conventional lead collimator, and the efficiency was approximately 20% higher for the narrow septa uranium collimator. In addition to providing a collimator of greater strength than lead, the narrow septa uranium collimator would be lighter in weight at under 5 kg, which is less than half the mass of the conventional lead collimator.

6.1 Future work

Several extensions to the work performed for this thesis are suggested for future work. These suggestions are discussed briefly in this section.

In addition to the defect of collimator hole misalignment which has been presented in this thesis, other types of collimator defect exist. One, that of the misalignment of collimator sides, has already been incorporated into the main Monte Carlo collimator simulation and is ready for use in image production. The code enables one or more sides of the collimator hole to be rotated by a predefined amount about the centre of the side. Average response functions would be obtained for a collimator with all holes having the same side misalignments. For production of the images, the same method will be used as for the hole misalignment simulation where the location of the photon on the collimator face is calculated, the appropriate response function obtained for that location, and the final location of the photon in the crystal calculated together with

the type of interactions undergone in the collimator. In this way an image using a collimator with hole edge misalignment may be obtained.

The simulations of the laminated collimator structure and the narrow septa uranium collimator show that both are viable alternatives to the conventional lead collimator. Both require experimental confirmation. A prototype of the laminated collimator could be constructed with round holes, as this would be quicker to obtain than a hexagonal hole prototype. Before a uranium collimator is constructed it will be necessary to obtain a lump of depleted uranium of suitable dimensions to investigate the count rate obtained from the uranium on a gamma camera. If favourable results are obtained, a prototype narrow septa uranium collimator could be constructed. A laminated uranium/aluminium structure could also be investigated.

The eventual aim of the work is the improvement of gamma camera images, both by a reduction in the detection of unwanted photons, and by collimator designs which exhibit fewer manufacturing errors and are less prone to damage due to the materials from which they are constructed.

Appendices

Appendix 1 — The photomultiplier tube

The purpose of a photomultiplier (PM) tube is to convert a light pulse to an electrical signal which is sufficiently amplified to be fed into the counting electronics. A diagram of a typical PM tube is given in figure 1.1A.

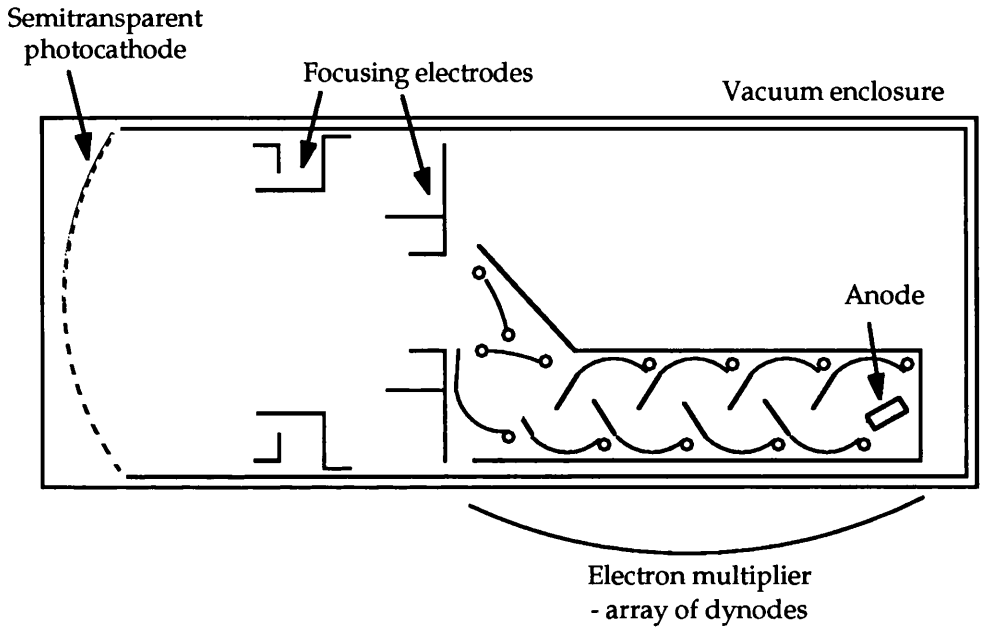

Figure 1.1A A typical photomultiplier tube.

The photocathode converts an incident light pulse into a low energy electron pulse of a similar time duration. Since the charge of the pulse is too small to measure accurately it is necessary to amplify the charge in order to achieve a convenient electrical signal. This amplification is achieved using a multiplying structure of dynodes. Electrons from the photocathode are accelerated by a voltage gradient to strike the surface of an electrode known as a dynode. The energy deposited by this electron causes the emission of more than one electron from the dynode surface. The magnitude of the potential difference between the photocathode and dynode determines the kinetic energy of the electrons incident on the dynode and hence the number of secondary electrons emitted.

The process of electron multiplication can be repeated many times by the use of further dynodes with low energy electrons from each dynode being accelerated towards the following dynode. If the multiplication factor δ for a single dynode is given by

$$\delta = \frac{\text{number of secondary electrons emitted}}{\text{number of primary photons incident}} \qquad (1.1A)$$

then if N stages are provided the overall gain Δ from the tube will be

$$\Delta = \alpha\delta^{N} \qquad (1.2A)$$

where α is the fraction of all photoelectrons collected by the multiplier structure, near unity for a well designed tube.

Appendix 2 — Linear systems theory

In an ideal imaging system the image would be a perfect representation of the object at all points. The image would be sharp with no blurring. Representing the object by the symbol f and the image by g an ideal imaging system is one in which, at all locations in the space, f = g. However, no imaging system achieves this perfect relationship.

Consider an object distribution $f(\alpha,\beta)$, entirely contained within the object plane, which gives rise to an image distribution $g(x,y)$, which is entirely contained within the image plane. In a perfect system, the information at the point (α,β) in the object plane would only contribute to the corresponding point (x,y) in the image plane. However, in practice the information from the object point (α,β) can disperse to other image locations, so for the imaging system to be useful the information at a particular point (α',β') should contribute principally to a single point (x',y'). Neighbouring points to (x',y') will contain smaller amounts of information, the contribution decreasing rapidly the further the point (x,y) is from (x',y'). This effect is seen in a gamma camera system imaging a point source of radioactivity. If the camera is fitted with a parallel hole collimator the image pixel that corresponds to the direct line of sight view will record maximum counts, adjacent pixels will record fewer counts, while pixels further away from the direct viewpoint will record still fewer counts.

This imperfect system can be described schematically by the 'black box' representation of a 'linear' imaging system (Barrett and Swindell 1981) depicted in figure 2.1. The black box receives an input signal $f(\alpha,\beta)$ producing an output response $g(x,y)$.

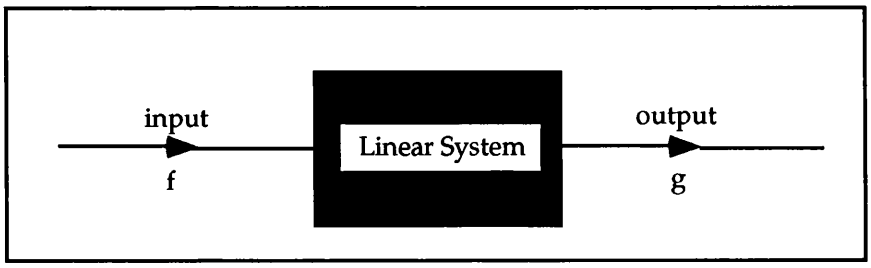

Figure 2.1A 'Black box' representation of linear system.

If two different inputs $f'(\alpha,\beta)$ and $f''(\alpha,\beta)$ produce the outputs $g'(x,y)$ and $g''(x,y)$ respectively, then the system is linear if, when the two inputs are simultaneously applied, the output is given by the sum of the two individual outputs, i.e. if

$$f(\alpha,\beta) = f'(\alpha,\beta) + f''(\alpha,\beta) \qquad (2.1A)$$

then we have a linear system if

$$g(x,y) = g'(x,y) + g''(x,y) \qquad (2.2A)$$

The function of the "black box" is the subject of linear systems theory. Suppose a function $h(x,y,\alpha',\beta')$ exists that describes the spatial dependence of the process of imaging an object plane in which the object is zero everywhere except at (α',β'), i.e. there is a point source at (α',β'). The recorded image will be described by

$$g'(x,y) = h(x,y,\alpha',\beta',f'(\alpha',\beta')) \tag{2.3A}$$

which reduces to

$$g'(x,y) = h(x,y,\alpha',\beta') \cdot f'(\alpha',\beta') \tag{2.4A}$$

if the system is linear.

If a second point source $f''(\alpha',\beta')$ is present at the same position in the object plane then from equations (2.1) and (2.4) the image will be described by

$$g'(x,y) = h(x,y,\alpha',\beta') \cdot [f'(\alpha',\beta') + f''(\alpha',\beta')] \tag{2.5A}$$

Thus for a linear imaging system, additive components in the object plane lead to additive measurements in the image plane through use of a transformation function h.

This treatment can be employed to describe a distribution of radioactivity in the object plane that is non-zero in several locations. If the system is linear, the image will be described by

$$g(x,y) = \int\int h(x,y,\alpha,\beta) \cdot f(\alpha,\beta)\, d\alpha\, d\beta \tag{2.6A}$$

The function h is the point spread function (PSF) and is a function of the spatial coordinates of both object and image plane. It is a shift-variant PSF.

If the point process is the same for all locations of the point source in the object plane, then the imaging system is said to be shift- invariant giving rise to a shift-invariant PSF. In this case the PSF is dependent only on the difference coordinates $(x-\alpha, y-\beta)$, i.e. on the relative distance between the point in the object plane and the image plane. Thus the relationship between image and object in a shift-invariant linear imaging system is

$$\begin{aligned} g(x,y) &= \int_{-\infty}^{\infty}\int_{-\infty}^{\infty} h(x-\alpha, y-\beta) \cdot f(\alpha,\beta)\, d\alpha\, d\beta \\ &= h(x,y) * f(x,y) \end{aligned} \tag{2.7A}$$

where * denotes a convolution.

If an imaging system can be considered to be both linear and shift-invariant linear systems theory may therefore be used as a means of forming the image. Consider the application of this theory to an imaging system consisting of several components. Each individual component has its own response function h. Individual components can be considered to form an image that then becomes the object for the next component, the

process being repeated until the final image is produced. This process can be described in terms of the convolution function of equation (2.7A). Suppose the imaging system consists of an object labelled 0, and three imaging components labelled 1, 2, and 3. Consider component 1 to form an image g_1 of the object f_0 then from equation (2.7A)

$$g_1 = h_1 * f_0 \qquad (2.8A)$$

This image g_1 now becomes the object for component 2, i.e.

$$f_1 = g_1 \qquad (2.9A)$$

and

$$g_2 = h_2 * f_1 \qquad (2.10A)$$

Similarly the image from component 2 becomes the object for the component 3 and

$$g_3 = h_3 * f_2 \qquad (2.11A)$$

Thus finally

$$g_{final} = g_3 \qquad (2.12A)$$

Combining equations (2.8A) to (2.12A) gives

$$g_{final} = h_3 * h_2 * h_1 * f_0 \qquad (2.13A)$$

Thus the convolution of the object, with the individual responses of the system components will produce the image.

Appendix 3 — The interaction of gamma rays with matter

3.1A Gamma ray interactions

The three interaction processes that are of importance in gamma camera imaging at low energies are photoelecric absorption, Compton scatter and coherent (or Rayleigh) scatter. These interactions are described briefly in this appendix.

3.1.1A Photoelectric Absorption

In this process an incoming photon gives up all its energy, hν, to a planetary electron. The electron is ejected from the atom with a kinetic energy equal to the energy required to remove the electron from the attraction of the nucleus. Momentum is conserved by the recoil of the residual atom. The interaction is with the atom as a whole, and not with free electrons.

For this process to occur, the photon energy must not be less than the binding energy of the electron in the atom, for example E_K for a K electron. For photon energies greater than the binding energy, the probability of interaction decreases with increasing photon energy. The interaction probability is therefore greatest when the photon energy equals the binding energy of the electron. In this energy region, the photoelectric cross-section per atom varies approximately as $(h\nu)^{-3}$. Over 80% of the primary interactions are in the K shell when the K shell can interact. When the photon energy is lower than the K shell binding energy there is a sudden drop in interaction, known as the K absorption edge, as the photon energy decreases through E_K . Similar effects occur at the three L absorption edges.

For high atomic number materials the photoelectric cross section per atom varies approximately as Z^4 and, since each atom contains Z elecrons, the photoelectric component of the mass attenuation coefficient varies as Z^3. High-Z materials are therefore very strong absorbers of photons and are widely used for beam defining and radiation purposes. Low atomic number materials have a photoelectric cross section per atom which varies approximately as $Z^{4.8}$.

When the vacancy in the electron orbit left by the ejection of the photoelectron is filled by an electron falling in from an outer orbit, the potential energy given up by this electron can appear as an x-ray photon. The photons are called characteristic radiation since their energies are characteristic of the atom from which they came. Photons resulting from electronic transitions to the K shell are called K radiation, with corresponding names for the L and other shells. The characteristic K radiation emitted from lead will have an energy of 88.004 keV.

3.1.2A Compton scattering

In this process, a photon of energy $h\nu_0$ (having wavelength λ_0, and momentum $h\nu_0/c$) collides with an electron which is regarded as free. A portion of the photon's energy is transferred to the electron, which recoils, and the remainder of the energy $h\nu$ appears as the energy of a scattered photon of longer wavelength λ_1. Applying the principles of conservation of energy and momentum to the collision shows that

$$\lambda_1 - \lambda_0 = \frac{h}{mc}(1 - \cos\theta) \qquad (3.1A)$$

where θ is the angle between the directions of the incident and scattered photons. Thus the wavelength change at a particular angle θ is independent of the initial photon wavelength.

The total Compton cross section per electron ${}_e\sigma$, which is independent of Z, is almost constant at low energies but falls off at the higher energies used in radiotherapy. The cross section per atom, ${}_{atom}\sigma$, is given by

$${}_{atom}\sigma = {}_e\sigma \cdot Z \qquad (3.2A)$$

where Z is the atomic number of the medium. Hence ${}_{atom}\sigma$ is proportional to Z. The Compton component $\frac{\sigma_c}{\rho}$ of the mass attenuation coefficient is proportional to $\frac{{}_{atom}\sigma}{M}$ and therefore to $\frac{Z}{M}$.

The angular distribution of scattered photons is predicted by the Klein-Nishina formula for the differential cross section $\frac{d\sigma}{d\Omega}$:

$$\frac{d\sigma}{d\Omega} = \left(\frac{r_0^2}{2}\right)^2 \left(\frac{\lambda_0}{\lambda_1}\right)\left(\frac{\lambda_1}{\lambda_0} + \frac{\lambda_0}{\lambda_1} - 1 + \cos^2\theta\right) \qquad (3.3A)$$

where λ_0 is the incident photon wavelength,

λ_1 is the scattered photon wavelength,

r_0 is the classical electron radius,

θ is the scattering angle with respect to the initial direction of travel, and

$d\Omega$ is the solid angle.

At very low energies the scattering is symmetrical about 90° but tends more in the forward direction with increasing photon energy.

3.1.3A Coherent scattering

In this process, the incident photon is elastically scattered by an electron which is sufficiently tightly bound in the atom for the whole atom to absorb the recoil. The energy

transfer to the atom is negligible causing the photon to be scattered without loss of energy.

Coherent scatter is more prevalent at low photon energies since the incident photon wavelength must be greater than the electron spacing for elastic scattering to occur. The increase in electric charge with atomic number Z causes the electrons to appear more bound resulting in an increase in the probability of coherent scatter. The bound electron is excited by the incident photon energy emitting a photon of the same wavelength which returns the electron to its original state. Since the excitation of the electron must be sufficiently small to prohibit atomic excitation or ionisation the scattering angles obtained are small.

The coherent scatter differential cross section may be written as

$$\frac{d\sigma_{coh}}{d\Omega}(\theta,\alpha,Z)=\frac{d\sigma_t(\theta)}{d\Omega}\cdot F^2(x,Z) \qquad (3.4A)$$

where $\frac{d\sigma_t}{d\Omega}=r_e{}^2\cdot\left(\frac{1+\cos^2\theta}{2}\right)$ is the differential Thomson cross section per electron for elastic scattering from an unpolarised beam,

r_e is the classical electron radius,

θ is the photon scattering angle and

F(x,Z) is the atomic form factor (Hubbel *et al* 1975) used to correct $\frac{d\sigma_t(\theta)}{d\Omega}$ for electron binding effects.

The factor F(x,Z) is the atomic form factor (Hubbel *et al,* 1979) used to correct the Thomson distribution for electron binding effects. The square of this quantity is the probability that the Z electrons of the atom take up the recoil momentum without absorbing any photon energy. $F^2(x,Z)$ has values near Z^2 for small scattering angles and falls by several orders of magnitude for large angles resulting in a highly anisotropic distribution.

The coherent scattering cross section per atom varies approximately as

$$_{atom}\sigma_{coh}\propto(h\upsilon)^{-2}Z^{2.5} \qquad (3.5A)$$

Appendix 4 — Monte Carlo Techniques

4.1A Principles of Monte Carlo

Many physical processes are random in nature giving rise to probability distributions of their occurrence. Such processes may be simulated by the generation of random numbers from these known probability distributions. These techniques are known as Monte Carlo methods. Monte Carlo methods are commonly used for studying photon or electron histories and have many applications in medical physics, for example absorbed dose calculations, determination of the efficiencies of gamma-ray detectors, etc. (Andreo 1991). A Monte Carlo simulation of photon transport is a sequence of random choices: distance to next collision, type of collision process and trajectory and photon energy leaving collision. the two most frequently used methods being the direct (or inversion) method and the rejection method. It is important that the random number generator used in Monte Carlo methods gives rise to an unpredictable sequence for the duration of the calculation and mathematical algorithms are used most frequently to generate such a sequence. Although mathematical algorithms produce what has been referred to as only 'pseudo random' numbers, such methods have passed randomness tests equally as well as random numbers obtained by physical processes.

4.1.1A Sampling methods

Direct Sampling: The basic idea of direct sampling requires the inversion of the cumulative probability distribution obtained from the random process under study (Raeside 1976). If f(x) is the probability density function for the variable x, then the cumulative probability that x is less than X is

$$F(x) = \int_0^X f(x)dx \qquad (4.1A)$$

The requirement that $0 \leq F(x) \leq 1$ leads to a normalisation condition:

$$\int_0^{X_m} f(x)dx = 1 \qquad (4.2A)$$

where x_m is the maximum value of x.

If a random number r* is generated where $0 \leq r^* \leq 1$ then a random sample x* may be produced from the distribution F(x) by inverting

$$r^* = F(x) \qquad (4.3A)$$

to find X.

Rejection sampling: As its name suggests, rejection sampling rejects certain of the random numbers generated. The basis of the criterion for rejection is described below.

Random samples drawn from a probability distribution of density f(x) are denoted by $x_1, x_2, \ldots$ where

(i) $f(x) = 0$ for $x < a, x > b$ and

(ii) $f(x) < m$ for $a < x < b$.

Consider random samples $u_1, u_2, \ldots$ and $v_1, v_2, \ldots$ drawn from two uniform density distributions $p(u) = \frac{1}{(b-a)}$ and $p(v) = \frac{1}{(m-0)}$, respectively. The points $(a + u_1, v_1)$, $(a - u_2, v_2)$, ... are obtained from this sampling, the points being bounded by the lines $x = a$, $x = b$, $f(x) = 0$, and $f(x) = m$. Rejection sampling rejects all points lying above the curve f(x) and retains all those points lying on or below the curve. It can be shown that the rejection method of sampling is equivalent to the direct method of sampling from the density f(x) (Raeside 1976).

4.2A Applications of Monte Carlo Techniques

In photon transport studies Monte Carlo techniques can be applied to simulate scatter. In gamma camera studies the scattering processes involved are Compton and Rayleigh scatter (Appendix 3).

4.2.1A Monte Carlo Sampling of Compton Scattered Photons

Both the direct and rejection methods may be used to sample incoherently scattered photons, however, Pickard (1982) demonstrated that, although more complicated, rejection sampling was superior to direct sampling.

The rejection technique used is based on that devised by Khan (1956) and involves transforming the Klein-Nishina formula (equation 3.3A) into a form yielding the probability of the scattered photon having a wavelength in the range λ_1 and $\lambda_1 + d\lambda_1$. This form is obtained by evaluating

$$\frac{d\sigma}{d\lambda_1} = \left(\frac{d\sigma}{d\Omega}\right) \cdot \left(\frac{d\Omega}{d\lambda_1}\right) \qquad (4.4A)$$

The shift in the photon wavelength is given by the Compton shift formula (equation 3.1A). The scattering angle can be evaluated and using the Klein-Nishina formula may be rewritten as

$$d\sigma = \pi r_0 \left(\frac{m_0 c}{h}\right)\left(\frac{\lambda_0}{\lambda_1}\right)^2 \left[\frac{\lambda_1}{\lambda_0} + \frac{\lambda_0}{\lambda_1} - 1 + \left(1 - \frac{m_0 c}{h}\lambda_1 + \frac{m_0 c}{h}\lambda_0\right)^2\right] d\lambda_1 \quad (4.5A)$$

A commonly used scaling convention sets Planck's constant, h, the electron rest mass, m_0, and the speed of light, c, to be unity. Adopting this convention enables us to express equation 21 for a given λ as the probability density p:

$$p(r|\lambda_0) \propto \frac{1}{r^2}\left[\frac{1}{r} + r - 1 + (1 - \lambda_0 r + \lambda_0)^2\right] \qquad (4.6A)$$

where $r \equiv \frac{\lambda_1}{\lambda_0}$.

It can be shown that

$$p(r|\lambda_0) \propto \left(\frac{\lambda_0 + 2}{9\lambda_0 + 2}\right) g_1(r) h_1(r) + \left(\frac{8\lambda_0}{9\lambda_0 + 2}\right) g_2(r) h_2(r) \qquad (4.7A)$$

where $g_1 \equiv \frac{\lambda_0}{2}$, $h_1 \equiv 4\left(\frac{1}{r} - \frac{1}{r^2}\right)$

and $g_2 \equiv \frac{\lambda_0 + 2}{2r^2}$, $h_2 \equiv \frac{(1 - \lambda_0 r + \lambda_0)^2 + \frac{1}{r}}{2}$.

The variables g_1 and g_2 are both probability densities such that

$$\int_1^{1+2/\lambda_0} g_1(r)dr = \int_1^{1+2/\lambda_0} g_2(r)dr = 1 \qquad (4.8A)$$

The limits of integration are obtained by reducing the Compton shift formula in scaled units to

$$\lambda_1 - \lambda_0 = 1 - \cos\theta \qquad (4.9A)$$

allowing λ_1 to range from λ_0 to $\lambda_0 + 2$. Thus r may have values from 1 to $(1 + 2 / \lambda_0)$.

The two parts of equation 4.8A are referred to as track 1 (the g_1h_1 - track) and track 2 (the g_2h_2 - track), respectively. Khan's application of the rejection sampling method (Khan 1956) selects either track 1 or track 2 by the generation of a random number r_1

If $0 \le r_1 \le \left(\frac{\lambda_0 + 2}{9\lambda_0 + 2}\right)$ then track 1 is selected

if $\frac{8\lambda_0}{9\lambda_0 + 2} \le r_1 \le 1$ track 2 is selected.

Having selected which track is entered, a second random number r_2 is generated and the cumulative probability G_1 (for track 1) or G_2 (for track 2) is sampled by inversion, where

$$G_1 \equiv \int_1^{\rho} g_1(r)dr = \left(\frac{\lambda_0}{2}\right)(\rho - 1) \qquad (4.10A)$$

$$G_2 \equiv \int_1^{\rho} g_2(r)dr = \left(\frac{(\lambda_0 + 2)}{2}\right)\left(1 - \frac{1}{\rho}\right) \qquad (4.11A)$$

giving $\rho = 1 + \left(\frac{2}{\lambda_0}\right) r_2$ for track 1

and $\rho = \frac{\lambda_0 + 2}{[\lambda_0 + 2(1 - r_2)]}$ for track 2.

A third random number r_3 is generated in order to apply the rejection procedure, and the following tests are applied:

If $r_3 \leq 4\left(\frac{1}{\rho} - \frac{1}{\rho^2}\right)$ then ρ for track 1 is accepted

if $r_3 \leq \frac{1}{2}\left[(\lambda_0 - \rho\lambda_0 + 1)^2 + \frac{1}{\rho}\right]$ then ρ for track 2 is accepted.

If a sample of ρ is accepted then the scattered wavelength λ_1 is obtained using $\lambda_1 = \rho\lambda_0$
Using this value of λ_1, the polar scattering angle θ is determined using Compton's shift formula (in scaled units)

$$\theta = \cos^{-1}(1 + \lambda_0 - \lambda_1) \qquad (4.12A)$$

The azimuthal scattering angle τ is determined by sampling an isotropic azimuthal distribution ($-\pi \leq \tau \leq \pi$).
Finally, the scattered photon energy is determined using

$$E_1 = \frac{5111.006}{\lambda_1} \qquad (4.13A)$$

4.2.2A Monte Carlo Sampling of Coherent Scattered Photons

Since coherent scatter is an elastic process, the only parameter that needs to be sampled in Monte Carlo sampling of coherent photons is the scattering angle. The differential cross section for coherent scatter was given in equation 3.4A.

Hubbel *et al* (1975) have tabulated atomic form factors as a function of the photon momentum transfer for all elements Z = 1 to 100. If the incident photon is considered to have momentum $h\underline{k}_i$ and the scattered photon momentum is $h\underline{k}_s$ then the momentum transfer is $\underline{q} = \underline{k}_i - \underline{k}_s$ in units of inverse length (Jackson and Hawkes 1981). In coherent scatter, the photon energy is constant so $|k_i| = |k_s| = \frac{1}{\lambda}$ thus

$$h \cdot q = \frac{2}{\lambda} h\left(\sin\frac{\theta}{2}\right) = h \cdot x \qquad (4.14A)$$

where $x = \frac{2}{\lambda}\left(\sin\frac{\theta}{2}\right)$ is the momentum transfer of the photon.

The atomic form factor squared has a maximum value of Z^2 for zero momentum transfer, rapidly decreasing to zero as the momentum transfer increases to infinity, resulting in a forward peak at $\theta = 0°$.

Zerby (1963) describes a Monte Carlo sampling technique that combines inversion and rejection sampling. The method was applied by Williamson and Morin (1983) to the problem of coherent scatter since conventional rejection sampling was found to be very inefficient.

In this method the coherent scatter differential cross section $\frac{d\sigma_{coh}}{d\Omega}$ is considered to be the product of two probability density functions g and h respectively:

$$\frac{d\sigma_{coh}}{d\Omega} = g \cdot h \qquad (4.15A)$$

where $g = F^2(x, Z)$

and $h = \left(\frac{1+\cos^2\theta}{2}\right)$ and is normalised to have a maximum value of unity.

Given an random number r* ($0 \leq r^* \leq 1$) a random variate X* can be generated distributed according to $\frac{d\sigma_{coh}}{d\Omega}$ in the following way:

(i) X* is defined such that:

$$r^* = \frac{\int_0^{X^*} F^2 dx}{\int_0^{x_{max}} F^2 dx} \qquad (4.16A)$$

where $x_{max} = \frac{1}{\lambda} = 0.0801 \cdot E$ with E in units of KeV and x in units of Å $^{-1}$

To overcome the energy dependence equation (4.16A) is rewritten:

$$r^* \left(\frac{\int_0^{x_{max}} F^2 dx}{\int_0^{\infty} F^2 dx} \right) = \left(\frac{\int_0^{x^*} F^2 dx}{\int_0^{\infty} F^2 dx} \right) \qquad (4.17A)$$

The integral F^2 is zero for $x^* = 0$, converges as x* approaches infinity and monotonically approaches unity as $x^* \longrightarrow x_{max}$. Thus if $x^* \leq x_{max}$ the evaluation of the integral can be omitted. The equation may be solved numerically by integrating F^2 using the trapezoidal rule over the momentum transfer increments of the form factor tabulation (Hubbel 1979).

(ii) Having evaluated x*, the scattering angle θ is calculated using

$$\cos\theta = 1 - \left(\frac{X^*}{\alpha k}\right)^2 \qquad (4.18A)$$

where $\alpha = h\upsilon_0 / mc^2$ and k = 29.1445.

θ is accepted if $r^{**} \leq \frac{1+\cos^2\theta}{2}$, where r** is a separately generated random number, otherwise a new random number is generated and the process repeated.

As in Compton scatter the azimuthal angle τ is determined randomly between $-\pi \leq \tau \leq +\pi$.

References

Andreo P. (1991). Monte Carlo techniques in medical radiation physics. *Phys. Med. Biol.* **36,** 891-920.

Anger H.O. (1952). Use of a gamma-ray pinhole camera for *in vivo* studies. *Nature.* **170,** 200-201.

Anger H.O. (1958). Scintillation camera. *Rev. Sci. Instrum.* **29,** 27-33.

Anger H.O. (1964). Scintillation camera with multichannel collimators. *J. Nucl. Med.* **5,** 515-531.

Anger H.O. and Davis D.H. (1964). Gamma-ray detection efficiency and image resolution in sodium iodide. Rev. *Sci. Instrum.* **35,** 693-697.

Barrett H.H. and Swindell W. (1981). The theory of image formation, detection and processing. *Academic Press, London.*

Beck J.W., Jaszczack R.J., Coleman R.E., Starmer C.F. and Nolte L.W. (1982). Analysis of SPECT including scatter and attenuation using sophisticated Monte Carlo modelling methods. *IEEE Trans. Nucl. Sci.* **NS-29,** 506-511.

Beck R.N. and Redtung L.D. (1985a). Hole pattern analysis in collimator design. *J. Nucl. Med.* **26,** P44.

Beck R.N. and Redtung L.D. (1985b). Collimator design using ray-tracing techniques. *IEEE Trans. Nucl. Sci.* **32,** 865-869.

Bell T.K., Spiers E.W. and Johnston A.R. (1970). Calculation of penetration factors for point gamma ray sources off the axis of cylindrical hole collimators. *Phys. Med. Biol.* **15,** 47-56.

Bonte F.J., Graham K.D. and Dowdey J.E. (1971). Image aberrations produced by multichannel collimators for a scintillation camera. *Radiology.* **98,** 329-334.

Bradshaw J., Burnham C., Correia J., Rogers W.L. and Clinthorne N.H. (1985). Application of Monte Carlo methods to the design of SPECT detector systems. *IEEE Trans. Nucl. Sci.* **32,** 753-757.

Bramlet R.C. (1970). Elimination of collimator artifacts in scintillation camera images. *Radiology* .**94,** 417-419.

Budinger T.F. (1980). Physical attributes of single photon tomography. *J. Nucl. Med.* **21,** 579-592.

Budinger T.F. and Gullberg G.T. (1977). Transverse reconstruction of gamma reay emitting radionuclides in patients. In Reconstruction tomography in diagnostic radiology and nuclear medicine, *University Park Press, Baltimore, MD,* 315-342.

Busemann-Sokole E. (1987). Measurement of collimator hole angulation and camera head tilt for slant and parallel hole collimators used in SPECT. *J. Nucl. Med.* **28,** 1592-1598.

Cassen B., Curtis L., Reed C. and Libby R. (1951). Instrumentation for I^{131} use in medical studies. *Nucleonics.* **9,** 46-50.

Chang W., Lin S.L., Henkin R.E.., and Salo B.C. (1980). A multisegmental slant hole tomographic collimator (MUST): a new tomographic gamma camera system. *J. Nucl. Med.* **21,** P28.

Chang W., Bruch P.M., Wesolowski C., Kirchner P.T. and Ehrhardt J.C. (1985). Performance of cast collimator for SPECT imaging. *J. Nucl. Med.* **26,** P44.

Chang W., Li S., Williams J.J., Bruch P.M., Wesolowski C.A., Ehrhardt J.C. and Kirchner P.T. (1988). New methods of examining gamma camera collimators. *J. Nucl. Med.* **29,** 676-683.

De Vries D.J., Moore S.C., Zimmerman R.E., Mueller S.P. Friedland B. and Lanza R.C. (1990). Development and validation of a Monte Carlo simulation of photon transport in an Anger camera. *IEEE Trans. Med. Imaging.* **9,** 430-438.

Dresser M.M and Knoll G.F. (1973). Results of scattering in radioisotope imaging. *IEEE Trans. Nucl. Scl.* **NS-20,** 266-272.

Elliott A.T., Short M.D. and Barnes K.J. (1986). Performance of gamma cameras—Part IV Report STB/86/9, DHSS, London.

Farrell T.J.., Cradduck T.D. and Chamberlain R.A. (1984). The effect of collimators on the center of rotation in SPECT. *J. Nucl. Med.* **25**, 632-633.

Floyd C.E., Jaszczak R.J. and Coleman R.E. (1985a). *IEEE Trans. Nucl. Sci.* **NS-32**, 779.

Floyd C.E., Jaszczak R.J. Greer K.L. and Coleman R.E. (1985b). Deconvolution of Compton scatter in SPECT. *J. Nucl. Med.* **26**, 403-408.

Freedman G.S. (1970). Tomography with a gamma camera — theory. *J. Nucl. Med.* **11**, 602-604.

Gerber M.S. and Miller D.W. (1974). Parallel-hole collimator design. *J. Nucl. Med.* **15**, 724-725.

Gillen G.J., Hilditch T.E. and Elliott A.T. (1988). Nonisotropic point spread function as a result of collimator design and manufacturing defects. *J. Nucl. Med.* **29**, 1096-1100.

Heller S.L. and Goodwin P.N. (1987). SPECT instrumentation — performance, lesion detection, and recent innovations. *Seminars in Nuclear Medicine.* **17**, 184-199.

Hubbel J.H., Veigele W.J., Briggs E.A., Brown R.T., Cromer D.T. and Howerton R.J. (1977). Atomic form factors, incoherent scattering functions and photon scattering cross sections. *J. Phys. Chem. Ref. Data* . **6**, 615.

International Electrotechnical Commission (1984). Characteristics and test conditions of radionuclide image devices. IEC 789. (BSI 6609, 1985).

Jackson D.F. and Hawkes D.J. (1981). X-ray attenuation coefficients of elements and mixtures. *Physics Reports (Physics Letters C).* **70**, 169.

Jahns M.F. (1981). The influence of penetrating radiation on collimator performance. *Phys. Med. Biol.*,**26,** 113-124.

Jarritt P.H. and Ell P.J. (1984). Gamma Camera Emission Tomography: Quality Control and Clinical Applications. *Alden, Oxford.*

Jenkins T.M., Nelson W.R. and Rindi A. (1988). In: Monte Carlo Transport of Electrons and Photons. *Plenum, New York.*

Keller E.L. (1968). Optimum dimensions of parallel-hole, multi-aperture collimators for gamma-ray cameras. *J. Nucl. Med.* **9,** 233-235.

Khan H., (1956). Applications of Monte Carlo. *RAND, Santa Monica, Ca.*

Kibby P.M., (1969). The design of multichannel collimators for radio-isotope cameras. *Br. J. Radiol.* **42,** 91-101.

King S.E., Jih F., Lim C.B., Chaney R. and Gray E. (1985). Spectral-spatial-sensitivity distortion trends and an accurate correction method in scintillation gamma cameras. *IEEE Trans. Nucl. Sci.* **32,** 870-874.

Knoll G.F. (1989). in: Radiation detection and measurement. *Wiley: New York.*

Mallard J.R. and Myers M.J. (1963a). The performance of a gamma camera for the visualisation of radioactive isotopes *in vivo*. *Phys. Med. Biol.* **8,** 168-182.

Mallard J.R. and Myers M.J. (1963b). Clinical applications of a gamma camera. *Phys. Med. Biol.* **8,** 183-192.

Malmin R.E., Stanley P.C. and Guth W.R. (1990). Collimator angulation error and its effect on SPECT. *J. Nucl. Med.* **31,** 655-659.

Mather R.L. (1957). Gamma-ray collimator penetration and scattering effects. *J. Appl. Phys.* **28,** 1200-1207.

Metz C.E., Atkins F.B. and Beck R.N. (1980). The geometric transfer function component for scintillation camera collimators with straight parallel holes. *Phys. Med. Biol.* **25,** 1059-1070.

Moore S.C., Kouris K. and Cullum I. (1992). Collimator design for single photon emission tomography. *Eur. J. Nucl. Med.* **19**, 138-150.

Moores G.E. (1948). Use of radioactive diiodofluorescein in the diagnosis and localization of brain tumors. *Science.* **107**, 569-571.

Muehllehner G. (1969). A diverging collimator for gamma ray imaging cameras. *J. Nucl. Med.* **10**, 197-201.

Muehllehner G. (1971). A tomographic scintillation camera. *Phys. Med. Biol.* **16**, 87-95.

Muehllehner G. and Luig H. (1973). Septal penetration in scintillation camera collimators. *Phys. Med. Biol.* **18**, 855-862.

Muehllehner G., Colsher J.G. and Stoub E.W. (1980). Correction for field nonuniformity in scintillation cameras through removal of spatial distortion. *J. Nucl. Med.* **21**, 771-776.

Murray K.J., Elliott A.T. and Wadsworth J. (1979). A new phantom for the assessment of nuclear medicine imaging equipment. *Phys. Med. Biol.* **24**, 188-192.

Nelson W.R., Hirayama H. and Rogers D.W.O. (1985). The EGS4 code system. *SLAC-265.*

Newiger H. and Jordan K. (1985). Optimisation of collimators for imaging positron emitters by a gamma camera. *Eur. J. Nucl. Med.* **11**, 230-234.

Pickard M. (1982). An investigation into the information content of the scattered radiological beam. *M.Sc. Dissertation.* University of London, London UK.

Raeside D.E. (1976). Monte Carlo principles and applications. *Phys. Med. Biol.* **21**, 181-197.

Rogers W.L., Clinthorne B.A., Koral K.F. and Keyes J.W. (1982). Field-flood requirements for emission computed tomography with an Anger camera. *J. Nucl. Med.* **23**, 162-168.

Rosenthal M.S. and Henry L.J. (1990). Scattering in uniform media. *Phys. Med. Biol.* **35**, 265-274.

Rottenberg A.D., and Johns H.E. (1965). Collimator efficiency and design I. Collimator efficiency. *Phys. Med. Biol.* **10**, 51-65.

Royal H.D., Brown P.H. and Claunch B.C. (1979). Effects of a reduction in crystal thickness on Anger camera performance. *J. Nucl. Med.* **20**, 977-980.

Sharpe J. and Taylor D. (1951). Nuclear Particle and Radiation Detectors. Part 2. Counters and Counting Systems. *Proc. Instr. Electr. Eng.* **98**, 209-230.

Short M.D. (1984). Gamma camera systems. *Nucl. Instr. and Meth.* **221**, 142-149.

Shosa D.W. O'Connell J.W. and Hattner R.S. (1980). Motivation for the rotating slant hole approach to scintillation camera tomography. *J. Nucl. Med.* **21**, (2), 27.

Simon R.W. and Williams B.F. (1968). *IEEE Trans. Nucl. Sci.* **NS-15**, 167-176.

Simons H.A.B. (1962). The calculation of gamma ray penetration of the walls of cylindrical and conical collimating holes. *Phys. Med. Biol.* **7**, 561-576.

Simons H.A.B. (1970). A computer method for calculation of the point source response of a focussing collimator. *Phys. Med. Biol.* **15**, 57-70.

Storm E. and Israel H.I. (1970). Photon cross sections from 1keV to 100MeV for elements Z=1 to 100. *Nuclear data tables.* **A7**, 565.

Svedberg J.D. (1972). On the intrinsic resolution of a gamma camera system. *Phys. Med. Biol.* **17**, 514-524.

Todd-Pokropek A. (1980). Image processing in nuclear medicine. *IEEE Trans. Nucl. Sci.* **NS-27**, 1080-1094.

Walker W.G., (1969). Design and analysis of scintillation camera lead collimators using a digital computer. In Medical Radioisotope Scintigraphy, **1**, *Vienna, IAEA*, 545-560.

Wilks R.J., Mallard J.R. and Taylor C.G. (1969). The collywobbler — a moving collimator image processing device for stationary detectors in radioisotope scanning. *Br. J. Radiol.* **42,** 705-709.

Williamson J. F. and Morin R. L. (1983). An efficient method of randomly sampling the coherent angular scatter distribution. *Phys. Med. Biol.* **28,** 57.

Yanch J.C., Dobrzeniecki A.B., Ramanathan C. and Behrman R. (1992). Physically realistic Monte Carlo simulation of source, collimator and tomographic data acquisition for emission computed tomography. *Phys. Med. Biol.* **37,** 853-870.

Yeh E.-Y. (1979). Distortion of bar-phantom image by collimator. *J. Nucl. Med.* **20,** 260-261.

Yeh E.-Y. (1983). Polarity in a hexagonal collimator. *J. Nucl. Med.* **24,** 1203-1204.

Zerby C.D. (1963). In: Methods of Computational Physics **Vol. 1**. ed. Alder B., Fernbach S. and Rotenburg M., *New York.*

Zimmerman R.E. (1977). Advances in nuclear medicine imaging instrumentation. In Medical Radionuclide Imaging. **Vol. 1,** *Vienna, IAEA,* 121-139.

Horrocks J.A. (1988). The application of dual energy techniques to digital ionography. Ph.D Thesis, University of London.

Press W.H. Flannery B.P. Teukolsky S.A. and Vetterling W.T. (1988). In: Numerical recipes: the art of scientific computing. *Cambridge.*

Rodriguez-Villafuerte M. (1991). Private communication.